Numerical Assessment of Galloping for VTS Cross-Sections

Master Thesis Offshore & Dredging Engineering

by

Tom Toutenburg

Supervisor TU Delft:	Prof. Dr. A.V. Metrikine
Supervisor Allseas:	Dr. Ir. N.J. Mallon
Second corrector:	Dr. Ir. H. Hendrikse
Graduation date:	19 March 2026
Faculty:	Mechanical Engineering, Delft

TU Delft

Allseas

Preface

This thesis marks the completion of my Master of Science in Offshore & Dredging Engineering at Delft University of Technology. It explores the galloping behaviour of vertical transport systems for deep-sea mining and was carried out in collaboration with Allseas.

I would like to sincerely thank Niels Mallon, my company supervisor at Allseas, for his steady guidance, technical insight, and encouragement throughout this project. His expertise was very helpfull in shaping the direction and depth of the work. I also appreciate the many helpful conversations with the colleagues at Allseas, whose practical perspectives greatly enriched my understanding of several offshore systems.

I am also grateful to Andrei Metrikine, my academic supervisor at Delft University of Technology. His sharp analytical feedback and ability to challenge my assumptions helped elevate the technical quality of the thesis and encouraged a deeper engagement with the underlying mechanics.

Support from outside the academic and professional domain was just as important. I am grateful to my friends and family, whose encouragement, patience, and perspective were invaluable during the more intense stages of the process.

Lastly, I acknowledge the use of AI-assisted tools during the development of this thesis. These tools contributed to programming, structuring technical sections, improving clarity of expression, and spelling control. All output was critically reviewed to ensure the quality and integrity of the final work.

Abstract

Deep-sea mining is being developed as an alternative source of critical metals, using a subsea collector connected to a surface vessel by a multi-kilometre vertical transport system (VTS). During pilot testing, the upper section of the VTS was observed to adopt significant inclination, raising concerns that flow-induced vibrations (FIV), particularly galloping-type instabilities, could contribute to sustained dynamic loading and accelerated fatigue damage.

The objective of this thesis is to develop and apply a cross-sectional, quasi-steady time-domain model that can screen two representative in-line, three-cylinder VTS bundle cross-sections for galloping susceptibility over the full range of inflow orientations, and to assess how sensitive the predicted stability behaviour is to key modelling choices, especially hydrodynamic inertia represented through added mass.

The approach follows a stepwise workflow. First, a published 3DOF galloping paper is reproduced to verify the numerical implementation and confirm that the solver captures the essential coupled translation–rotation response, including the transition from decay to bounded limit-cycle oscillations. The verified framework is then transferred to two representative in-line, three-cylinder VTS cross-sections: Model 18A and Model 32A. For these cases, quasi-steady force and moment coefficients obtained from MARIN are represented by smooth fitted functions and combined with Den Hartog screening to identify orientations that are potentially prone to negative hydrodynamic damping.

For Model 18A, the simulations show a clear and repeatable response pattern. The response-active inflow-direction intervals from the coupled 3DOF simulations align closely with the Den Hartog screening zones, indicating that the quasi-steady onset indicator provides a reliable first-order localisation tool for this cross-section. Differences between added-mass assumptions are mainly expressed in the post-onset amplitude level: constant added mass yields the largest limit-cycle amplitudes, the frequency-dependent formulation gives intermediate amplitudes, and neglecting added mass gives the smallest response. Sensitivity studies further show that unstable orientation windows remain largely unchanged under variations in stiffness, torsional compliance, and inflow speed, while the achieved response levels depend strongly on these parameters.

For Model 32A, the results are less consistent. The simulated response windows show noticeable offsets relative to the Den Hartog boundaries, and the predicted response is more sensitive to the higher-order coefficient fit required to represent the available data. This indicates that the 32A predictions should be interpreted with additional caution and highlights the need for improved coefficient processing and validation, for example, through refined CFD or experimental datasets and expanded model checks.

Overall, the developed framework provides an effective screening tool to identify VTS cross-section orientations that are susceptible to galloping-type instabilities and to quantify the influence of added-mass modelling on predicted response levels. The results highlight that reliable coefficient data and careful coefficient representation are essential to obtain robust stability predictions for complex, non-circular VTS geometries.

List of Figures

List of Tables

Contents

Nomenclature

Abbreviations

Abbreviation	Definition
2D/3D	Two/three-dimensional
DOF	Degree(s) of freedom
AOA	Angle of attack
CFD	Computational Fluid Dynamics
EOM	Equation(s) of motion
FBD	Free-body diagram
FIV	Flow-induced vibrations
MARIN	Maritime Research Institute Netherlands
PTL	Power transmission line
REE	Rare earth elements
REO	Rare earth oxides
VIV	Vortex-induced vibrations
VTS	Vertical transport system
WIV	Wake-induced vibrations

Symbols

Symbol	Definition	Unit
A_{end}	End-window resultant response amplitude	[m]
A_{ref}	Reference area	[m^2]
C_A	Added-mass coefficient	[-]
$C_D(\alpha)$	Drag coefficient	[-]
$C_L(\alpha)$	Lift coefficient	[-]
$C_M(\alpha)$	Moment coefficient	[-]
c_x, c_y	Translational viscous damping coefficients	[N s/m]
c_θ	Rotational viscous damping coefficient	[N m s/rad]
D	Characteristic cross-section width / diameter	[m]
f	Oscillation frequency	[Hz]
f_0	natural frequency	[Hz]
f^*	Reduced frequency	[-]
F_D	Drag force component	[N]
F_L	Lift force component	[N]
F_x	Force component x-direction	[N]
F_y	Force component y-direction	[N]
$H(\alpha) = \dfrac{dC_L}{d\alpha} + C_D$	Den Hartog galloping indicator	[-]
$I_{a,\theta}$	Added polar inertia	[kg m^2]
I_θ	Polar mass moment of inertia	[kg m^2]
k_x, k_y	Translational stiffness	[N/m]
k_θ	Rotational stiffness	[N m/rad]
L	Spanwise length	[m]
m	Structural mass	[kg]
m_a	Added mass	[kg]
$m_{a,x}$, $m_{a,y}$	Added mass terms in x and y	[kg]
M	Aerodynamic/hydrodynamic pitching moment	[N m]
T	Hydrodynamic moment / torque about z-axis	[N m]
t	Time	[s]
$u = \lVert \mathbf{U}_{\mathrm{rel}} \rVert$	Relative flow speed magnitude	[m/s]
U_∞	Free-stream velocity magnitude	[m/s]
U_{rel}	Relative flow velocity	[m/s]
U_r	Reduced velocity $U_\infty/(f\,D_{\mathrm{ref}})$	[-]
V_x, V_y	Relative flow components	[m/s]
$x(t)$, $y(t)$	In-line and cross-flow displacement	[m]
α	Effective angle of attack	[rad]
α_0	Constant offset angle	[rad]
β	Inflow angle of $\mathbf{U}_{\mathrm{rel}}$	[rad]
ω	Natural frequency	[rad/s]
ψ	Inflow direction in global frame	[rad]
ρ	Fluid density	[kg/m^3]
$\theta(t)$	Cross-section rotation	[rad]
ζ	Damping ratio	[-]

1

Introduction

The global transition to low-carbon energy systems is quickly increasing the demand for critical minerals, including rare earth elements (REE) and other metals. These materials are used in batteries and a wide range of renewable-energy technologies [1, 2]. Currently, a large share of REE supply and refining capacity, of rare earth oxides (REO), is concentrated in a few countries, especially China (Figure 1.1). This concentration raises concerns about supply-chain vulnerability, geopolitical exposure, and the environmental and social footprint of terrestrial mining and refining activities [3–5]. Beyond the extraction, the following stages can be equally critical bottlenecks. These stages are chemical separation, oxide refining, and metal and alloy production. As a result, governments and industry are increasingly considering different technologies, including new mining and processing projects, recycling and circular-economy pathways, substitution, and alternative primary sources of supply [2].

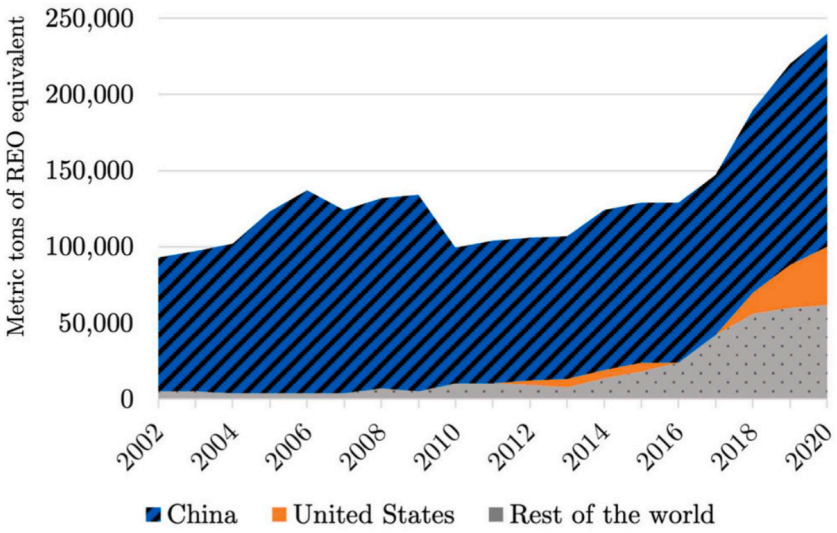

Figure 1.1: World production of rare earth oxides equivalent for China, US, and the rest of the world, 2002–2020 [4]

Deep-sea mining is being identified as a potential alternative to mine critical mineral resources. Polymetallic nodules lie on the sea bed. These nodules contain significant concentrations of metals such as nickel, cobalt, copper, and manganese, and are therefore discussed as a possible complement to land-based mining. However, deep-sea mining is relatively new and therefore introduces significant uncertainties and debate on ecological impacts, environmental baselines, and governance frameworks, which remain active topics of research and policy

development [6]. In contrast to land-based mining within national borders, many potential nodule fields are located in areas beyond national jurisdiction, meaning that permitting, regulation, monitoring, and liability are governed through international frameworks rather than a single state. From an engineering perspective, deep-sea mining pushes the limits of offshore system design due to large water depths, long and slender suspended structures, and complex coupled hydrodynamic and structural behaviour.

Allseas is an offshore contractor and marine engineering company based in the Netherlands. Allseas has been working on technologies related to a solution for polymetallic nodule harvesting and vertical transport of the harvested nodules to the surface. The system consists of a subsea collector that operates on the seabed and is connected to a surface vessel through a vertical transport system (VTS). This arrangement is illustrated in Figure 1.2. The VTS consists of multiple long and slender pipes extending over several kilometers. During operation, the VTS is exposed to ocean currents and operational loads driven by the motion of the vessel. Ensuring safe and reliable operation requires understanding both the mean configuration of the system and the dynamic response.

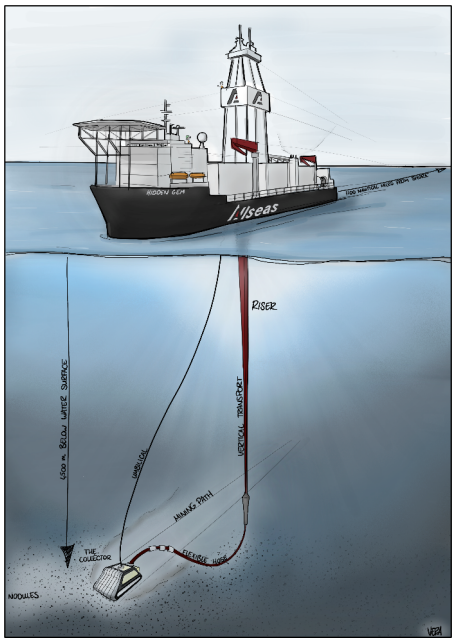

Figure 1.2: Schematic overview of the ship and collector, connected with the VTS

The main engineering challenge that occurs is that long, flexible structures in the cross-flow are susceptible to flow-induced vibrations (FIV). FIV tends to increase the magnitude of the vibrations of the structure, leading to increased cyclic stresses and therefore reduced fatigue life. In hydrodynamics, several FIV mechanisms may occur, depending on cross-sectional geometry and flow conditions. These mechanisms include vortex-induced vibrations (VIV), galloping of non-circular or asymmetric shapes, and interference-driven responses such as wake-induced vibrations (WIV) in multi-element configurations.

For design studies at the early design level, reduced-order modelling provides an expedited approach to understanding the problem by identifying the prevailing phenomena and approximating stability boundaries. These results can then be used to indicate where higher-level studies are required and to support design mitigation or accommodation as a design consideration.

1.1. Problem statement

Allseas has been testing their deep-sea mining system in a pilot project. During this pilot project, large inclination angles were observed at the top of the VTS. While some inclination can result from steady currents and self-weight, the observed angles raised additional concerns about dynamic effects and potential flow-induced instabilities that may appear. In particular, sustained oscillatory motions can lead to increased cyclic stresses, which accelerate fatigue accumulation. From a design perspective, the key risk is a regime shift. A condition may become unstable as current speed, inflow direction, or effective cross-sectional orientation changes. Although such instabilities were not necessarily observed during the pilot tests, they remain plausible and warrant screening.

A technical drawing of the cross-section of the VTS can be found in Figure 1.3. The VTS geometry can be susceptible to multiple FIV mechanisms. VIV is commonly associated with alternating vortex shedding from bluff bodies, often producing lock-in behaviour over specific reduced-velocity ranges. Galloping, in contrast, is a self-excited instability that can occur for non-circular or asymmetric cross-sections when the fluid forces introduce negative effective damping. Once initiated, the response may grow until limited by nonlinearities and may result in large amplitudes compared to VIV. In a multi-element setting, wake interference can further modify the effective inflow seen by downstream components, potentially triggering WIV or altering the stability of galloping-prone shapes. The coexistence of these phenomena complicates the interpretation. A common strategy is to separate the mechanisms for analysis and then combine them in an integrated model for prediction.

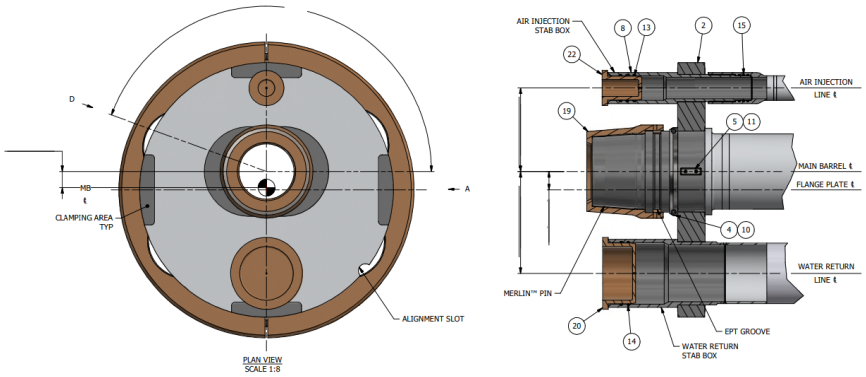

Figure 1.3: Technical drawing cross-section VTS

The main engineering problem addressed in this thesis is whether galloping-type instabilities can occur for the VTS cross-sections. During this thesis, two cross-sections will be investigated; Model 18A and Model 32A, the configurations are demonstrated in Figure 1.4. Both configurations represent rigid, in-line three-pipe bundles. These project-specific cross-sections are selected because hydrodynamic input data are available for them. This data contains quasi-steady drag, lift, and moment coefficient curves as a function of inflow orientation. The study will quantify how sensitive the predicted stability boundaries are to key modelling choices. Two challenges will be discussed in the thesis. Firstly, the applicability of galloping criteria and quasi-steady modelling approaches to the present geometry must be established. Secondly, hydrodynamic inertia effects, represented by added mass, may influence the effective natural frequency, and therefore the predicted onset of instability. The effect of different added-mass assumptions will be investigated.

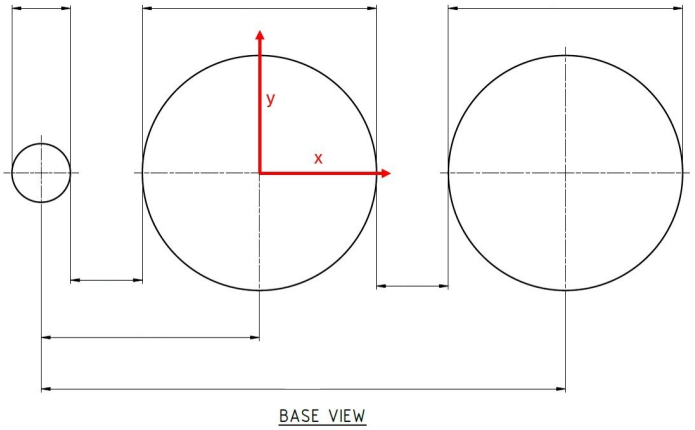

(a) Model 18A

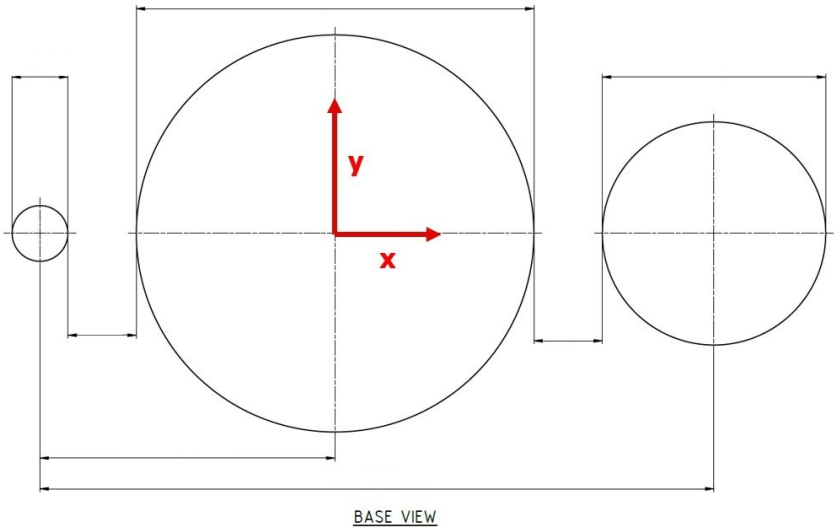

(b) Model 32A

Figure 1.4: Cross-sections used in the analysis

To address the challenges described above, this thesis uses a stepwise approach. Firstly, a benchmark model will be reproduced from a paper by Chabart and Lilien [7]. This model is first used to verify the numerical implementation and analysis workflow. The verified framework of the benchmark model is then used for the project-specific cross-sections. The cross-sectional galloping analysis is conducted for the cross-sections. Finally, the different added mass assumptions will be adopted, which enables a direct comparison of the predicted onset conditions and response magnitude for the different assumptions. The practical outcome is a set of stability predictions, sensitivity trends, and modelling insights that support decision-making on whether further high-fidelity analysis are warranted for the VTS design and operation.

1.2. Literature findings

From a literature perspective, the relevant point is that the VTS may be exposed to multiple excitation mechanisms, each with distinct onset conditions and response characteristics [8, 9]. For isolated bluff bodies, VIV is typically associated with vortex-shedding lock-in at relatively low reduced velocities [10, 11]. On the other hand, galloping is a self-excited instability that develops at higher reduced velocities and is not inherently self-limiting once negative damping is reached [8, 9]. For multi-body configurations, like riser bundles, additional wake-mediated

mechanisms can appear, where the inflow seen by a downstream element is strongly modified by upstream shedding and separation, and where interference may alter not only force magnitudes but also the qualitative form of force coefficient curves [12, 13].

A further aspect that distinguishes the present application from many classical galloping studies is the hydrodynamic character of the problem. Compared to air, the higher density of water increases the importance of inertia-related effects. Consequently, the interaction between fluid and structure is not governed by damping alone [8]. In reduced-order formulations, hydrodynamic effects enter primarily through added mass and through unsteady force contributions. As a result, the stability boundaries that are commonly evaluated from section coefficients may shift when the effective inertia and natural frequencies are modified by hydrodynamic effects [9]. Another difference is that the riser has many natural frequencies and modes, so it is unclear which modes are relevant and will be excited. Lastly, the cross-section properties of the riser vary over the length, making the analysis more difficult.

In addition, quasi-steady assumptions that are often adopted in galloping models require careful consideration for VTS-relevant cross-sections. The quasi-steady approach implies that fluid forces can be represented by static coefficient data evaluated at the instantaneous angle of attack (AOA) and relative velocity [9]. This assumption gives a good prediction for early-stage screening because it enables direct use of coefficient databases and supports systematic sensitivity studies. Within this framework, a common stability indicator is the Den Hartog criterion [8], which will be explained in more detail in Section 2.1. The Den Hartog criteria relates the onset of galloping to the slope of the lift curve and the level of drag:

$$\frac{\mathrm{d}C_L}{\mathrm{d}\alpha} + C_D < 0 \tag{1.1}$$

where α denotes the AOA and C_L and C_D are the lift and drag coefficients, respectively. Figure 1.5 shows coefficient curves $C_d(\alpha)$ and $C_l(\alpha)$, together with the lift slope $dC_l/d\alpha$ and the Den Hartog sum $H(\alpha) = dC_l/d\alpha + C_d$. The shaded interval indicates angles for which $H(\alpha) < 0$, i.e. negative quasi-steady damping and hence a galloping-susceptible orientation range.

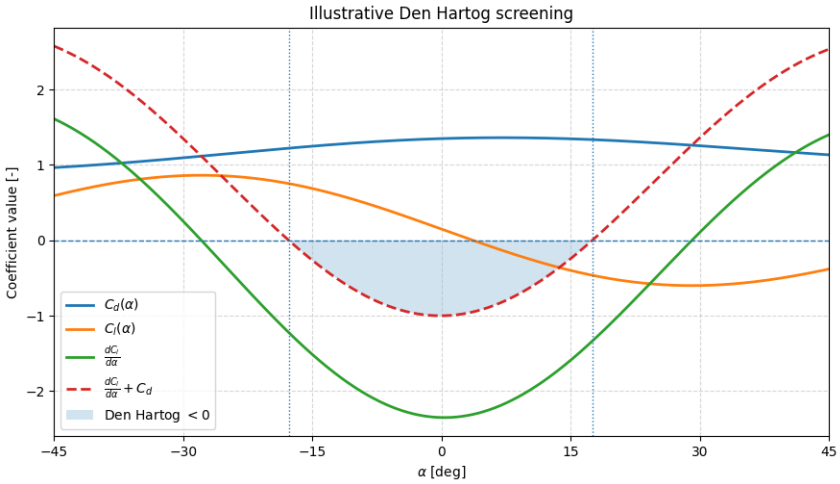

Figure 1.5: Illustrative Den Hartog Criteria with instable interval

However, quasi-steady screening also introduces modelling choices that can materially affect predicted onset conditions, such as the representation and smoothing of coefficient curves and the numerical differentiation required to evaluate stability indicators such as Equation 1.1. This becomes particularly important near marginal stability conditions, where small changes in coefficient slopes can shift the predicted onset boundaries.

For multi-pipe configurations, like the VTS, another recurring theme is that interference does not merely scale forces, but can also alter the qualitative shape of the coefficient curves with AOA [14]. This becomes especially relevant when the effective cross-section is formed by multiple closely spaced elements, where wake interaction, separation, and reattachment can create asymmetric loading even if the individual components are nominally symmetric. An implication is that galloping-like behaviour may appear depending on spacing, relative orientation, and the definition of the effective section used to represent the assembly [15].

The influence of AOA is another practical dependency that is repeatedly emphasized for bluff sections and multi-element assemblies. For square cylinders, the dominant response strongly depends on the AOA [16]. Intermediate angles can produce mixed or multi-regime behaviour. Comparable sensitivity is reported for marine-relevant cross-sections such as faired risers, where certain orientations exhibit pronounced vibration while others remain comparatively stable [17]. Similar inflow-direction dependence is also observed for riser bundle configurations [13]. For the present VTS-related configuration, this implies that stability assessment should not be based on a single nominal inflow direction. Instead, the full range of AOA should be investigated to quantify how stability indicators evolve with orientation and to identify critical angular intervals where the response will be the largest.

Finally, the treatment of added mass requires specific attention in the marine context. It directly affects the effective inertia and therefore the natural frequencies which are used in linear stability assessment and time-domain response prediction. A constant added-mass coefficient is commonly used as an assumption [18]. Doing this will provide a convenient baseline, but it assumes that inertia contributions are independent of the oscillation frequency. When unsteady effects become relevant, the effective inertia contribution can shift predicted onset boundaries when results are expressed in terms of current speed and reduced frequency.

The literature provides mature concepts for VIV, galloping screening, and qualitative descriptions of wake interference. However, transferring these ideas to a VTS-related cross-section introduces two practical gaps. First, there is limited availability of validated workflows for hydrodynamic galloping analyses that can be investigated before being applied to a new geometry. Second, there is limited guidance on how hydrodynamic inertia modelling choices influence predicted stability boundaries and response levels in simplified models. The approach in this thesis addresses these gaps by first reproducing a published galloping benchmark and then applying the same framework to the project specific cross-sections. Coefficient processing and damping are kept as explicit inputs, and the inertia model is extended with frequency-dependent added mass to assess how hydrodynamic terms affect onset and response.

1.3. Research objective and research questions

The overall goal of this thesis is to provide a step towards galloping prediction for the full riser system. The objective of this thesis is to develop and apply a cross-sectional model to predict the stability and response of the project-specific cross-sections. This cross-sectional approach is selected because the onset of galloping is primarily governed by the sectional hydrodynamic loading. This model ensures efficient parametric studies in the early design phase and provides a starting point that can be integrated at a later stage into a full-length VTS analysis. This will be more complex because a VTS contains varying cross-sections and both bending and torsion effects can play a role in the global response. The influence of added-mass modelling on the predicted onset of instability will be studied. This leads to the following research question:

To what extent can a cross-sectional galloping modelling framework be used to predict the onset and response of galloping for the project-specific cross-sections, as a basis for galloping prediction of the full VTS?

This research question will be answered by the following sub questions:

1. To what extent can a published galloping model be reproduced and used as a verified benchmark for this research?
2. What are the predicted critical flow angles for galloping of the project-specific cross-sections?
3. How does the added mass formulation affect the onset of galloping and the response amplitude?

1.4. Method overview

The methodology of this thesis follows a stepwise workflow. First, a benchmark model is set up to verify the numerical implementation against a published reference case. This verification establishes the correctness of the coefficient processing and the coupled equations of motion (EOM). The verified framework is then applied to the project-specific VTS cross-sections. The onset of instability and the post-onset response are evaluated primarily through time-domain simulations. This will be supported by Den Hartog screening to identify critical inflow-angles that are potentially susceptible to galloping. Finally, the impact of key modelling choices is quantified through a frequency-dependent added-mass comparison and targeted sensitivity studies. The workflow of the method is summarised below:

1. **Benchmark verification:** A cross-sectional galloping model is implemented based on a published reference case. The aerodynamic coefficient workflow and the coupled EOM are reproduced. The agreement with the reference is assessed using instability ranges, critical conditions, and representative time-history characteristics.
2. **Application to the case-study cross-sections:** The verified framework is adapted to the cross-sections of the VTS by updating geometric reference quantities, structural properties, and the force-coefficient representation. A cross-sectional galloping assessment is performed over the full range of inflow-angles. Den Hartog screening is used to identify unstable intervals, which are subsequently evaluated with time-domain simulations to determine critical conditions and response behaviour.
3. **Added-mass extension:** The baseline model will be extended to include alternative added-mass formulations. The effective inertia and natural frequencies are updated accordingly, and the resulting changes in predicted onset conditions and response metrics are compared with those of the other cases.
4. **Evaluation and sensitivity:** The onset of galloping is identified from time-domain simulations. This will be done by checking whether small motions grow into sustained oscillations, using consistent initial conditions and evaluation criteria. The behaviour after onset is described using the response amplitude. Sensitivity studies are performed to assess how the predictions change with stiffnesses and inflow velocity. Slow coefficient-related modelling choices will be discussed.
5. **Extension towards a 3D model:** As a next step beyond this thesis, the verified cross-sectional framework can be extended to a full-length 3D VTS/riser model. This can be done by applying the sectional hydrodynamic load along the span of a structural model of the entire VTS. Such an extension would make it possible to account for variations in cross-section and current conditions with depth, include both bending and torsion effects, and evaluate how local galloping behaviour may influence the overall system response and fatigue loading.

2

Theoretical framework and method

FIV are structural oscillations driven by unsteady fluid loading. This thesis focuses on galloping, a self-excited instability that may occur for non-circular or asymmetric cross-sections in steady inflow. Galloping arises when fluid forces act with negative effective damping, causing small perturbations to grow. This chapter presents the galloping stability criterion, the governing equations adopted for the cross-sectional model used in the numerical investigations, and the numerical workflow used to verify and apply the model.

2.1. Galloping instability criterion

Galloping can be described as a self-excited cross-flow instability, commonly observed for non-circular or asymmetric sections. In the approach of Blevins [8], the unsteady fluid loading is approximated using quasi-steady aerodynamics. The force on the moving body is taken equal to the steady force measured for the same instantaneous effective angle of attack and relative speed. Linearizing this force model around a mean operating condition yields a velocity-proportional fluid term that may act as negative effective damping. The onset of galloping is then predicted by the sign of an aerodynamic slope parameter, referred to as the Den Hartog criterion. The quasi-steady approximation is most appropriate when the aerodynamic loading adjusts much faster than the structural motion. This happens when the reduced frequency is small and the instantaneous flow can be regarded as locally steady. In this limit, the unsteady force is dominated by the change in the effective direction of the inflow caused by body motion rather than by vortex shedding dynamics. Consequently, the linearized quasi-steady model is primarily an onset predictor. It indicates whether small perturbations are expected to grow, but it does not predict post-onset amplitudes, which are typically governed by nonlinear aerodynamic and structural effects.

2.1.1. Quasi-steady force formulation for 1DOF

In Blevins [8], the rigid cross-section shown in Figure 2.1 is considered. The section is elastically supported in cross-flow direction. The steady lift and drag are written as:

$$F_L = \tfrac{1}{2}\rho U^2 D\, C_L(\alpha) \tag{2.1}$$

$$F_D = \tfrac{1}{2}\rho U^2 D\, C_D(\alpha) \tag{2.2}$$

where ρ is the fluid density, D is a characteristic width normal to the mean flow, U_{rel} is the relative speed, and $C_L(\alpha)$ and $C_D(\alpha)$ are aerodynamic coefficients as functions of effective angle of attack α.

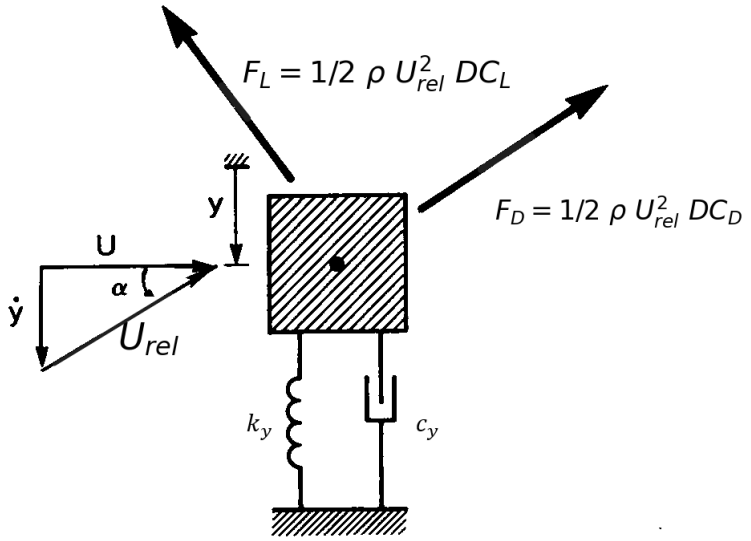

Figure 2.1: One-degree-of-freedom galloping model, adapted from Blevins [8].

The cross-flow resultant force can be expressed as:

$$F_y \;=\; \tfrac{1}{2}\rho U^2 D\, C_y(\alpha) \tag{2.3}$$

with $C_y(\alpha)$ obtained by resolving lift and drag into the cross-flow direction. For small motions, the effective angle of attack is governed primarily by the ratio of cross-flow velocity to mean flow speed. The structural equation of motion is given by:

$$m\ddot{y} + c_y\dot{y} + k_y y \;=\; F_y \tag{2.4}$$

where m is the mass per unit span, c_y is the damping, and k_y is the stiffness. In the literature, linearization is performed about the reference state $\alpha = 0$. Expanding the aerodynamic coefficient in a Taylor series about $\alpha = 0$ gives:

$$C_y(\alpha) \;=\; C_y(0) + \left.\frac{\partial C_y}{\partial \alpha}\right|_0 \alpha + \mathcal{O}(\alpha^2) \tag{2.5}$$

By combining the above equations and using the small-angle approximation $\dot{y} = U\alpha$, the following expression is obtained:

$$m\ddot{y} + \left(c_y + \tfrac{1}{2}\rho U D \left.\frac{\partial C_y}{\partial \alpha}\right|_0\right)\dot{y} + k_y y \;=\; \tfrac{1}{2}\rho U^2 D\, C_y(0) \tag{2.6}$$

The term on the right-hand side of Equation 2.6 is a constant mean force that produces a static offset of the equilibrium position. For linear stability considerations, it is common to shift the coordinate y to static equilibrium so that the forcing term vanishes. The galloping criterion is then governed solely by the sign of the effective damping term multiplying $\dot{y}$. With the natural frequency $\omega_y = \sqrt{k_y/m}$ and structural damping ratio $\zeta_y = c/(2m\omega_y)$, Equation 2.6 can be written as:

$$m\ddot{y} + 2m\omega_y\zeta_{\text{net}}\,\dot{y} + k_y y \;=\; \tfrac{1}{2}\rho U^2 D\, C_y(0) \tag{2.7}$$

with the net effective damping ratio:

$$\zeta_{\text{net}} \;=\; \zeta_y \;+\; \frac{\rho U D}{4m\omega_y}\left.\frac{\partial C_y}{\partial \alpha}\right|_0 \tag{2.8}$$

Galloping onset corresponds to $\zeta_{\text{net}} = 0$ and instability occurs when $\zeta_{\text{net}} < 0$.

2.1.2. Den Hartog-type criterion in terms of aerodynamic slopes

The slope of the vertical force coefficient can be related to lift and drag slopes. A commonly used approximation gives:

$$\left.\frac{\partial C_y}{\partial \alpha}\right|_0 = -\left(\left.\frac{\partial C_L}{\partial \alpha}\right|_0 + C_D(0)\right) \tag{2.9}$$

Equation 2.9 follows from rewriting the lift and drag into the transverse direction and linearizing for small α. The appearance of $C_D(0)$ reflects the fact that a small inclination of the drag vector contributes to a transverse component proportional to the mean drag. Consequently, even if $\partial C_L/\partial \alpha$ is weak, sufficiently large drag can stabilize the motion, whereas a negative $\partial C_L/\partial \alpha$ combined with moderate drag may lead to the destabilizing condition in Equation 2.10. The instability condition can then be expressed as:

$$\zeta_{\text{net}} < 0 \quad \Longleftrightarrow \quad \left.\frac{\partial C_y}{\partial \alpha}\right|_0 > 0 \quad \Longleftrightarrow \quad \left.\frac{\partial C_L}{\partial \alpha}\right|_0 + C_D(0) < 0 \tag{2.10}$$

where the last form is the classical Den Hartog criterion. The inequality $\left.\frac{\partial C_L}{\partial \alpha}\right|_0 + C_D(0) < 0$ is an onset indicator for negative aerodynamic damping. It is therefore a necessary condition for 1DOF galloping. The actual stability limit also depends on structural damping. For a given operating condition, the boundary is reached when the net damping becomes zero. This gives the critical velocity U_{crit} in Equation 2.11. For $U < U_{\text{crit}}$ small perturbations decay. For $U > U_{\text{crit}}$ small perturbations grow until nonlinearities limit the response.

2.1.3. Critical flow velocity

Setting $\zeta_{\text{net}} = 0$ in Equation 2.8 gives the critical velocity for onset of 1DOF galloping:

$$U_{\text{crit}} = \frac{4m\omega_y\zeta_y}{\rho D}\left(\left.\frac{\partial C_y}{\partial \alpha}\right|_0\right)^{-1} \tag{2.11}$$

Expressed as a reduced velocity using $f_y = \omega_y/(2\pi)$,

$$\frac{U_{\text{crit}}}{f_y D} = \frac{8\pi m\zeta_y}{\rho D^2}\left(\left.\frac{\partial C_y}{\partial \alpha}\right|_0\right)^{-1} \tag{2.12}$$

Sections with a destabilizing slope $\left.\partial C_y/\partial\alpha\right|_0 > 0$ possess a finite positive U_{crit}, otherwise the motion is linearly stable with respect to galloping.

2.1.4. Two-degree-of-freedom galloping

Many sections can both translate and rotate. These motions are coupled through the effective angle of attack. A convenient 2DOF quasi-steady model for the cross-section in Figure 2.2 is given by Blevins [8]:

$$m\ddot{y} + 2m\zeta_y\omega_y\dot{y} + k_y y + S_x\ddot{\theta} = \tfrac{1}{2}\rho U^2 D\, C_y(\alpha) \tag{2.13}$$

$$J_\theta\ddot{\theta} + 2J_\theta\zeta_\theta\omega_\theta\dot{\theta} + k_\theta\theta + S_x\ddot{y} = \tfrac{1}{2}\rho U^2 D^2\, C_M(\alpha) \tag{2.14}$$

where θ is the torsion about the elastic axis, $C_M(\alpha)$ is the moment coefficient, and S_x represents inertial coupling. k_y and k_θ represent the structural damping terms. The coupling terms $S_x\ddot{\theta}$ and $S_x\ddot{y}$ represent inertial coupling between translation and rotation due to an offset between the elastic axis and the mass center. In addition, because the effective angle of attack depends on both $\dot{y}$ and θ, the aerodynamic forcing introduces cross-coupled damping and stiffness contributions in the linearized system. As a result, the 2DOF stability boundary is generally obtained by forming the linearized coupled system and determining when an eigenvalue crosses into the unstable region.

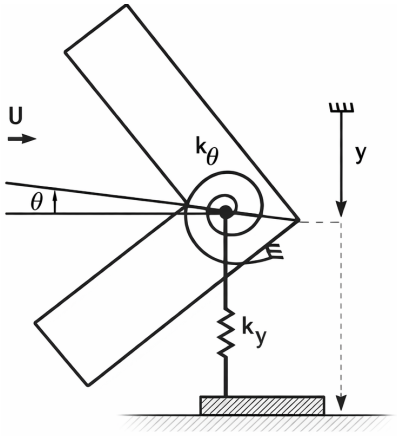

Figure 2.2: Two-degree-of-freedom galloping model, adapted from Blevins [8].

2.1.5. Stability limit for multi-DOF galloping

When torsion or in-line motion is included, the Den Hartog function is no longer a complete stability criterion. It can be used as a screening tool, but the stability boundary must be obtained from the linearised coupled system [19–21]. Physically, torsion makes the effective angle of attack dynamic. It also introduces aerodynamic coupling through the moment coefficient and its slope [19]. This coupling can shift, widen, or narrow the instability regions predicted from 1DOF screening [20, 21]. Coupled translational–torsional galloping may occur even when the 1DOF screening is only weakly unstable [20, 22]. In more detuned cases, the response may remain mainly translational with only limited torsional participation [19, 20].

2.1.6. Applying the criterion using lift and drag coefficient data

In practice, $C_L(\alpha)$, $C_D(\alpha)$ and $C_M(\alpha)$ are obtained from steady measurements or CFD. The indicator of the onset of galloping is then evaluated from the local slope $\partial C_L/\partial\alpha|_\alpha$ and the corresponding drag $C_D(\alpha)$ at the operating angle α. The linear prediction identifies ranges of α for which $\partial C_L/\partial\alpha|_\alpha + C_D(\alpha) < 0$, indicating negative aerodynamic damping and potential onset of galloping. It should be emphasized that the Den Hartog criterion is an onset criterion derived from a local linearization. Since $C_L(\alpha)$ and $C_D(\alpha)$ are generally nonlinear, a given section may exhibit both stable and unstable angle ranges, and the final oscillation amplitude after onset cannot be predicted by the linear model. Post-onset behaviour typically requires nonlinear time-domain simulation or experimental validation, as growth is ultimately limited by nonlinearities in the aerodynamic coefficients and structural response.

2.2. Governing equations of the cross-sectional model

The governing model equations used in this thesis are based on the formulations by Blevins [8]. These have been rewritten and adapted to the present problem: a 2D cross-section in uniform inflow that may translate in both directions and rotate about its origin. The three cylinders are assumed to form a rigid bundle, i.e. they do not move relative to each other and their mutual spacing is fixed. The coupled mechanical model is combined with a quasi-steady loading model in which the hydrodynamic coefficients are evaluated at the effective angle of attack. The quasi-steady coefficient data are obtained from an internal Marin report, in which steady inflow CFD simulations were performed for a rigid three-cylinder cross-section placed in a uniform current. In these simulations, the cylinders were fixed, without structural motion, and the force and moment coefficients were extracted as time-averaged values from the simulations. The coefficients are provided for discrete inflow angles in increments of $15°$. An overview of the cross-sectional free-body model is shown in Figure 2.3.

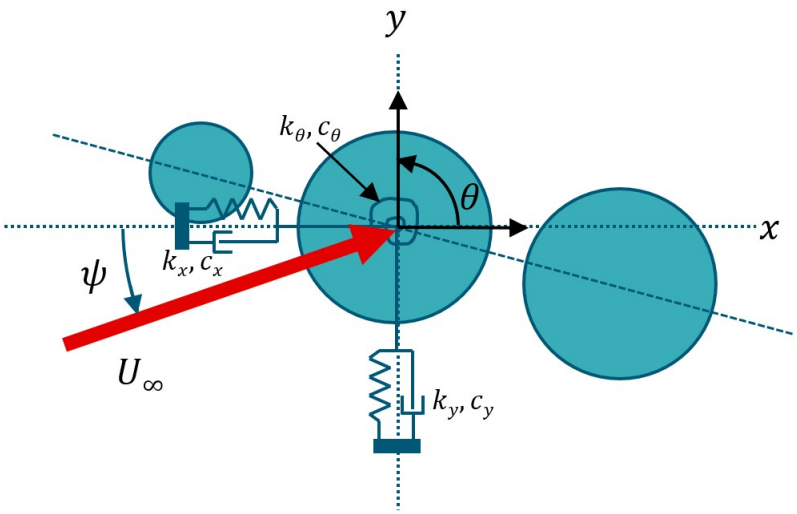

Figure 2.3: Free-body model of the cross-sectional system.

2.2.1. Kinematics and coordinate system

A 2D cross-section is considered in a uniform inflow. The structural motion is described in the global Cartesian directions denoted by $x(t)$ and $y(t)$. The inflow velocity magnitude is denoted by U.

In general, the incoming flow may approach the section under an angle ψ with respect to the x-axis. The free-stream velocity vector is:

$$\mathbf{U}_\infty = U \begin{bmatrix} \cos\psi \\ \sin\psi \end{bmatrix} \tag{2.15}$$

The instantaneous relative velocity $\mathbf{U}_{\text{rel}}$ is defined as the difference between the free-stream velocity and the structural velocity:

$$\mathbf{U}_{\text{rel}}(t) = \mathbf{U}_\infty - \begin{bmatrix} \dot{x}(t) \\ \dot{y}(t) \end{bmatrix} = \begin{bmatrix} U\cos\psi - \dot{x}(t) \\ U\sin\psi - \dot{y}(t) \end{bmatrix}, \qquad U_{\text{rel}}(t) = \|\mathbf{U}_{\text{rel}}(t)\| \tag{2.16}$$

The effective direction of the relative flow with respect to the x-axis is:

$$\beta(t) = \arctan\left(\frac{U\sin\psi - \dot{y}(t)}{U\cos\psi - \dot{x}(t)}\right) \tag{2.17}$$

The hydrodynamic coefficients are defined with respect to the body. The section rotates by $\theta(t)$ about its reference point. In the remainder of this thesis, $\alpha(t)$ is used to evaluate the quasi-steady force coefficients and corresponding hydrodynamic forces. The effective angle of attack seen by the body is defined as:

$$\alpha(t) = \beta(t) - \theta(t) \tag{2.18}$$

2.2.2. Structural model and equations of motion

The motion is modelled in the cross-sectional plane with two translational degrees of freedom, $x(t)$ and $y(t)$, and one rotational degree of freedom $\theta(t)$. Structural restoring and damping forces are represented by linear stiffness and viscous damping. The equations of motion are:

$$(m + m_{a,x})\,\ddot{x} + c_x\dot{x} + k_x x = F_x(x, y, \theta, t) \tag{2.19}$$

$$(m + m_{a,y})\,\ddot{y} + c_y\dot{y} + k_y y = F_y(x, y, \theta, t) \tag{2.20}$$

$$(I_\theta + I_{a,\theta})\,\ddot{\theta} + c_\theta\dot{\theta} + k_\theta\theta = M(x, y, \theta, t) \tag{2.21}$$

where m is the structural mass, I_θ is the structural mass moment of inertia about the out-of-plane axis, and $c_{x,y,\theta}$ and $k_{x,y,\theta}$ are damping and stiffness coefficients. The terms $m_{a,x}$, $m_{a,y}$ and $I_{a,\theta}$ denote ideal inertia terms which are relevant for the hydrodynamic case. The fluid loads are denoted by the in-line and cross-flow forces F_x and F_y, and the torsional moment M about the reference point. The natural frequencies are:

$$\omega_{n,x} = \sqrt{\frac{k_x}{m + m_{a,x}}}, \qquad \omega_{n,y} = \sqrt{\frac{k_y}{m + m_{a,y}}}, \qquad \omega_{n,\theta} = \sqrt{\frac{k_\theta}{I_\theta + I_{a,\theta}}} \tag{2.22}$$

Using damping ratios ζ_x, ζ_y, and ζ_θ, the damping coefficients are defined as:

$$c_x = 2\,\zeta_x\,(m + m_{a,x})\,\omega_{n,x}, \qquad c_y = 2\,\zeta_y\,(m + m_{a,y})\,\omega_{n,y}, \qquad c_\theta = 2\,\zeta_\theta\,(I_\theta + I_{a,\theta})\,\omega_{n,\theta} \tag{2.23}$$

2.2.3. Added mass modelling

Hydrodynamic inertia is represented through translational added mass. A common simplification is to treat the added mass as constant, using an added-mass coefficient (often $C_a = 1$). In this thesis, to improve accuracy for submerged bodies, the added mass is treated as direction-dependent and, in addition, as frequency-dependent. The translational added mass is defined in body axes, where it is assumed diagonal but anisotropic:

$$\mathbf{M}_{a,\text{body}} = \begin{bmatrix} C_{a,x}\,m_{xx0} & 0 \\ 0 & C_{a,y}\,m_{yy0} \end{bmatrix} \tag{2.24}$$

where m_{xx0} and m_{yy0} denote baseline added-mass terms.

In the numerical model, the added-mass matrix is rotated to the global frame using the instantaneous orientation $\theta(t)$, which yields an orientation-dependent translational inertia and, in general, coupling between the x- and y-accelerations through off-diagonal terms.

To obtain baseline added-mass terms for the present three-pipe configuration, the cross-section is approximated by an equivalent ellipse. The resulting added-mass expressions are based on the elliptic airfoil formulation reported by [23]. The ellipse axes are taken from the outer dimensions of the cross-section, such that the major and minor axis lengths are defined as c_{eq} and b_{eq}, as shown in Figure 2.4.

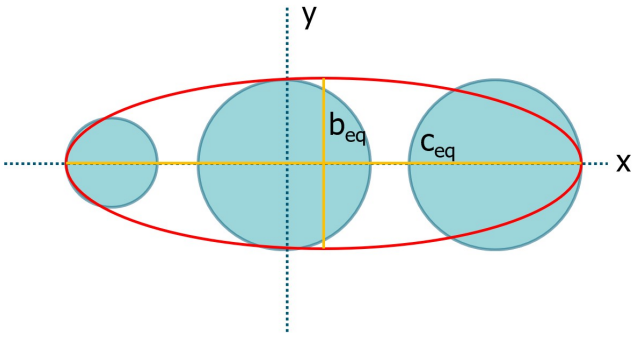

Figure 2.4: Equivalent ellipse formulation used to define baseline added-mass terms.

The baseline added-mass terms for a cross-sectional slice of length L become:

$$m_{xx0} = \frac{\pi\rho}{4} b_{\text{eq}}^2 L, \qquad m_{yy0} = \frac{\pi\rho}{4} c_{\text{eq}}^2 L \tag{2.25}$$

In this thesis, $C_{a,x}$ and $C_{a,y}$ are not treated as constants, but may depend on the oscillation frequency through a literature-based $C_a(f^*)$ relation. The chosen $C_a(f^*)$ curve and its numerical implementation are described in Section 2.2.4.

2.2.4. Frequency-dependent added mass implementation

Experimental studies on elastically mounted cylinders in steady current show that the added-mass coefficient varies strongly with reduced velocity and may become negative at higher reduced velocities [24, 25]. The mean trend reported by Vikestad et al. [25] is therefore used as a literature-based sensitivity model for frequency-dependent inertia. In this paper, f_0 denotes the natural frequency measured in still water (including the still-water added mass, reported as $C_a \approx 1.04$), which is used as a fixed reference frequency to define the reduced velocity $U_r = U_\infty/(f_0 D)$. This avoids a circular definition, since the true natural frequency in current depends on the added mass, which itself varies with U_r.

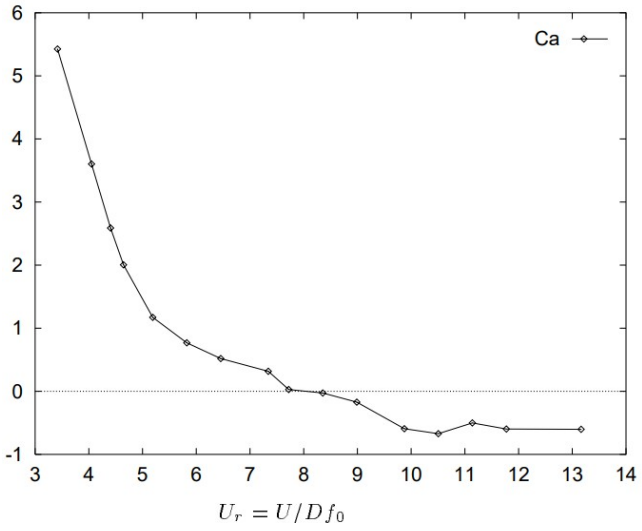

Figure 2.5: Mean added-mass coefficient C_a as a function of reduced velocity $U_r = U/(f_0 D)$ for a freely vibrating circular cylinder in steady current (adapted from Vikestad et al. [25], Fig. 4a).

To implement the relation shown in Figure 2.5 in the numerical model, the curve is expressed in terms of reduced frequency f^* rather than reduced velocity. Using:

$$f^* = \frac{f D_{\text{ref}}}{U_\infty}, \qquad U_r = \frac{U_\infty}{f D_{\text{ref}}} = \frac{1}{f^*} \tag{2.26}$$

the digitised data are rewritten as $C_a(f^*)$ and interpolated to obtain a continuous relation. Figure 2.6 shows the data and the resulting interpolation used in the model. In the model, $C_{a,x}$ and $C_{a,y}$ are updated each timestep.

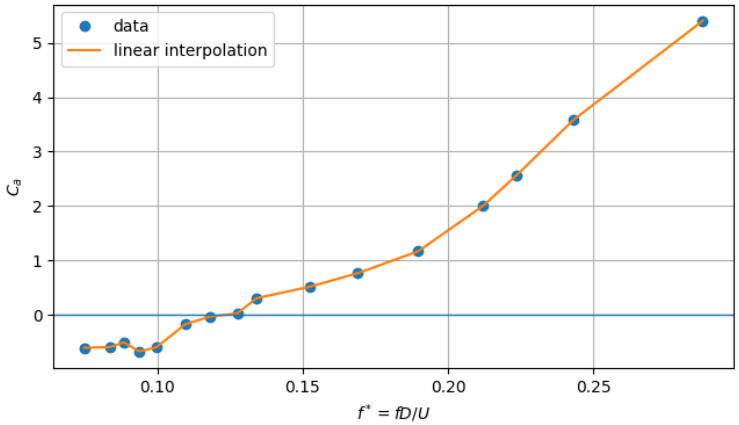

Figure 2.6: Added-mass data from Figure 2.5 rewritten as $C_a(f^*)$ and interpolated for use in the numerical model.

2.2.5. Quasi-steady hydrodynamic forces

In the quasi-steady approach, the fluid forces are expressed using static force coefficients evaluated at the instantaneous angle of attack $\alpha(t)$. Using the coefficients, the relative velocity, and a characteristic width D, the lift and drag forces are:

$$F_D(t) = \frac{1}{2}\rho U_{\mathrm{rel}}^2(t)\, D\, C_D(\alpha(t)) \tag{2.27}$$

$$F_L(t) = \frac{1}{2}\rho U_{\mathrm{rel}}^2(t)\, D\, C_L(\alpha(t)) \tag{2.28}$$

where ρ is the fluid density, and $C_D(\alpha)$ and $C_L(\alpha)$ are the drag and lift coefficients. The model uses the global x and y axes. Transforming lift and drag to these axes gives:

$$F_x(x, y, \theta, t) = -F_D(t)\cos\alpha(t) + F_L(t)\sin\alpha(t) \tag{2.29}$$

$$F_y(x, y, \theta, t) = \quad F_D(t)\sin\alpha(t) + F_L(t)\cos\alpha(t) \tag{2.30}$$

2.3. Numerical method

The governing equations and quasi-steady loading model introduced in Sections 2.1–2.2 are implemented in a time-domain solver. The implementation is first verified against a published galloping benchmark model. After verification, the framework is applied to the case-study cross-sections through systematic sweeps in inflow angles. Finally, multiple added-mass formulations are compared in order to quantify their influence on predicted galloping onset and post-onset response characteristics.

2.3.1. Research workflow

The numerical study consists of the following steps:

1. **Model implementation:** The coupled equations of motion are implemented together with the quasi-steady force model. Static force and moment coefficients are provided as functions of the angle of attack and are evaluated at the instantaneous effective angle $\alpha(t)$ using curves of the available data.
2. **Benchmark verification:** The solver is verified by reproducing a published galloping benchmark. The agreement is assessed using reported instability ranges and representative response time histories.
3. **Case-study application:** The verified model is adapted to the thesis cross-sections by updating the geometry, structural parameters, and coefficient data. Inflow-angle sweeps are performed to identify critical operating conditions.
4. **Model-variant comparison:** Added mass is treated as zero, constant ($C_a = 1$), and frequency-dependent according to Section 2.2.4. The resulting changes in the onset conditions and response metrics are quantified.

2.3.2. Numerical experiment setup and evaluation

For each configuration, the inflow velocity U_∞ is prescribed and fixed to the value considered in the Marin report ($U_\infty = 0.45\,\mathrm{m/s}$). For both cross-sections, the analysis is carried out in two complementary steps:

- **Screening for susceptible angles:** The Den Hartog criteria is evaluated using the processed coefficient curves to identify angular intervals that are prone to negative hydrodynamic damping. These intervals define the priority cases for time-domain simulations.
- **Time-domain confirmation and quantification:** The full nonlinear equations are integrated in time from a small perturbation about the equilibrium state. The response is classified as stable or galloping and response amplitudes are extracted.

Galloping onset is identified from the time-domain response as the transition from decaying motion to sustained oscillations. The objective of this procedure is to determine whether small perturbations grow under quasi-steady loading and, if so, to quantify the resulting post-onset response.

2.3.3. Time-domain response simulations

For each velocity U_∞, the nonlinear equations Equation 2.19–Equation 2.21 are integrated in time using the quasi-steady force model described in Section 2.2.5. The responses can be classified as:

- **Stable:** the perturbation decays and the motion returns to equilibrium.
- **Unstable (galloping):** the motion grows from the perturbation and evolves towards significant oscillation.

From the final part of the time histories the response amplitudes (peak-to-peak) are extracted for comparison across inflow angles and different added-mass formulations.

2.3.4. Benchmark verification

The benchmark verification reproduces a published galloping case to validate the implementation of the effective angle of attack, the applicability and evaluation of static coefficient data, and the coupled time-domain response characteristics. Upon demonstrating satisfactory agreement with the published benchmark, the modelling framework is transferred to the project-specific cross-sections for the analyses.

2.4. Assumptions, scope, and limitations

The theoretical and numerical framework adopted in this thesis relies on the following main assumptions and limitations:

- **Cross-sectional modelling:** The structure is represented by a rigid 2D cross-section; three-dimensional effects, spanwise variability, and end conditions are neglected.
- **Quasi-steady loading:** Hydrodynamic forces are evaluated from static coefficient data at the instantaneous effective angle of attack; unsteady effects are not explicitly modeled.
- **Linear structural properties:** Structural stiffness and viscous damping are assumed constant.
- **Idealized inflow:** The inflow is taken as steady and uniform; turbulence, shear, inflow unsteadiness, and wave-induced kinematics are neglected.
- **Dependence on coefficient data:** Prediction quality depends on the applicability, accuracy, and angle-of-attack coverage of the static coefficients, as well as interpolation choices.
- **Added-mass simplifications:** Added mass is represented through constant or frequency-dependent coefficients; strong amplitude- or history-dependence and other nonlinear inertia effects are not represented.

These assumptions define the scope of validity of the results and are revisited in the discussion when interpreting outcomes and recommending future work.

3

Benchmark model reproduction

This chapter verifies the numerical implementation by reproducing a published galloping study. A two-dimensional lumped-parameter model is implemented following the wind-tunnel experiment of Chabart and Lilien [7] on an iced transmission-line conductor. The chapter evaluates the instability ranges predicted from the measured aerodynamic coefficients and time-domain responses for two representative operating cases reported in the reference study.

3.1. Benchmark configuration

The benchmark model used in this study is based on the wind–tunnel experiment of Chabart and Lilien, in which an iced overhead line conductor is represented by an ice accretion mounted on a rigid tube. The outside layer of a stranded conductor is placed on an aluminium tube of appropriate diameter, and an artificial, highly eccentric ice shape is cast around it. The resulting ice-covered section forms a straight sample. The tube can rotate about its longitudinal axis so that the ice accretion can be positioned at different angular orientations θ with respect to the oncoming flow, thereby allowing systematic variation of the effective angle of attack.

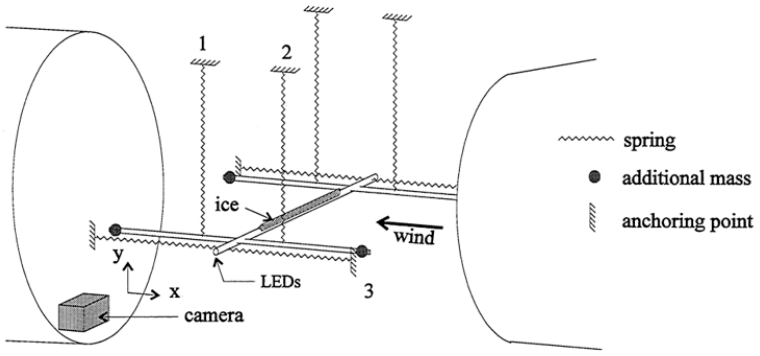

Figure 3.1: Set-up used in paper [7]

For the dynamic galloping tests, the iced tube is suspended in a rectangular frame using multiple springs, such that horizontal, vertical, and torsional motion are all permitted. Four horizontal springs provide lateral flexibility, while four vertical springs support the weight of the structure and define the vertical stiffness. The torsional stiffness of the system is controlled by the distance between the vertical springs and the center of the sample. Increasing this distance raises the rotational stiffness and frequency, whereas reducing the distance, lowers the torsional frequency. The motion of the sample is recorded using a camera-based tracking system, which allows an accurate reconstruction of the 3DOF over time.

Aerodynamic coefficients are obtained in a separate configuration in which the sample is rigidly supported and connected to force transducers. Two vertical dynamometers measure the resultant vertical force and pitching moment, while a horizontal dynamometer measures the drag force. For each angular position θ, the forces are recorded over a period of one minute and averaged, this procedure is repeated several times to improve repeatability. The AOA is varied over a full revolution in increments of 5°, and the procedure is repeated for several wind speeds in the range relevant for galloping. The resulting lift, drag, and moment coefficients show only a weak dependence on wind speed for the majority of angles, which supports the use of a quasi-steady aerodynamic model in the subsequent cross-sectional galloping analysis.

3.2. Instability ranges

The aerodynamic force coefficients obtained from the wind–tunnel measurements were provided as discrete values of the lift, drag, and moment coefficients, $C_L(\alpha)$, $C_D(\alpha)$, and $C_M(\alpha)$, as functions of the angle of attack α. In order to obtain smooth, differentiable representations suitable for stability analysis, these data were approximated by a fitted Fourier series of the form:

$$C_k(\alpha) \approx a_0^{(k)} + \sum_{n=1}^{N} \left[a_n^{(k)} \cos(n\alpha) + b_n^{(k)} \sin(n\alpha) \right], \qquad k \in \{L, D, M\} \tag{3.1}$$

where α is expressed in radians and N denotes the number of harmonics retained. This representation captures the periodic dependence of the coefficients on α and allows the derivative $\mathrm{d}C_L/\mathrm{d}\alpha$ to be evaluated analytically, in contrast to a finite–difference approximation on noisy experimental data.

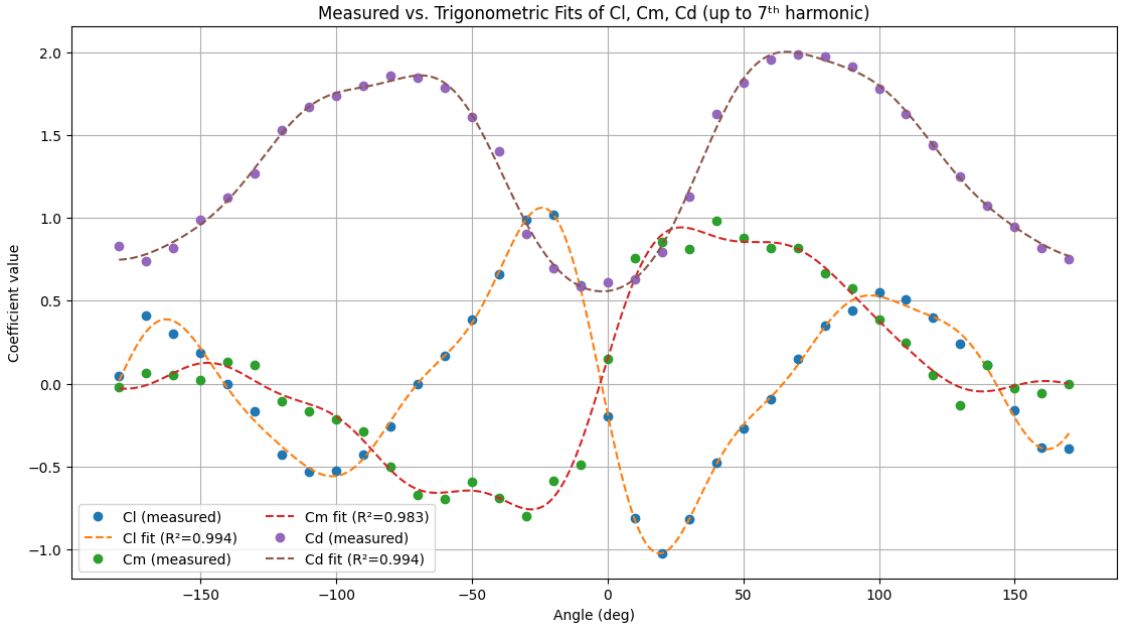

Figure 3.2: Fourier curve fitting experimental data

Following Den Hartog, the propensity of the section to gallop in vertical motion is assessed by means of the Den Hartog criteria presented earlier:

$$H(\alpha) = \frac{\mathrm{d}C_L}{\mathrm{d}\alpha} + C_D(\alpha) \tag{3.2}$$

where, for the present sign convention, negative values of $H(\alpha)$ correspond to negative aerodynamic damping and therefore indicate potentially unstable ranges of angle of attack.

It is noted that the Den Hartog function is a 1DOF onset indicator derived for pure transverse motion with a fixed section orientation. However the wind–tunnel set-up permits coupled translation and torsional rotation. In a coupled system the effective angle of attack is not prescribed but becomes dynamic through $\alpha = h_0 + \theta + \beta$, and the stability problem is governed by the eigenvalues of the full aeroelastic system [19–21]. As a consequence, the regions where the Den Hartog criteria is negative should be interpreted here as preliminary, quasi-static potential galloping ranges. When torsion is allowed, the rotation $\theta(t)$ can modify $\alpha(t)$ and introduce additional aerodynamic damping and stiffness couplings through the moment coefficient and its slope. This means that the actual stability boundary of the coupled 3DOF system may vary compared to the 1DOF prediction [19, 26, 27]. For this reason, the Den Hartog plot is used below to identify likely unstable orientations, while the final verification of instability and response type is performed using the full 3DOF time-domain simulations reported in the subsequent sections.

The distributions of C_D, $\mathrm{d}C_L/\mathrm{d}\alpha$ and $H(\alpha)$ resulting from the Fourier fit are shown in Figure 3.3. The zero-crossings of $H(\alpha)$ in the interval $-180^\circ \leq \alpha \leq 0^\circ$ are found at:

$$\alpha = -163.68^\circ, \quad \alpha = -45.64^\circ, \quad \alpha = -23.24^\circ$$

Consequently, the Den–Hartog function is negative in the ranges:

$$-180^\circ < \alpha < -163.68^\circ, \qquad -45.64^\circ < \alpha < -23.24^\circ$$

which defines two distinct instability intervals. These correspond to one unstable region centered near $\alpha \approx -180^\circ$ and a second one centered around $\alpha \approx -35^\circ$, in good agreement with the two unstable areas reported in the original experiment.

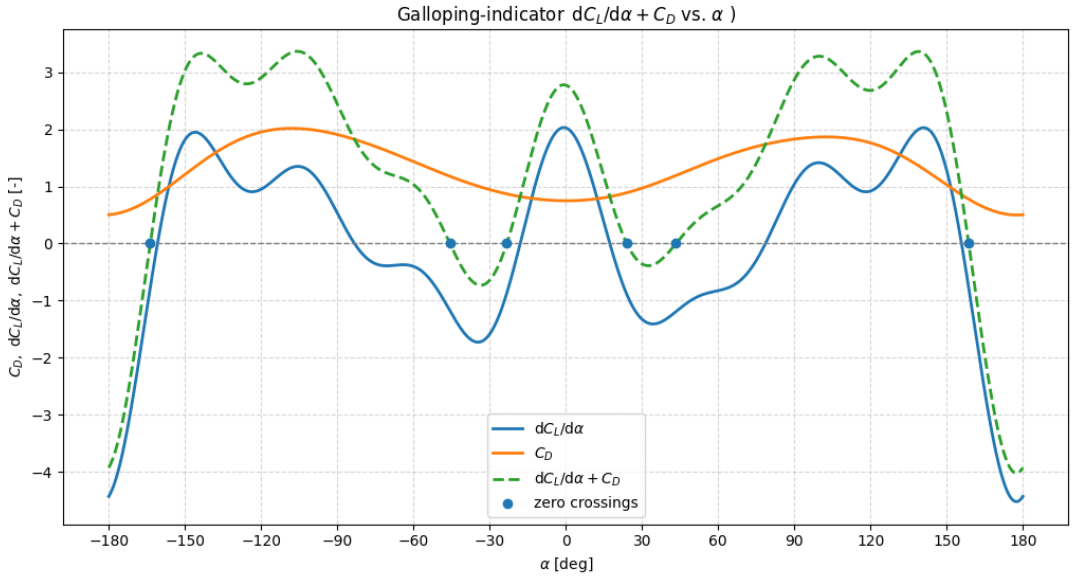

Figure 3.3: Den Hartog criteria reproduction

3.3. Governing equations and input data

The benchmark model is recreated by a lumped–parameter system with three degrees of freedom. These are horizontal translation $x(t)$, vertical translation $y(t)$ and rotation $\theta(t)$ of the iced section about its center. The schematic free body diagram (FBD) can be found in Figure 3.4. The wind tunnel flow is assumed to be uniform with speed U in the global x–direction. Due to the motion of the body, the section experiences a relative flow with components:

$$V_x = U + \dot{x}, \qquad V_y = \dot{y} \tag{3.3}$$

With magnitude:

$$U_r = \sqrt{V_x^2 + V_y^2} \tag{3.4}$$

The corresponding inflow angle β of the relative velocity, measured from the x–axis, is given by:

$$\beta = \tan^{-1}\left(\frac{V_y}{V_x}\right) \tag{3.5}$$

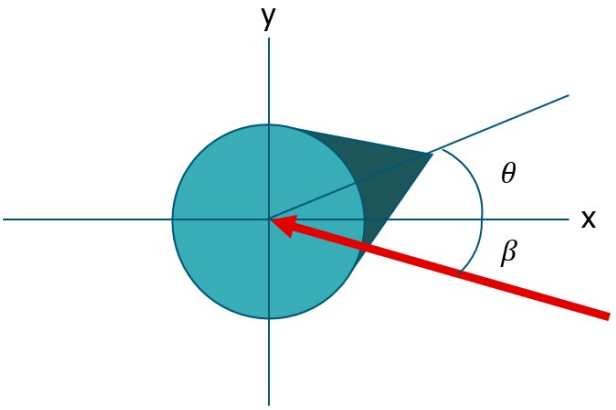

Figure 3.4: Schematic FBD PTL reproduction paper

The ice accretion itself is not aligned with the tube axis but has a fixed geometric offset angle h_0. Together with the structural rotation θ and the instantaneous inflow angle β, this defines the effective aerodynamic angle of attack

$$\alpha = h_0 + \theta + \beta \tag{3.6}$$

This angle α is used to evaluate the aerodynamic coefficients $C_D(\alpha)$, $C_L(\alpha)$ and $C_M(\alpha)$ obtained from the wind–tunnel measurements.

Under the quasi-steady assumption, the aerodynamic forces per unit span are expressed in terms of these coefficients and the relative velocity. For a section of diameter d and spanwise length L, the total aerodynamic forces in the x and y directions and the pitching moment about the section centre are written as:

$$F_x = \frac{1}{2}\rho U_r^2 dL\left[-C_D(\alpha)\cos\beta + C_L(\alpha)\sin\beta\right] \tag{3.7}$$

$$F_y = \frac{1}{2}\rho U_r^2 dL\left[-C_D(\alpha)\sin\beta - C_L(\alpha)\cos\beta\right] \tag{3.8}$$

$$M = \frac{1}{2}\rho U_r^2 d^2 L\, C_M(\alpha) \tag{3.9}$$

where ρ is the air density. The drag component acts opposite to the relative flow direction, while the lift component acts normal to it. The above projections account for the chosen sign convention of F_x and F_y.

The structural dynamics of the suspended frame are modelled by linear mass–spring–damper relations in each degree of freedom:

$$m\ddot{x} + c_x\dot{x} + k_x x = F_x \tag{3.10}$$

$$m\ddot{y} + c_y\dot{y} + k_y y = F_y \tag{3.11}$$

$$I_\theta\ddot{\theta} + c_\theta\dot{\theta} + k_\theta\theta = M \tag{3.12}$$

where m denotes the mass of the oscillating system, I_θ its polar moment of inertia, and c_x, c_y, c_θ, k_x, k_y, k_θ are the corresponding damping and stiffness coefficients. These coupled equations of motion form the basis for the subsequent stability and time-domain galloping analyses of the benchmark model.

The structural properties of the experimental set-up are adopted from the measurements reported for the iced-conductor test rig. These values are summarised in Table 3.1 and are used to define the mass, damping and stiffness parameters in the governing equations.

Total mass m	$2.99\ \mathrm{kg}$
Ice-covered length L	$0.80\ \mathrm{m}$
Critical damping ratio (x, y)	0.08%
Critical damping ratio (rotation)	0.30%

Table 3.1: Structural properties used in the benchmark simulations. [7]

In the original study, the structural parameters that are systematically varied are the translational and rotational stiffnesses k_x, k_y and k_θ, in order to adjust the natural frequencies and investigate different coupling conditions between translation and rotation. Consequently, these stiffnesses are treated in the present work as control parameters rather than fixed input values.

The polar mass moment of inertia associated with the rotational motion is not reported explicitly in the paper. In the present model, it has therefore been estimated by matching the natural frequencies and instability behaviour described in the experiments. On this basis, a constant value of $I_\theta = 1.0 \times 10^{-4}\ \mathrm{kg\,m^2}$ is adopted for all simulations.

3.4. Model verification: free-decay check

Two representative operating conditions from the experiment are reproduced numerically in order to assess the capability of the 3DOF model to capture the coupled motion of the iced conductor.

3.4.1. Case 1

The first case corresponds to a wind speed of $U = 12\ \mathrm{m/s}$ and an initial pitch angle of $\theta_0 = -165°$, within the instability range associated with the tail of the ice accretion. The stiffnesses are chosen such that the uncoupled natural frequencies in the horizontal, vertical and rotational directions are close to those reported in the experiment, and the ratio between the vertical and rotational frequencies is nearly unity. In the physical set-up both translational directions are pretensioned, which shifts the static equilibrium position to approximately $0.10\ \mathrm{m}$. In the present model, displacements are measured relative to this equilibrium position, so the mean of the computed signals is close to zero. The corresponding structural and flow parameters for Case 1 are summarised in Table 3.2.

Wind speed U	$12\ \mathrm{m/s}$
Initial pitch angle θ_0	$-165°$
Horizontal natural frequency f_x	$0.995\ \mathrm{Hz}$
Vertical natural frequency f_y	$0.845\ \mathrm{Hz}$
Rotational natural frequency f_θ	$0.865\ \mathrm{Hz}$
Frequency ratio f_y/f_θ	0.98

Table 3.2: Parameters used for Case 1 of the benchmark simulations. [7]

Figure 3.5 compares the simulated vertical displacement with the experimental time history and x–y trajectory reported in the original paper. The numerical solution exhibits a quasi-periodic response with a nearly constant amplitude during the simulation, indicating that the system has reached a stable limit cycle. The amplitude level, frequency and slight modulation of the envelope are in good agreement with the measurements, and the simulated x–y orbit has the same elongated, inclined shape as the experimental trajectory. This confirms that the model correctly reproduces the phase relationship and relative motions.

The rotational response for Case 1 shows similar behaviour. The pitch angle oscillates around its mean value with a peak-to-peak amplitude of approximately $13°$, which is consistent with the amplitude reported in the paper for this operating point. The rotation is almost perfectly synchronised with the translational motion, reflecting the near 1:1 ratio between the vertical and rotational natural frequencies. Overall, the comparison indicates that the chosen set of structural parameters and aerodynamic coefficients is capable of reproducing the key features of the measured coupled motion at $U = 12\ \mathrm{m/s}$, including the existence of a steady galloping limit cycle, its oscillation frequency and its characteristic spatial orbit.

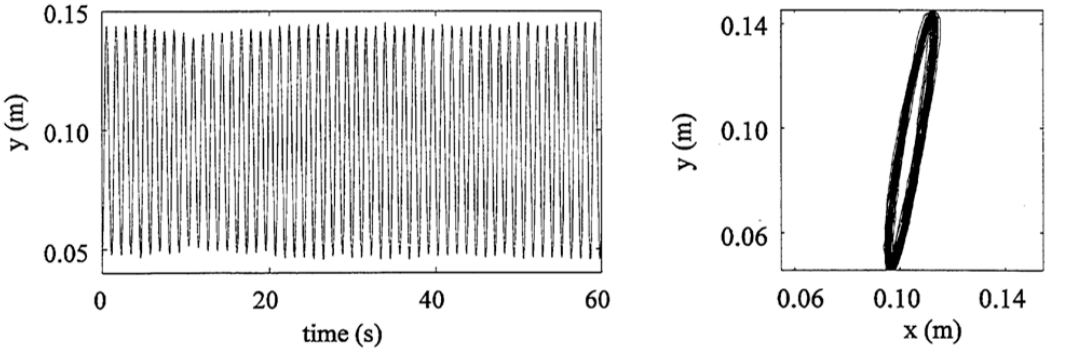

(a) Results paper [7]

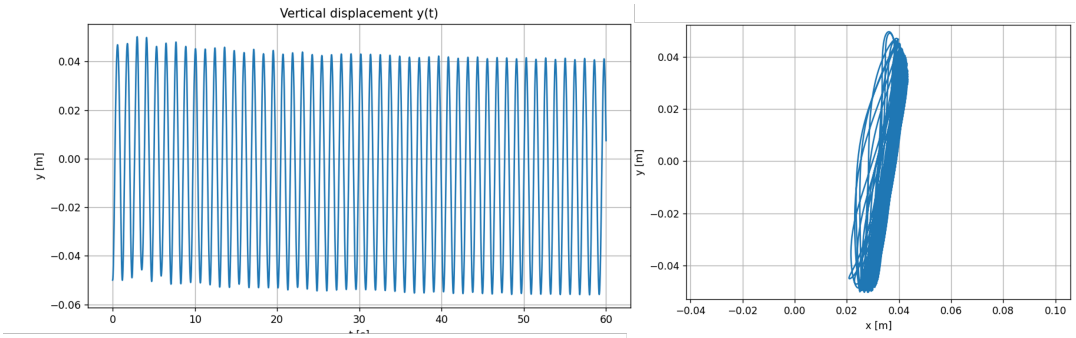

(b) Results reproduction model

Figure 3.5: Results for benchmark Case 1.

3.4.2. Case 2

The second case corresponds to a lower wind speed of $U = 8.5\ \mathrm{m/s}$ and an initial pitch angle of $\theta_0 = -180°$, which lies close to the second unstable region identified by the Den–Hartog criterion. The natural frequencies of the uncoupled system are selected to match the experimental configuration, with vertical, horizontal, and rotational frequencies of 0.85, 0.96 and $1.54\ \mathrm{Hz}$, respectively. This gives a ratio between the vertical and rotational frequencies of $f_v/f_\theta = 0.55$. As in the physical set-up, the translational directions are pre-tensioned such that the static equilibrium position is displaced to approximately $0.10\ \mathrm{m}$. In the present model this offset is removed, and the reported displacements are measured relative to the equilibrium position. The parameters used for Case 2 are summarised in Table 3.3.

Wind speed U	$8.5\ \mathrm{m/s}$
Initial pitch angle θ_0	$-180°$
Horizontal natural frequency f_x	$0.96\ \mathrm{Hz}$
Vertical natural frequency f_v	$0.85\ \mathrm{Hz}$
Rotational natural frequency f_θ	$1.54\ \mathrm{Hz}$
Frequency ratio f_v/f_θ	0.55

Table 3.3: Parameters used for Case 2 of the benchmark simulations. [7]

Figure 3.6 compares the computed vertical displacement and x–y trajectory with the experimental time histories for the same operating point. The vertical response shows a gradual growth of the oscillation amplitude over the $50\ \mathrm{s}$ simulation window. This behaviour is consistent with the experimental record, where the oscillation builds up from the initial perturbation and continues to grow beyond the $50\ \mathrm{s}$ shown in the figure. In the experiment, the maximum vertical displacement reaches about $0.20\ \mathrm{m}$ later in the run, which were the limits of the physical model. This level is also attained in the numerical simulations, for approximately the same time.

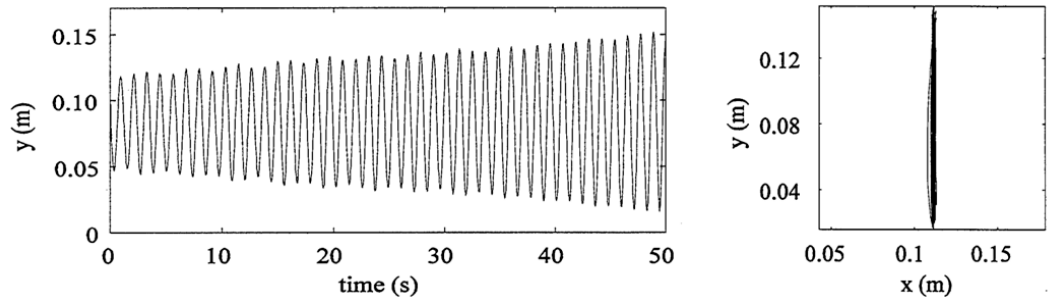

(a) Results paper [7]

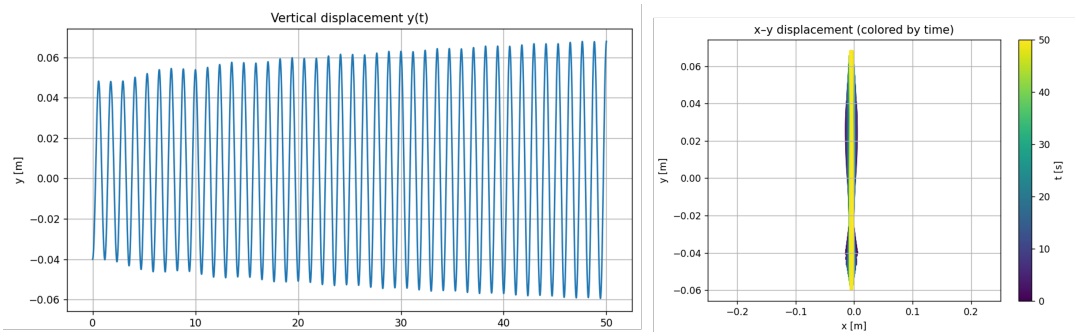

(b) Results reproduction model

Figure 3.6: Results for benchmark Case 2.

The simulated x–y orbit is a slender loop, which is qualitatively in good agreement with the measured trajectory. The shape and orientation of the orbit reflect a stronger vertical than horizontal response, combined with the relatively high torsional frequency. The rotational motion remains modest compared to Case 1. The simulated pitch angle exhibits a peak-to-peak amplitude of approximately 3°, in line with the value reported in the paper for this case. This confirms that, for the chosen combination of stiffnesses and frequency ratio $f_v/f_\theta = 0.55$, the model reproduces the experimentally observed regime of predominantly vertical galloping with weakly coupled rotation. Overall, Case 2 demonstrates that the 3DOF model is able not only to capture large-amplitude coupled motion (Case 1), but also to reproduce a regime with smaller rotational amplitudes and slower growth of the vertical response, as observed experimentally when the vertical and rotational natural frequencies are more widely separated.

3.5. Benchmark model summary

The benchmark model based on the iced transmission-line experiment provides a consistent basis for the subsequent cross-sectional analysis of the present configuration. The Fourier representation of the aerodynamic coefficients reproduces the Den–Hartog instability ranges reported in the original study, and the free–decay simulations confirm that the structural mass, stiffness and damping are implemented correctly. In addition, the time-domain simulations for two representative operating conditions yield vertical displacements, x–y orbits and pitch amplitudes that are in close agreement with the experimental records. A key outcome of the benchmark is that the presence of torsional freedom influences the effective stability and response characteristics compared with a purely 1DOF Den–Hartog screening. This can be explained by the effective dynamic angle of attack. Torsional motion can modify the instantaneous operating angle and introduce additional aeroelastic coupling through the moment coefficient, which may shift the instability boundary relative to the 1DOF indicator [19–21]. Despite the simplifying assumptions of the lumped-parameter three-degree-of-freedom model, the agreement with the measurements is good. The model uses quasi-steady aerodynamics and an estimated polar moment of inertia. Even so, the simulations reproduce the main features of coupled translational–rotational galloping. They also capture the influence of torsion and frequency tuning on the response [19, 20, 22]. The numerical framework and parameter identification are therefore considered sufficiently validated. They are adopted, with slight modifications, for the cross-sectional analysis of the project-specific cross-sections in Chapter 4.

4

Case-study cross-sections

This chapter applies the numerical framework, which has been verified in Chapter 3, to the case-study cross-sections considered in this thesis; 18A and 32A. The 3DOF cross-sectional model is evaluated for the full range of inflow directions and three added-mass assumptions. The focus of this chapter lies on identifying orientations that lead to sustained oscillations. Also the sensitivity of the response is evaluated with multiple sensitivity studies. For readability, the detailed results for the 32A cross-section are provided in Appendix A. A direct comparison between the considered cross-sections is presented at the end of this chapter.

4.1. Configuration and coefficient curves

Both systems are modeled as rigid 2D 3DOF cross-sections. The degrees of freedom are in-line translation $x(t)$, cross-flow translation $y(t)$, and rotation $\theta(t)$ about the out-of-plane axis. The structural restoring forces are represented by linear springs and viscous dampers. The surrounding flow is assumed to be steady and uniform with inflow velocity (U_∞) and inflow direction (ψ). The properties in the models are computed from the specified geometry and material densities for the solid and internal fluid. The fluid density is taken as $\rho = 1025\ \mathrm{kg/m^3}$. This Chapter will clarify the configuration for the 18A model.

Model 18A consists of three in-line pipes. A schematic lay-out of the 18A model is shown in Figure 4.1.

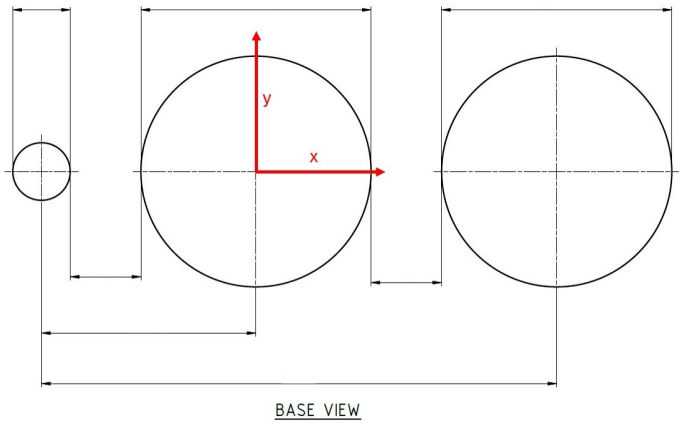

Figure 4.1: Layout of the 18A model geometry

Hydrodynamic loads are evaluated using a quasi-steady representation with fitted force and moment coefficient functions of the instantaneous effective angle of attack. These coefficients are obtained with the Fourier fit given in Equation 3.1, based on the data obtained from a MARIN report. A visual overview can be found in Figure 4.2. The Fourier representation is kept to a limited order, such that the coefficient functions remain smooth and physically realistic and do not introduce artificial oscillations associated with high-order curve fitting.

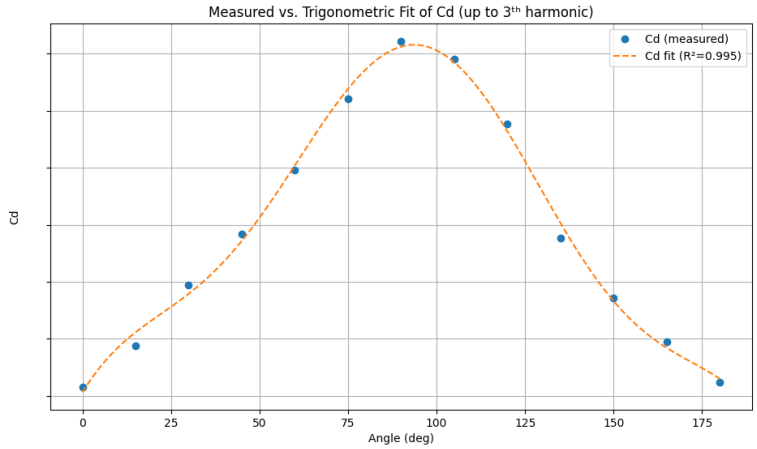

(a) $C_d(\alpha)$ curve fit

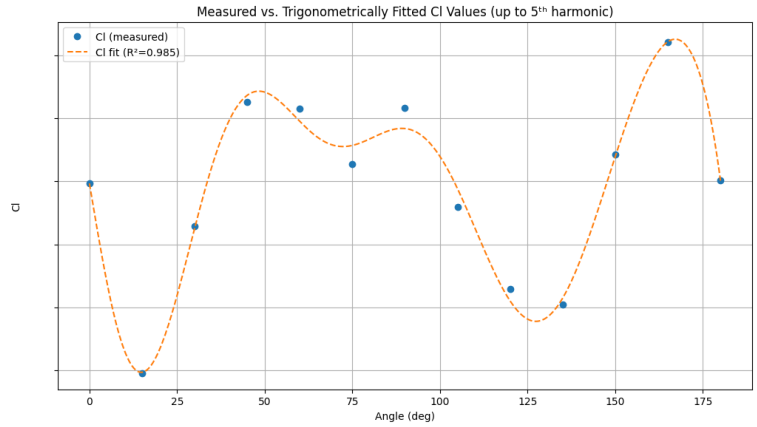

(b) $C_l(\alpha)$ curve fit

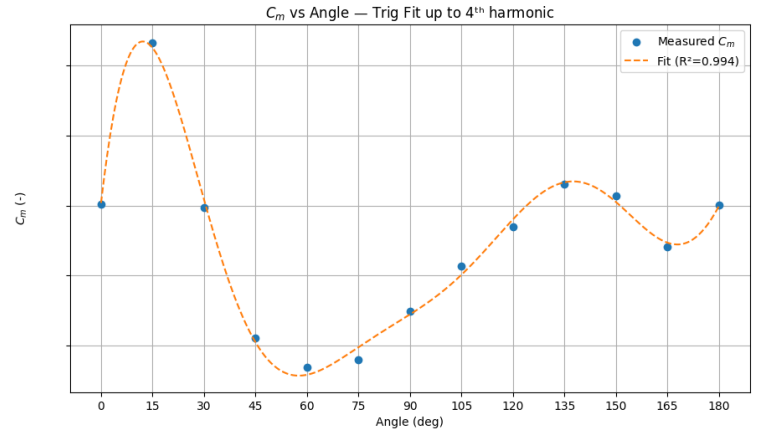

(c) $C_m(\alpha)$ curve fit

Figure 4.2: Results for Fourier curve-fitting - Model 18A

4.2. Governing equations

The equations of motion follow the 3DOF formulation introduced in Chapter 2. Recalling the main formulas in this chapter, starting with the EOM:

$$(m + m_{a,x})\,\ddot{x} + c_x\dot{x} + k_x x = F_x(\alpha) \tag{4.1}$$

$$(m + m_{a,y})\,\ddot{y} + c_y\dot{y} + k_y y = F_y(\alpha) \tag{4.2}$$

$$(I_z + I_{z,a})\ddot{\theta} + c_\theta\dot{\theta} + k_\theta\theta = T(\alpha) \tag{4.3}$$

where m and I_z are the structural mass and polar mass moment of inertia of the cross-sectional slice, $m_{a,x}$ and $m_{a,y}$ are translational added-mass terms, $I_{z,a}$ is the rotational added mass term, and $k_{x,y,\theta}$ and $c_{x,y,\theta}$ are the stiffness and damping coefficients. In this thesis, the rotational added-inertia term is neglected by setting $I_{z,a} = 0$ for simplicity. This choice is made because reliable values for rotational added inertia are generally difficult to obtain for non-circular composite cross-sections and would introduce additional uncertainty. Neglecting $I_{z,a}$ provides a practical first-order model while keeping the number of uncertain hydrodynamic parameters limited.

4.2.1. Relative velocity and effective angle of attack

The inflow velocity vector is defined as:

$$\mathbf{U}_\infty = U_\infty \begin{bmatrix} \cos\psi \\ \sin\psi \end{bmatrix} \tag{4.4}$$

and the relative velocity seen by the moving section is:

$$\mathbf{U}_{\mathrm{rel}} = \mathbf{U}_\infty - \begin{bmatrix} \dot{x} \\ \dot{y} \end{bmatrix} = \begin{bmatrix} U_x \\ U_y \end{bmatrix} \tag{4.5}$$

where $U_x = U_\infty \cos\psi - \dot{x}$ and $U_y = U_\infty \sin\psi - \dot{y}$. The body-axis unit vector is given by:

$$\mathbf{b}_\parallel = \begin{bmatrix} b_x \\ b_y \end{bmatrix} = \begin{bmatrix} \cos\theta \\ \sin\theta \end{bmatrix} \tag{4.6}$$

The instantaneous effective angle of attack is computed as the signed angle between $\mathbf{b}_\parallel$ and $\mathbf{U}_{\mathrm{rel}}$:

$$\alpha \;=\; \arctan\!\left(\frac{b_x U_y - b_y U_x}{b_x U_x + b_y U_y}\right) \tag{4.7}$$

4.2.2. Hydrodynamic forces and moment

Let $u = \|\mathbf{U}_{\mathrm{rel}}\|$ and define the unit vectors along and normal to the relative flow direction as:

$$\mathbf{e}_{\parallel} = \frac{\mathbf{U}_{\mathrm{rel}}}{u}, \qquad \mathbf{e}_{\perp} = \begin{bmatrix} -e_{\parallel,y} \\ e_{\parallel,x} \end{bmatrix} \tag{4.8}$$

Using the reference diameter D_{ref}, taken as the main-pipe diameter, and the height of the cross-section H, so that the projected reference area is $A_{\mathrm{ref}} = D_{\mathrm{ref}}H$. The quasi-steady force vector can be written as:

$$\mathbf{F}(\alpha) = \frac{1}{2}\rho u^2 A_{\mathrm{ref}} \left[C_D(\alpha)\, \mathbf{e}_{\parallel} + C_L(\alpha)\, \mathbf{e}_{\perp} \right], \qquad \mathbf{F} = \begin{bmatrix} F_x \\ F_y \end{bmatrix} \tag{4.9}$$

The torsional load is modeled using the fitted moment coefficient $C_m(\alpha)$. The torsional load about the center of the middle cylinder can be written as:

$$T(\alpha) = \frac{1}{2}\rho u^2 D_{\mathrm{ref}}^2 H\, C_m(\alpha) \tag{4.10}$$

4.3. Galloping indicator

The hydrodynamic coefficients are represented by smooth Fourier-series fits based on the available MARIN dataset for the case-study cross-sections (Section 4.1). This continuous representation is used both to evaluate the quasi-steady loads during time integration and to assess the susceptibility to galloping as a function of inflow orientation.

Potential galloping-prone orientations are identified using the Den Hartog onset indicator. As described in Chapter 2, galloping may occur when the fluid loading introduces negative effective damping. In terms of steady coefficients, this is assessed through:

$$\frac{\mathrm{d}C_L}{\mathrm{d}\alpha} + C_D \leq 0 \tag{4.11}$$

where α denotes the inflow angle used to parameterize the coefficient data. The derivative $\mathrm{d}C_L/\mathrm{d}\alpha$ is obtained analytically from the fitted coefficient curves to ensure a smooth and consistent evaluation across all angles. It is noted that this indicator is derived for 1DOF transverse motion with a fixed section orientation. In the present 3DOF model, torsion makes the effective angle of attack $\alpha(t)$ dynamic through $\theta(t)$, which can either amplify or suppress the response via translation–rotation coupling and the moment coefficient. Therefore, the Den Hartog indicator is used here as a screening tool to identify susceptible orientations, while the final stability assessment is performed using the coupled time-domain simulations.

The cross-section is symmetric about the x-axis, such that the coefficient behaviour repeats over half a revolution. Therefore, the Den Hartog indicator is evaluated over $\alpha \in [0°,\, 180°]$, which fully captures the stability behaviour of the section. Figure 4.3 shows $C_D(\alpha)$, $\mathrm{d}C_L/\mathrm{d}\alpha$, and their sum $H(\alpha) = \mathrm{d}C_L/\mathrm{d}\alpha + C_D$. The zero-crossings of $H(\alpha)$ indicate transitions between stable and potentially unstable regions and are found at:

$$\alpha = 13.58°,\ 105.40°,\ 117.79°,\ 168.59° \tag{4.12}$$

Based on these crossings and Figure 4.3, three angular zones with $H(\alpha) \leq 0$ are defined as:

$$\begin{aligned} &\text{Zone 1: } 0° \leq \alpha \leq 13.58° \\ &\text{Zone 2: } 105.40° \leq \alpha \leq 117.79° \\ &\text{Zone 3: } 168.59° \leq \alpha \leq 180° \end{aligned} \tag{4.13}$$

These zones indicate inflow orientations that are most susceptible to galloping. They are therefore used to guide the selection of cases, and are examined in more detail in Chapter 4.6.

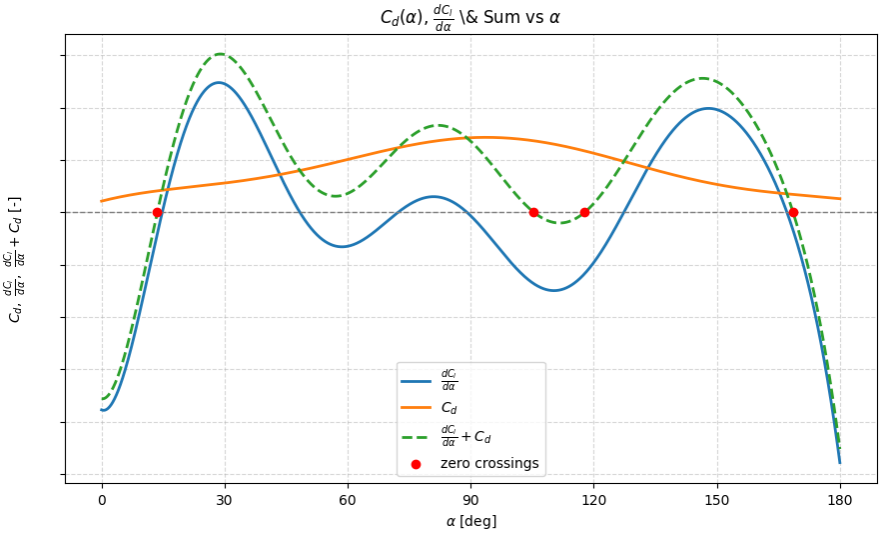

Figure 4.3: Den Hartog Criteria Model 18A

4.4. Input data for simulations

This section summarises the input parameters used in the numerical simulations for the case-study cross-sections. All simulations use the same cross-sectional 3DOF model defined in Section 4.2 and the same quasi-steady coefficient set introduced in Section 4.1. The study covers a systematic sweep over inflow direction (ψ) at a fixed free-stream speed U_∞. To quantify the influence of hydrodynamic inertia, three added-mass scenarios are compared. Apart from the added-mass treatment, all model settings are kept identical.

4.4.1. Added-mass scenarios

Hydrodynamic inertia is included through translational added mass in the in-line and cross-flow directions. Three added-mass scenarios are considered: (i) no added mass ($C_a = 0$), (ii) constant added mass ($C_a = 1$), and (iii) frequency-dependent added mass using the $C_a(f^*)$ relation described in Section 2.2.4. Rotational added inertia is neglected in all cases by setting $I_{z,a} = 0$.

Baseline added-mass terms are obtained from the equivalent-ellipse approximation of the three-pipe cross-section (Section 2.2.3), resulting in direction-dependent translational added-mass contributions. These terms modify the effective masses, and therefore influence the natural frequencies and (through Equation 4.16) the effective damping level used in the time-domain simulations.

4.4.2. Geometric, material and fluid inputs

A cross-sectional slice model of length $L = 1\ \mathrm{m}$ is used for mass and inertia evaluation, which difference for both of the cross-sections. The fluid is water with density $\rho = 1025\ \mathrm{kg/m^3}$. The structural mass and polar moment of inertia are computed from the geometry and the material densities of the solid and internal fluid in the section model.

4.4.3. Structural parameters and damping definition

The linear stiffness and damping parameters are set identical in the in-line and cross-flow directions:

$$k_x = k_y = 560\ \mathrm{N/m}, \qquad k_\theta = 850\ \mathrm{N\,m/rad} \tag{4.14}$$

The linear stiffness values are selected by scaling the linear model to the expected frequency range of the full-scale riser. First, the natural frequencies are estimated with the taut-string approximation given by:

$$f_n = \frac{n}{2L}\sqrt{\frac{T_{\text{eff}}}{m_{\text{eff}}}} \tag{4.15}$$

This gives a fundamental frequency f_1 for the riser of $4\,\text{km}$ of $0.0062\,\text{Hz}$. As an external check, Deng et al. report dominant response frequencies around 0.06, 0.111 and $0.233\,\text{Hz}$ for a riser of $5.5\,\text{km}$. These correspond to the 14th, 24th and 48th modes, respectively [28]. This confirms that the first natural frequency of the riser taut-string approximation is of the same order as the first natural frequency of the paper. The stiffness level is selected so that the lumped model represents a relevant higher-mode frequency. The 48th-mode level is used because it is reported as particularly responsive in the reference spectrum [28]. Based on this comparison, the translational stiffnesses are chosen as $k_x = k_y = 560\ \text{N/m}$, which correspond with a natural frequency of approximately $0.2\,\text{Hz}$. Finally, $k_\theta = 850\ \text{N m/rad}$ is selected to keep the torsional natural frequency in the same order of magnitude, so that translation–torsion coupling can develop when the modes are closely tuned.

Damping is specified through target damping ratios ζ_{xy} and ζ_θ in water. Literature values for long, slender cylinders and deepwater risers are often a few tenths of a percent. For example, Kim et al. [29] use a damping ratio of about 0.3% (at the dominant cross-flow frequency) in a deepwater riser time-domain VIV model, while Vandiver et al. [30] report values around 0.5% on average, with test cases spanning roughly 0.3% to 0.9% depending on the configuration and mode. In the present work, a higher baseline value is adopted ($\zeta_{xy} = 0.01$ and $\zeta_\theta = 0.01$). This choice is intentionally conservative with respect to stability predictions: it reduces the risk of over-predicting galloping onset when the true damping level is uncertain and when additional dissipative mechanisms are not modelled explicitly in the quasi-steady framework.

The viscous damping coefficients are defined from the damping ratios ζ_{xy} and ζ_θ using the effective masses $m_{\text{eff},x}$ and $m_{\text{eff},y}$:

$$c_x = 2\zeta_{xy}\sqrt{k_x\, m_{\text{eff},x}}, \qquad c_y = 2\zeta_{xy}\sqrt{k_y\, m_{\text{eff},y}}, \qquad c_\theta = 2\zeta_\theta\sqrt{k_\theta I_z} \tag{4.16}$$

In the numerical implementation, the damping ratios ζ_{xy} and ζ_θ are kept constant, while c_x and c_y are updated during time integration when $m_{\text{eff},x}$ and $m_{\text{eff},y}$ change.

4.4.4. Flow conditions and simulation sweep

The free-stream speed is fixed at $U_\infty = 0.45\ \text{m/s}$. A full inflow-direction sweep is performed over $\psi \in [0°, 180°]$. This covers all unique orientations due to the symmetry of the cross-section. The results of this full sweep are used as a first screening. Subsequently, the analysis focuses on the angular zones identified from the Den Hartog indicator in Section 4.3, since these zones are most susceptible to galloping-type instability.

4.4.5. Time integration settings and response metric

The coupled nonlinear equations are integrated in time using an implicit stiff Radau solver. Each simulation is run from $t = 0$ to $t = T_{\text{end}} = 400\ \text{s}$ with $\Delta t = 0.2\text{s}$. To quantify the post-transient response level, the response amplitude is estimated from the final time window of length $T_w = 40\ \text{s}$. The reported amplitude is computed as:

$$A_{\text{end}} = \frac{1}{2}\sqrt{(\Delta x)^2 + (\Delta y)^2}, \qquad \Delta x = x_{\max} - x_{\min}, \quad \Delta y = y_{\max} - y_{\min} \tag{4.17}$$

evaluated over $t \in [T_{\text{end}} - T_w,\ T_{\text{end}}]$.

4.5. Sensitivity study on Model 18A

This section presents the parameter sensitivity study on the 18A model to verify that the coupled 3DOF time-domain model behaves consistently with physical expectations. The objective is to confirm that the model responds correct when key structural and flow parameters are perturbed, and to identify which parameters have the strongest influence on the amplitude response level. The sensitivity metric used throughout is the end-window resultant amplitude A_{end} (Eq. 4.17), evaluated over the final part of each simulation. Three one-at-a-time sweeps are performed. First, the translational stiffnesses are varied by scaling k_x and k_y simultaneously. Second, the rotational stiffness k_θ is varied to assess the role of torsional restoring on the coupled dynamics. Finally, the inflow speed U_∞ is varied to quantify how changes in the flow velocity modify the onset and amplitude of galloping-type oscillations.

4.5.1. Varying k_x and k_y

A one-at-a-time sensitivity sweep was carried out in which the translational stiffnesses were scaled simultaneously ($k_x = k_y = s\,k_0$), while all other inputs were kept fixed. The damping ratio was kept fixed. Consequently, the viscous damping coefficients varied with stiffness according to Equation 4.16. For each stiffness scale factor s, the response level was quantified using the end-window resultant amplitude A_{end}. The corresponding results for the three Den Hartog screening zones are shown in Figures 4.4–4.6. Across all three angular bands, the location of the response windows in ψ remains nearly unchanged when varying k_x and k_y. This is consistent with the model structure. The existence and angular extent of the unstable regions are mainly governed by the Den Hartog indicator, whereas the stiffness level primarily controls the post-onset amplitude through its influence on the wet natural frequencies.

Zone 1 (Fig. 4.4). The response is largest at small inflow angles and collapses to zero near $\psi \approx 16°$–$17°$. The collapse angle is almost unaffected by stiffness scaling, while the plateau amplitude varies with s. An unexpected effect happens for $s = 0.25$ and $s = 0.4$, where the amplitude decreases quicker then compared to other zones. At low stiffness, the larger relative velocities modify the instantaneous angle of attack. With this modification the drag and lift coefficient can become smaller which leads to lower amplitudes. For the lowest stiffness case ($s = 0.1$), no sustained response is observed. This happens because the strong reduction in translational stiffness shifts the wet natural frequencies and detunes the coupled translation–rotation dynamics that drive the negative-damping mechanism. In combination with the frequency-dependent added-mass, this can move the system into a stable regime.

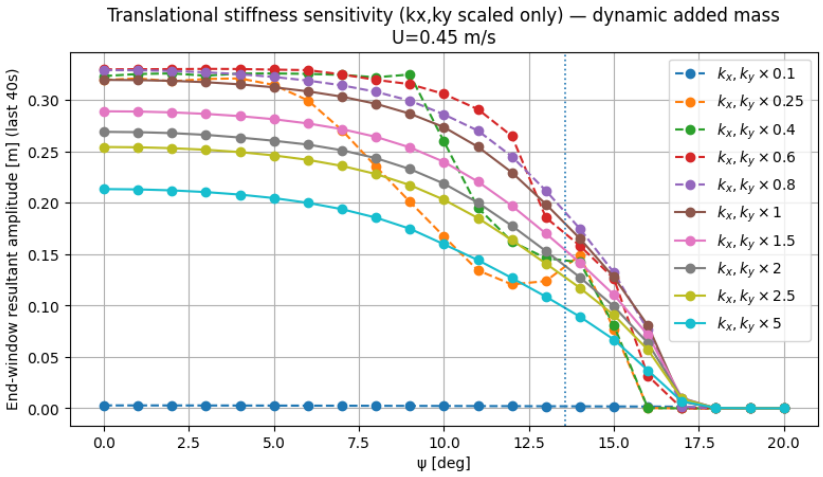

Figure 4.4: Sensitivity to translational stiffness scaling ($k_x = k_y = s\,k_0$) in Zone 1.

Zone 2 (Fig. 4.5). The response appears as a narrow, symmetric bump within the Den Hartog interval. A clear maximum is found around $\psi \approx 112°$–$113°$ and amplitudes decaying back to zero towards the interval boundaries. As k_x and k_y are reduced, the peak amplitude increases markedly, while the angular location and width of the bump remain essentially unchanged. This indicates that the unstable window is determined by the coefficients, whereas the post-onset response level is strongly controlled by the translational stiffness.

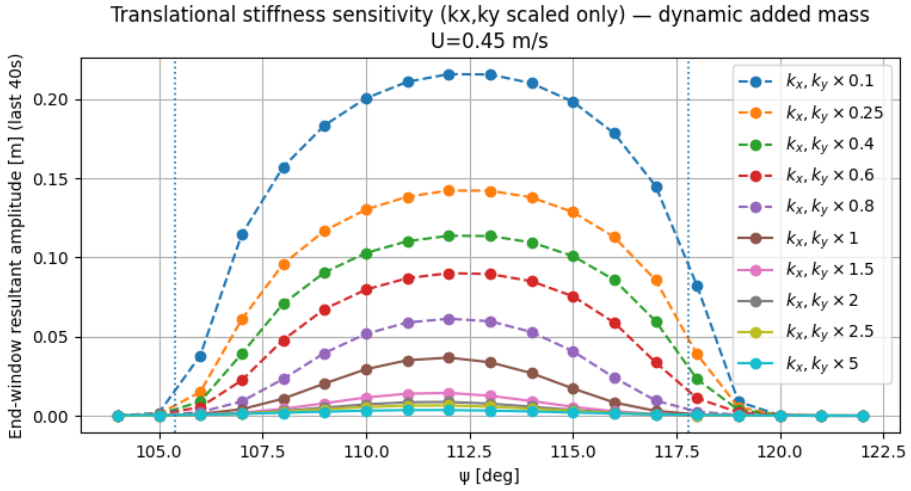

Figure 4.5: Sensitivity to translational stiffness scaling ($k_x = k_y = s\,k_0$) in Zone 2.

Zone 3 (Fig. 4.6). A sharp onset occurs very close to $\psi \approx 168°$, after which the amplitude rapidly rises to a plateau that persists up to $\psi = 180°$. The onset angle is almost insensitive to stiffness scaling, except for $s = 0.1$, but the plateau level is not. A lower translational stiffness produces substantially larger amplitudes, while increasing stiffness reduces the plateau. The sudden increase at onset and the nearly constant amplitude up to $\psi = 180°$ indicate that this zone is a strong and persistent instability region. In this case, changing the stiffness mainly affects how large the final oscillations become, rather than whether the instability occurs at all.

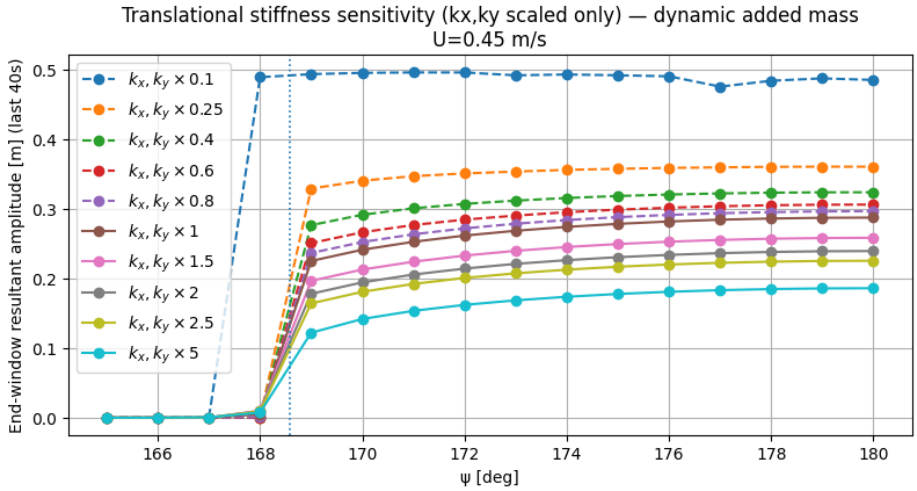

Figure 4.6: Sensitivity to translational stiffness scaling ($k_x = k_y = s\,k_0$) in Zone 3.

4.5.2. Varying k_θ

A one-at-a-time sensitivity sweep was carried out in which only the rotational stiffness was scaled ($k_\theta = s\,k_{\theta,0}$), while the translational stiffnesses k_x and k_y and all remaining inputs were kept at their baseline values. The response level was quantified using the end-window resultant amplitude A_{end} for simulations at $U_\infty = 0.45$ m/s. The results for the three Den Hartog screening zones are shown in Figs. 4.7–4.9.

Changing k_θ modifies the resistance against rotation and therefore the degree to which the section is able to reorient under hydrodynamic loading. Increasing k_θ restricts rotational motion, which reduces the variation of $\alpha(t)$ caused by $\theta(t)$ and makes the system behave more like a purely translational model. In the limit of very large k_θ, rotation becomes negligible and the rotational DOF contributes less to the coupled response. Conversely, reducing k_θ increases rotational compliance, which can either amplify the coupled response or stabilise it.

Zone 1 (Fig. 4.7). For moderate and high k_θ ($s \geq 0.6$), the response starts at a high plateau and then collapses to near zero within the same angular band as the baseline case. The collapse angle shifts by a few degrees with k_θ, with stiffer rotation causing an earlier drop-off. For low torsional stiffness the response is strongly reduced. For $s = 0.1, 0.25$ the amplitudes remain near zero throughout the zone. This indicates that allowing the section to rotate more freely can mitigate the effective negative-damping mechanism in this interval.

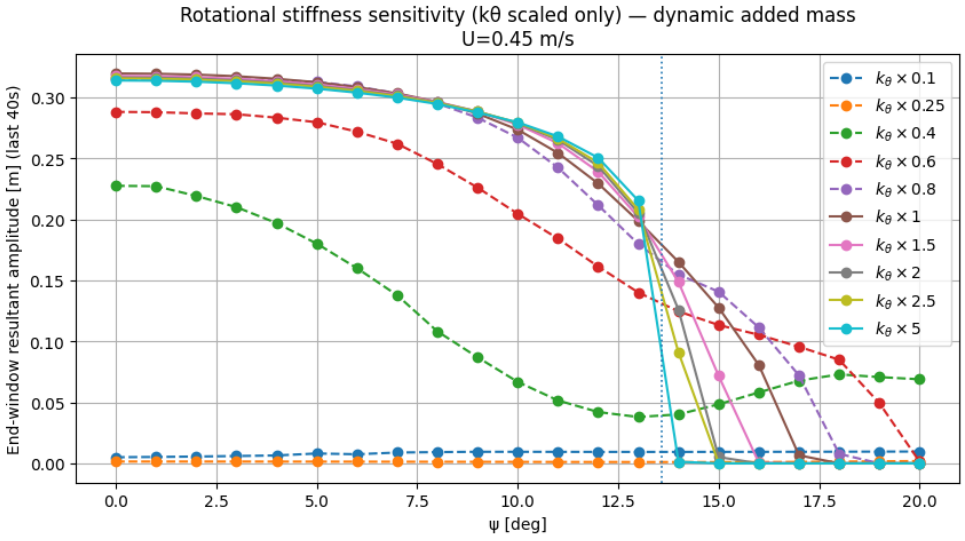

Figure 4.7: Sensitivity to rotational stiffness scaling ($k_\theta = s\,k_{\theta,0}$; k_x, k_y fixed) in Zone 1.

Zone 2 (Fig. 4.8). The response remains a small-amplitude bump centered near $\psi \approx 112°$, but the peak magnitude is highly sensitive to k_θ. For low rotational stiffness the response is almost fully suppressed, whereas increasing k_θ produces a progressively larger peak, with the stiffest cases giving the highest amplitudes. The onset and decay angles remain almost unchanged, which suggests that k_θ mainly affects the strength of the coupled response rather than shifting the angular interval where the quasi-steady forcing is destabilising.

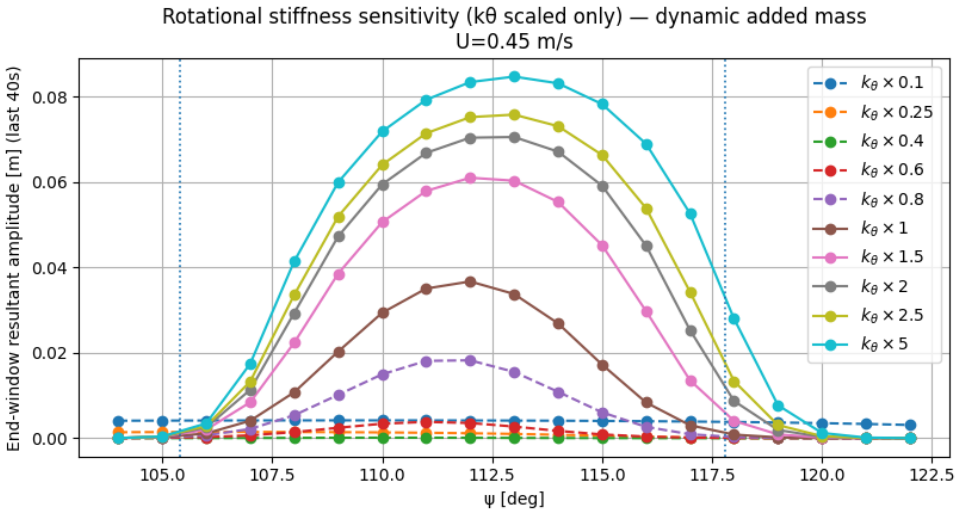

Figure 4.8: Sensitivity to rotational stiffness scaling ($k_\theta = s\,k_{\theta,0}$; k_x, k_y fixed) in Zone 2.

Zone 3 (Fig. 4.9). The response shows a distinct onset near $\psi \approx 168°$–$169°$ for most stiffness factors, followed by rapid growth and saturation towards the end of the interval. Once the oscillation is established, the plateau amplitude is the same for al values above $s = 0.4$. Extremely low rotational stiffness can completely eliminate the response ($s = 0.1$) or produce a more gradual build-up and a slightly reduced plateau ($s = 0.25$). Overall, this indicates that torsional stiffness mainly influences whether the instability can develop near onset in Zone 3, while the saturated translational response level is relatively insensitive to k_θ once the coupled response is established.

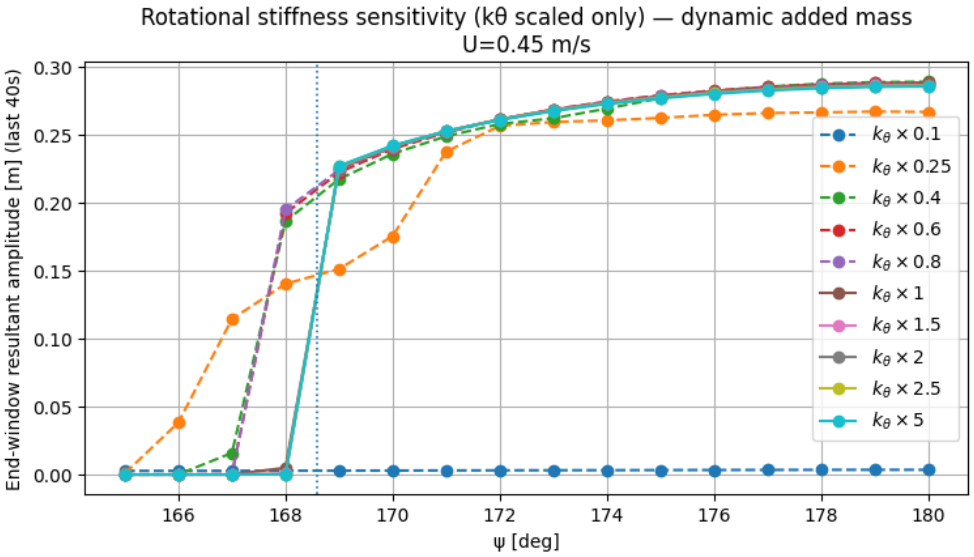

Figure 4.9: Sensitivity to rotational stiffness scaling ($k_\theta = s\,k_{\theta,0}$; k_x, k_y fixed) in Zone 3.

4.5.3. Varying inflow velocity

A one-at-a-time sensitivity sweep was carried out in which the inflow velocity was varied, while all structural parameters and remaining inputs were kept at their baseline values. The response level was quantified using the end-window resultant amplitude A_{end} for each velocity level. The results for the three identified Den Hartog zones are shown in Figs. 4.10–4.12.

Changing U_∞ directly modifies the hydrodynamic forcing level and the effective reduced velocity. In general, increasing U_∞ strengthens the negative-damping mechanism and promotes larger post-onset oscillations, although the coupled 3DOF dynamics can lead to non-monotonic behaviour in marginal zones where small changes in response frequency and effective angle of attack can shift the operating point.

Zone 1 (Fig. 4.10). The response level increases with U_∞ over the low-to-moderate range, producing progressively larger plateau amplitudes at small inflow angles. The decay towards zero still occurs within a similar angular band, but the collapse is shifted to slightly higher ψ for intermediate velocities. At the highest velocities the response can be partially suppressed, indicating that the coupled dynamics can stabilise the motion once the system moves into a different effective reduced-frequency regime.

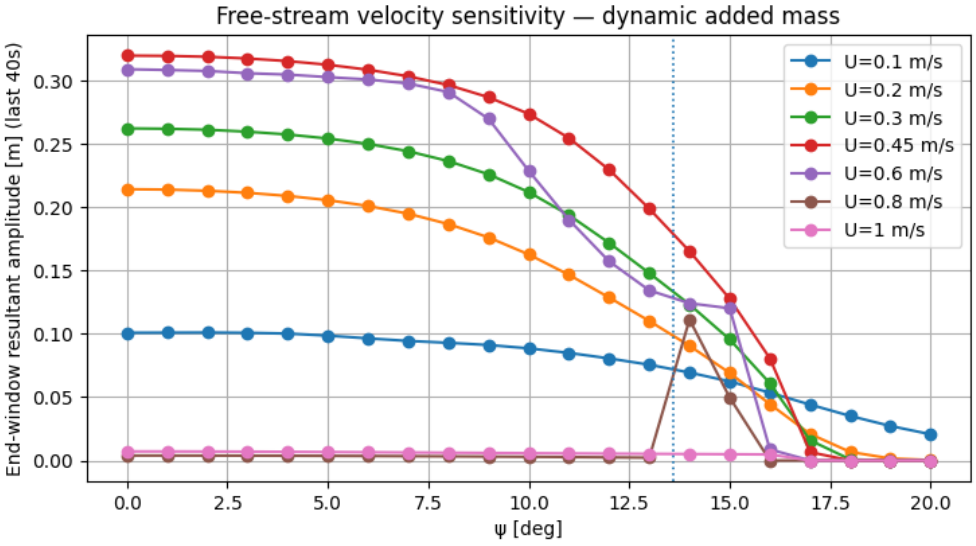

Figure 4.10: Sensitivity to inflow velocity U_∞ (all stiffness parameters fixed) in Zone 1.

Zone 2 (Fig. 4.11). Zone 2 remains a small-amplitude bump centred near $\psi \approx 112°$, but its magnitude is highly velocity dependent. For low U_∞ the response is weak, while increasing U_∞ produces a larger peak within the same onset angles. This behaviour is consistent with Zone 2 being a marginal instability. The angular extent is set primarily by the quasi-steady coefficient behaviour, whereas the amplitude scales strongly with the flow speed once the limit cycle is triggered.

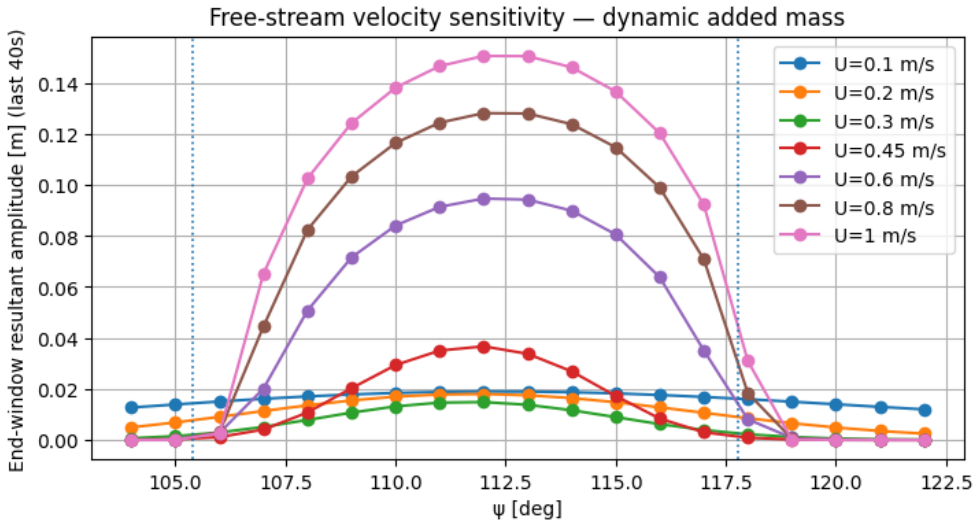

Figure 4.11: Sensitivity to inflow velocity U_∞ (all stiffness parameters fixed) in Zone 2.

Zone 3 (Fig. 4.12). A distinct onset occurs near $\psi \approx 168°$, after which the response grows rapidly and approaches a plateau towards $\psi = 180°$. The plateau amplitude increases strongly with U_∞, confirming that this zone corresponds to an instability where the post-onset limit-cycle level is primarily controlled by the flow speed. The onset angle itself changes only weakly with U_∞, which indicates that the directional localisation of the unstable window remains governed mainly by the quasi-steady coefficient behaviour.

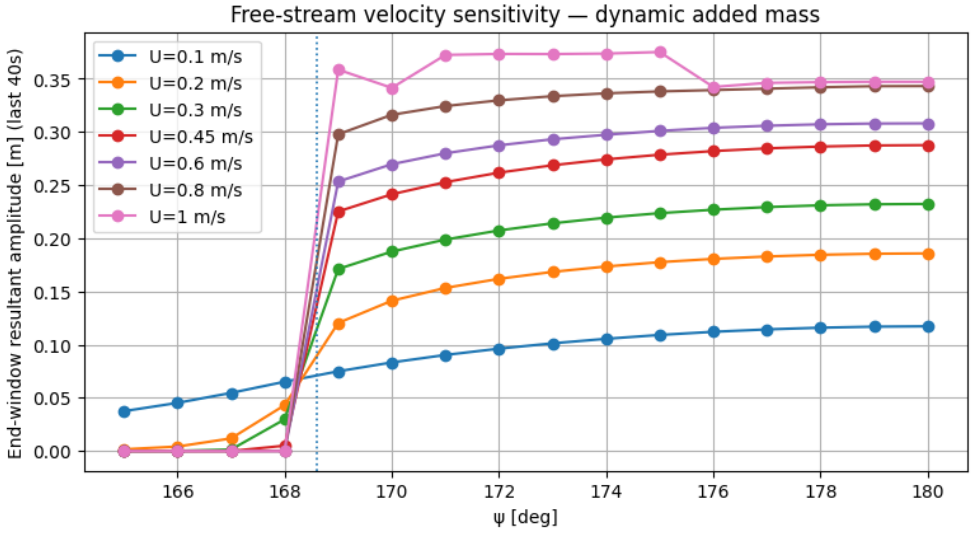

Figure 4.12: Sensitivity to inflow velocity U_∞ (all stiffness parameters fixed) in Zone 3.

4.5.4. Conclusion of the sensitivity study

The one-at-a-time sensitivity sweeps show that the coupled 3DOF time-domain model responds consistently to changes in key structural and flow parameters. In all cases the response remains strongly direction-dependent and the same three response-active windows persist, which indicates that the angular localisation of the instability is primarily governed by the quasi-steady coefficients. In contrast, the magnitude of the established response within these windows is clearly parameter dependent.

Scaling the translational stiffnesses (k_x and k_y) mainly affects the post-onset amplitude through changes in the wet natural frequencies, while the onset and decay angles remain nearly unchanged. Very low translational stiffness ($s = 0.1$) can eliminate the response in parts of the range, which is attributed to detuning of the coupled translation–rotation dynamics in combination with the frequency-dependent added-mass treatment. Varying the rotational stiffness k_θ alters the degree of rotation and therefore the translation–rotation coupling through $\alpha(t)$. Increasing k_θ restricts rotation and makes the behaviour more translational, while low k_θ can suppress the response entirely in Zones 1 and 2 and, for the most extreme case, also in Zone 3. Finally, the inflow speed U_∞ has the strongest influence on the response level. Increasing U_∞ generally promotes larger oscillation amplitudes, particularly in the robust Zone 3, whereas Zone 2 remains a marginal feature with comparatively small amplitudes.

Overall, the sensitivity study confirms that the predicted unstable orientations are robust with respect to parameter changes, while the response amplitudes are controlled by stiffness levels, torsional compliance, and especially the inflow velocity. The observed trends are consistent with the expected physical behaviour of a coupled quasi-steady galloping model, indicating that the implementation responds appropriately to systematic parameter perturbations. This provides confidence in the modelling approach and supports its use for the subsequent case-study evaluations.

4.6. Results Model 18A

This section summarises the time-domain simulations for the three added-mass scenarios introduced in Section 4.4. Response levels are reported using the resultant amplitude of the end-window, evaluated over the final 40 seconds of each run. All results correspond to a fixed inflow speed of $U_\infty = 0.45\ \mathrm{m/s}$, to compare the results.

Figure 4.13 shows A_{end} over the full inflow-direction sweep, $\psi \in [0°, 180°]$, for all three added mass models. For most angles the oscillations decay and the amplitude of the response approaches zero, indicating a stable coupled 3DOF system for the adopted stiffness and damping. Non-zero amplitudes appear only in three separated angular bands. These bands align with the Den Hartog screening intervals identified in Section 4.3, so the quasi-steady galloping indicator and the fully coupled time-domain simulations point to the same locations of potential vulnerability.

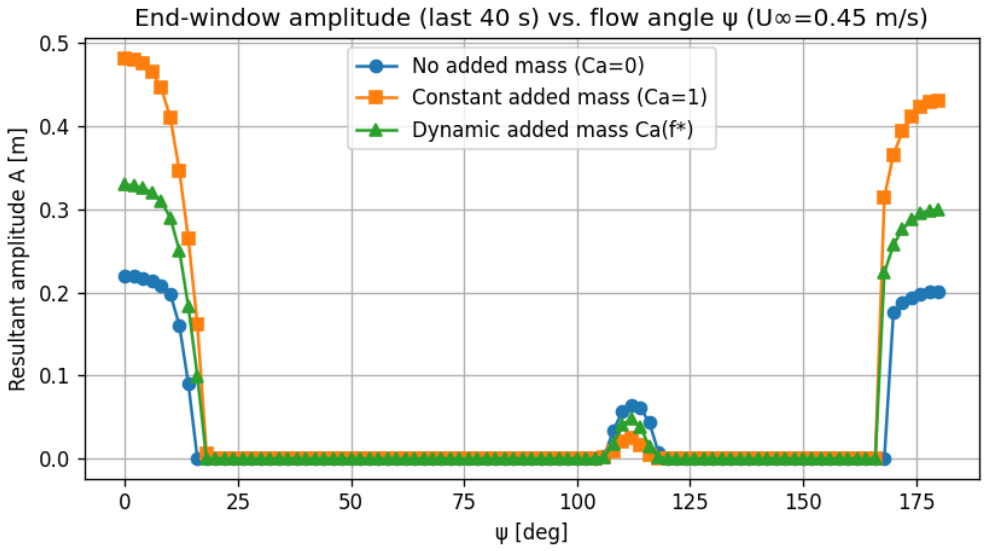

Figure 4.13: Full inflow-direction sweep of A_{end} at $U_\infty = 0.45\ \mathrm{m/s}$ for the three added-mass scenarios.

Two trends stand out from Fig. 4.13. First, the onset and decay angles of the three response regions are very similar across the added-mass models, which suggests that the angular localisation is mainly set by the quasi-steady coefficient behaviour. Second, the amplitude level is highly sensitive to the inertia model once a limit cycle is established. In the dominant regions (Zones 1 and 3), the constant added mass model produces the largest amplitudes, the frequency-dependent model gives intermediate values, and neglecting added mass yields the smallest response. This ordering is consistent with added mass increasing the effective translational inertia, lowering the wet natural frequencies, and thereby increasing the effective reduced velocity at fixed U_∞. This typically promotes larger post-onset galloping oscillations. The second screening band (Zone 2) behaves differently compared to Zone 1 and 3. It remains a small-amplitude feature in all cases, and its amplitude of the case with the neglected mass is the largest in this zone. This indicates that this interval is only marginally unstable and more sensitive to coupled dynamics and damping.

In the figures in the coming subchapters, the vertical dotted lines mark the Den Hartog boundaries of each screening interval. This has been done to provide a direct visual comparison between the quasi-steady stability prediction and the time-domain response.

4.6.1. Case 1: No added mass

Figures 4.14–4.16 zoom into the three Den Hartog screening zones for Case 1. As mentioned previously, the response map is strongly direction-dependent. Outside the windows of Figures 4.14–4.16 the solution returns to equilibrium, while inside the windows the motion gives significant amplitudes.

In Zone 1 (Fig. 4.14), the largest response occurs at the smallest inflow angles and then drops off quickly with increasing ψ. The Den Hartog boundary marks the angle where the quasi-steady indicator switches back to stable behaviour. Around this boundary the time-domain amplitudes indeed start to collapse, but coupled response does not vanish exactly at the Den Hartog line. The amplitudes persist for a few degrees beyond the predicted boundary point before the oscillations decay to zero. This small offset is expected in a nonlinear 3DOF system, where finite-amplitude effects and modal coupling can sustain motion slightly beyond a linear small-amplitude stability boundary.

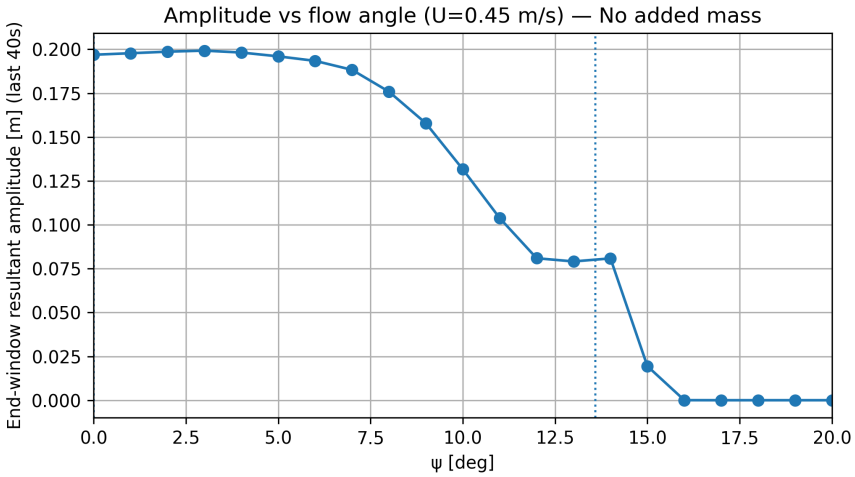

Figure 4.14: End-window resultant amplitude A_{end} for Case 1 in Zone 1

As mentioned before, Zone 2 (Fig. 4.15) shows a much weaker response than Zones 1 and 3. The curve forms a smooth bump within the Den Hartog interval, with a peak around $\psi \approx 112°$. It decays back to zero as ψ approaches the upper boundary. The fact that the response remains small throughout this zone suggests that the negative-damping margin is limited here.

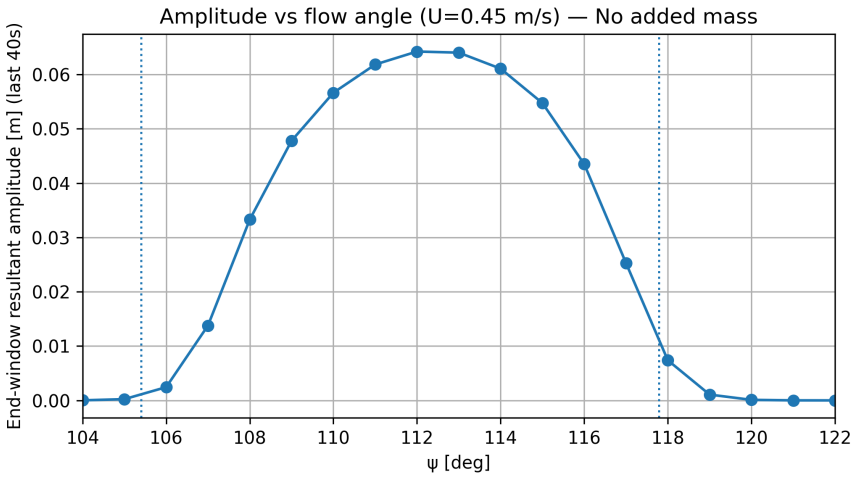

Figure 4.15: End-window resultant amplitude A_{end} for Case 1 in Zone 2

In Zone 3 (Fig. 4.16), the response remains close to zero until the Den Hartog boundary has been reached. Once triggered, the amplitude of the osscilations increases monotonically towards $\psi = 180°$ and then approaches a plateau. This monotonic growth indicates that the effective instability strengthens as the inflow direction approaches the most critical orientation at $\psi = 180°$,.

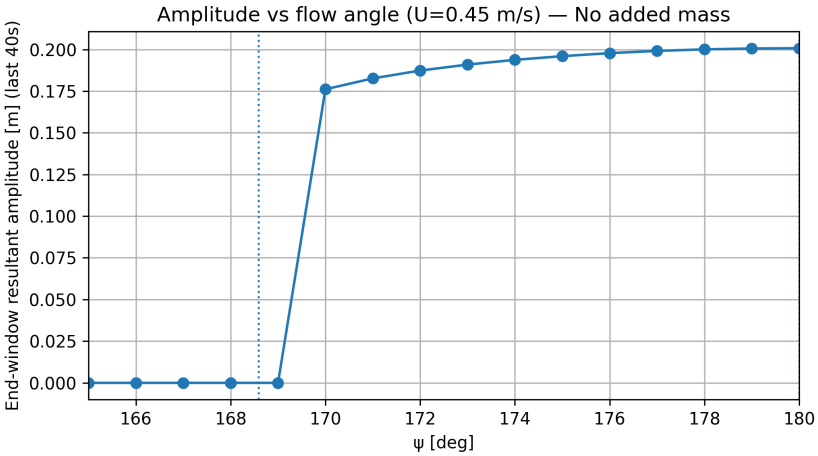

Figure 4.16: End-window resultant amplitude A_{end} for Case 1 in Zone 3

4.6.2. Case 2: Constant added mass ($C_{a,x} = C_{a,y} = 1$)

Figures 4.17–4.19 show the same three Den Hartog screening zones for the constant added-mass model. The angular locations of onset and decay remain close to those of Case 1, which again confirms that the directional sensitivity is primarily governed by the quasi-steady coefficient behaviour. However, once a response is triggered, the amplitude level increases substantially. This indicates that the added-mass treatment mainly affects the post-onset response magnitude, rather than the existence or position of the response windows.

In Zone 1 (Fig. 4.17), the response again peaks at the smallest inflow angles and then decreases as ψ increases. Compared to Case 1, the maximal values at the lower end of the interval are significantly higher, which shows that the same negative-damping mechanism drives larger oscillations when hydrodynamic inertia is included. The vertical dotted lines provide a useful reference, the collapse of the response still occurs again beyond the predicted quasi-static point.

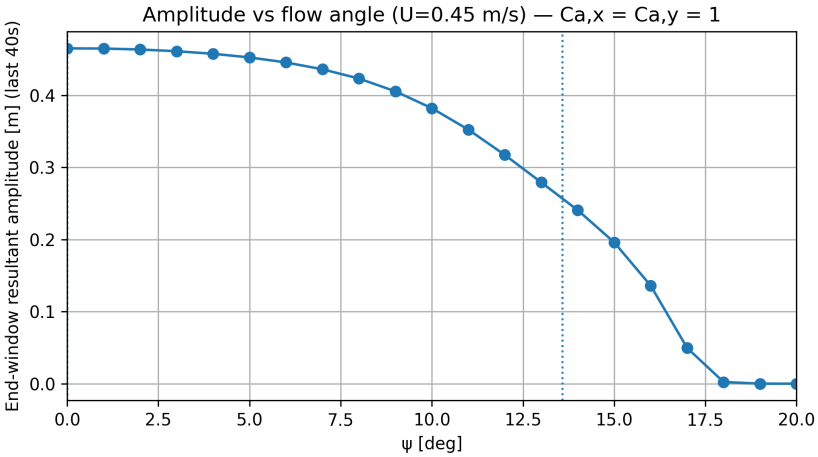

Figure 4.17: End-window resultant amplitude A_{end} for Case 2 in Zone 1

Zone 2 (Fig. 4.18) remains a weak feature, the amplitude is even significantly lower then for the case without added mass. The amplitude forms a small bump contained within the Den Hartog boundaries and decays rapidly towards both edges. Relative to the dominant zones, the response level is low, which suggests that this interval corresponds to a marginal instability where the negative-damping margin is small. In this zone, changes in added mass mainly shift the coupled dynamics and phase relations, rather than producing a strong amplification of the limit cycle.

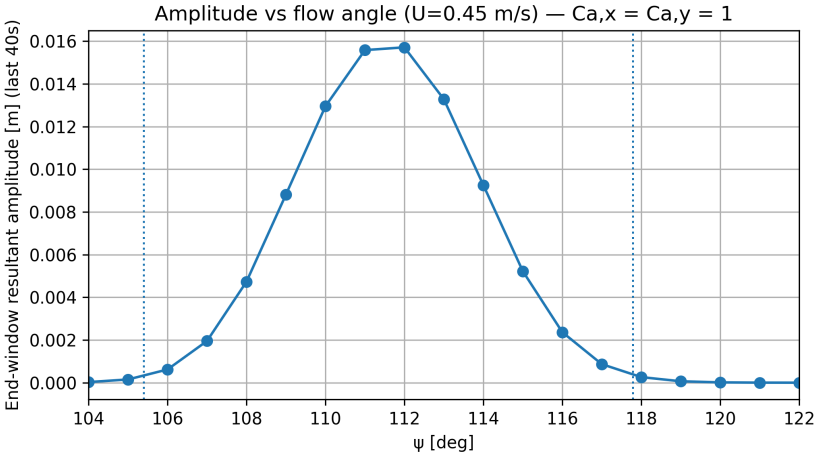

Figure 4.18: End-window resultant amplitude A_{end} for Case 2 in Zone 2

In Zone 3 (Fig. 4.19), the response remains near zero until a distinct onset close to the lower Den Hartog boundary. After onset, the amplitude increases monotonically towards $\psi = 180°$ and approaches a clear plateau. The dotted line again marks the beginning of the predicted unstable window and matches well with the observed triggering angle. The higher plateau level compared to Case 1 confirms that constant added mass is a first-order contributor to the predicted post-onset amplitude in this configuration.

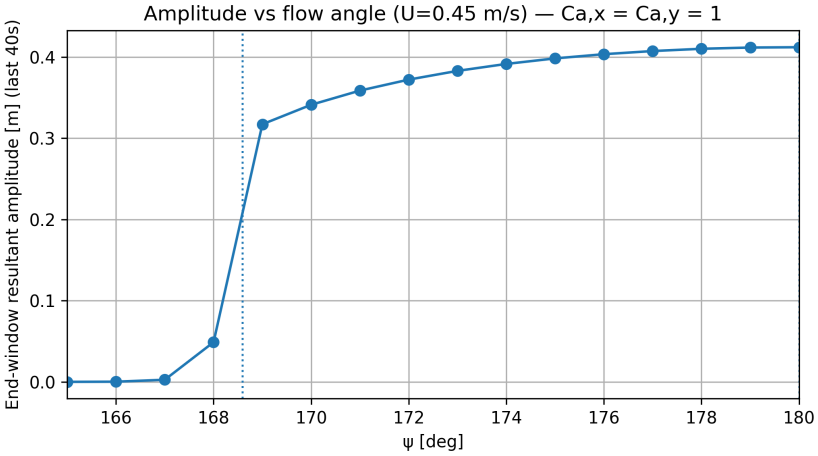

Figure 4.19: End-window resultant amplitude A_{end} for Case 2 in Zone 3

4.6.3. Case 3: Frequency-dependent added mass ($C_a(f^*)$)

Figures 4.20–4.22 present the results for the frequency-dependent added-mass implementation. The same three response windows are plotted, and the onset angles remain close to the Den Hartog bounds. This again supports that the Den Hartog function primarily determines the angular localisation of instability. In terms of magnitude, the response levels fall between Case 1 and Case 2 in all the zones.

In Zone 1 (Fig. 4.20), the response follows the same pattern as in the previous cases. A high amplitude at the lower end of the interval and a rapid decay with increasing ψ. Compared to Case 2, the plateau of the response is slightly lower. This can be explained by the frequency-dependent model, which implies a smaller effective inertia over the encountered reduced-frequency range. The decay still occurs close to the Den Hartog boundary, which is consistent with the nonlinear and coupled character of the 3DOF response.

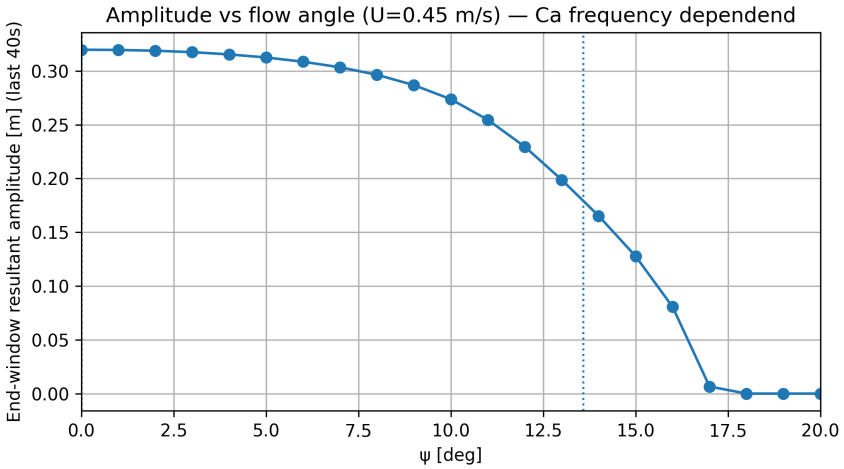

Figure 4.20: End-window resultant amplitude A_{end} for Case 3 in Zone 1

Zone 2 (Fig. 4.21) remains a small bump contained between the Den Hartog lines, with a peak near the middle of the interval and rapid decay towards both edges. The persistence of this feature across all inertia models indicates that Zone 2 is mainly driven by the quasi-steady coefficient behaviour, while inertia effects only tune an already weak response. This behaviour is in line with interpreting Zone 2 as a marginal galloping interval.

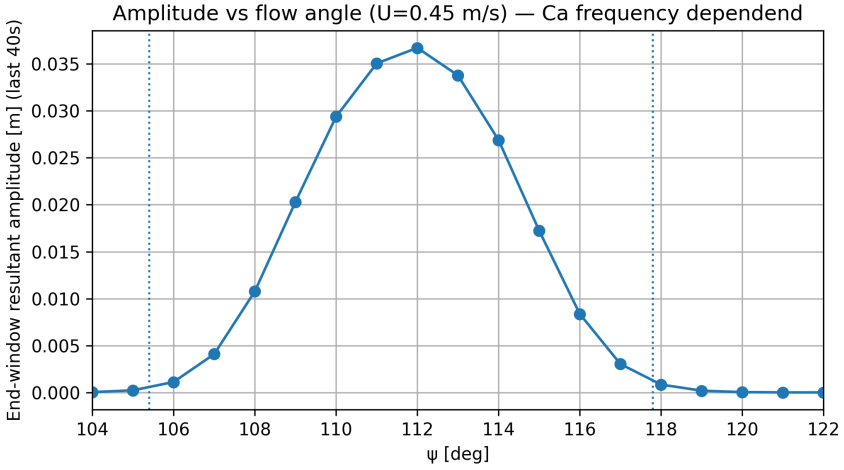

Figure 4.21: End-window resultant amplitude A_{end} for Case 3 in Zone 2

In Zone 3 (Fig. 4.22), the response stays near zero until the lower Den Hartog boundary is approached. When the boundary has been reached, the oscillations develop and grow monotonically towards $\psi = 180°$. The curve then saturates smoothly to a plateau. The overall shape matches the expected response, while the reduced plateau relative to Case 2 highlights the effect of incorporating frequency dependence when estimating the magnitude of the response.

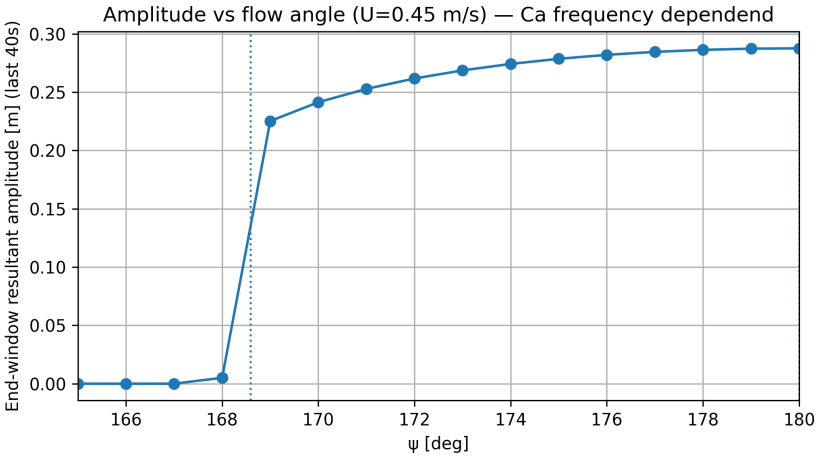

Figure 4.22: End-window resultant amplitude A_{end} for Case 3 in Zone 3

4.6.4. Comparison across zones

In Zone 1 (Fig. 4.23), the response is highest at the smallest inflow angles and then drops quickly as ψ increases. The Den Hartog lower boundary marks the start of the potentially unstable region, and the response is indeed concentrated in this interval. A small response tail persists slightly beyond the upper Den Hartog boundary before the oscillations fully decay. This is expected for a coupled 3DOF nonlinear model, where finite-amplitude effects and coupling can keep the amplitudes a few degrees past the stability limit. In this zone, Case 2 produces the largest amplitudes, Case 3 is intermediate, and Case 1 gives the smallest response. This ordering follows from the effective translational inertia. In Case 3 the frequency-dependent formulation yields an effective added-mass coefficient that lies between 0 and 1. As a result, added mass mainly controls the post-onset amplitude level, while the inflow-angle interval where the response occurs is only weakly affected.

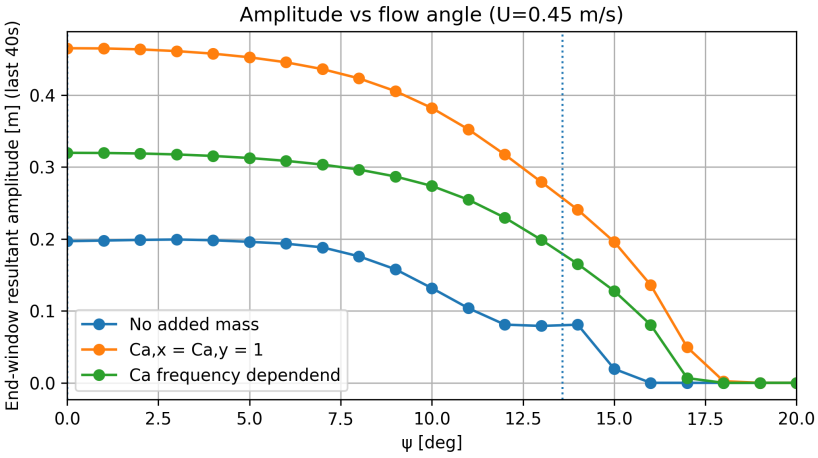

Figure 4.23: Direct comparison of end-window resultant amplitude A_{end} across the three added-mass scenarios in Zone 1

Zone 2 (Fig. 4.24) behaves differently. The response remains small for all three models and appears as a narrow bump centered near $\psi \approx 112°$. The bump is contained between the Den Hartog boundaries and decays to near zero at both edges. This indicates that the instability margin is limited in this interval. In addition, the ordering between the added-mass models is not consistent in Zone 2. Small changes in inertia and the coupled phase between translation and rotation can change the final amplitude in this marginal zone. Therefore, Zone 2 should be interpreted as a weak or borderline instability region, where the response level is sensitive to details of the coupled dynamics rather than being dominated by added mass alone.

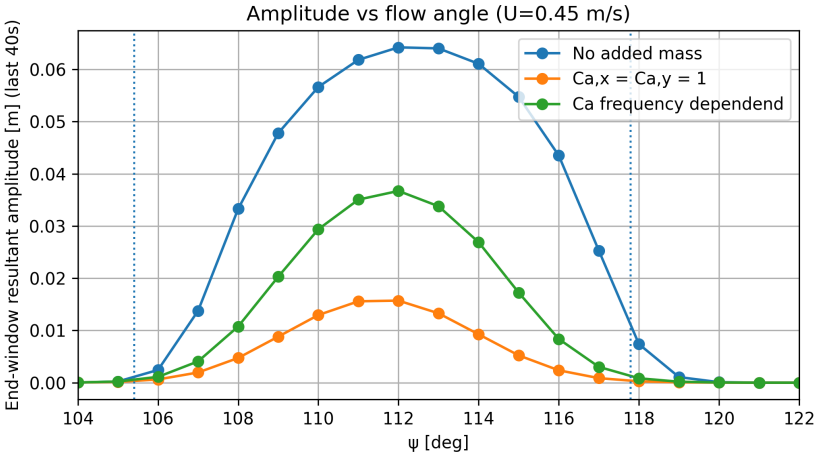

Figure 4.24: Direct comparison of end-window resultant amplitude A_{end} across the three added-mass scenarios in Zone 2

In Zone 3 (Fig. 4.25), all cases show a clear onset close to the lower Den Hartog boundary, followed by a steady increase towards $\psi = 180°$ and then a clear plateau. Compared to Zone 1, the match between the Den Hartog boundary and the observed onset is closer, and the response persists over the full upper-angle interval once it starts. This indicates that Zone 3 corresponds to a stronger and more persistent instability region. Case 2 produces the highest plateau, Case 3 yields intermediate values, and Case 1 is the lowest. The intermediate plateau in Case 3 reflects that the frequency-dependent formulation activates an effective added-mass coefficient lower than 1 over the realised response-frequency range in this zone. This shows that hydrodynamic inertia mainly controls the post-onset oscillation level, while the Den Hartog indicator primarily determines where the unstable window is located in ψ.

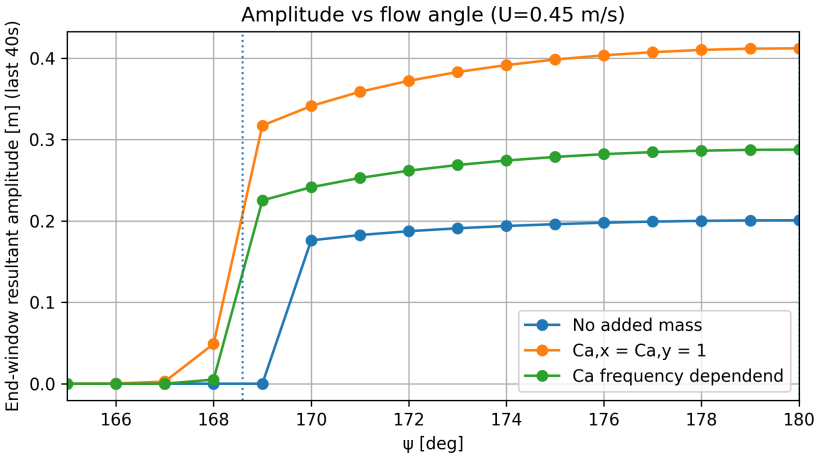

Figure 4.25: Direct comparison of end-window resultant amplitude A_{end} across the three added-mass scenarios in Zone 3

Overall, the comparison across zones shows that the three added-mass models predict the same three response-active windows, which supports that the angular localisation is primarily governed by the quasi-steady coefficient behaviour. Once oscillations develop, the response magnitude is strongly affected by the inertia model in Zones 1 and 3, while Zone 2 remains a small and more sensitive feature.

4.6.5. Conclusion Model 18A

The time-domain results for Model 18A show a clear direction-dependent response across all three added-mass scenarios. The response-active windows align well with the intervals predicted by the Den Hartog screening. Outside these zones the oscillations decay to zero, while within the bands the coupled 3DOF system develops sustained amplitudes. This indicates that the quasi-steady Den Hartog indicator provides a reliable first-order tool to localise vulnerable inflow directions for Model 18A, even though the final response is governed by nonlinear coupled dynamics.

Hydrodynamic inertia mainly affects the post-onset amplitude level. In Zones 1 and 3, Case 2 produces the largest amplitudes, Case 3 yields intermediate values, and Case 1 gives the smallest response. This ranking follows from the effective translational inertia. The frequency-dependent formulation in Case 3 activates an effective added-mass coefficient that is below the constant assumption over the response-frequency range. As a result, Case 3 moderates the amplification relative to Case 2 while still predicting higher amplitudes than Case 1.

A minor deviation from the Den Hartog boundaries is that oscillations can persist a few degrees beyond the predicted neutral points near the window edges. This is expected in a nonlinear coupled system, where finite-amplitude effects and modal interaction can sustain motion slightly beyond a small-amplitude stability boundary. Overall, the results support the modelling approach. Den Hartog screening localises the susceptible intervals, while the added-mass treatment primarily determines the response magnitude once instability develops.

4.7. Comparison between Model 18A and Model 32A

This section compares the simulated galloping response of Model 18A and Model 32A using the same numerical set-up. The comparison focuses on the hydrodynamic coefficient representation, the Den Hartog screening, and the influence of added mass on the response.

Hydrodynamic coefficient representation: For both cross-sections, the hydrodynamic forces have been modelled using fitted coefficient functions of the instantaneous effective angle of attack. For Model 18A, the Fourier representation could be kept to a limited order to maintain realistic curves. This avoided unnecessary curves associated with higher-order fitting. In contrast, the coefficient curves for Model 32A required a higher-order (10^{th} order) representation to reproduce the measured variation in $C_L(\alpha)$. This increases the risk of overfitting and leads to more oscillatory coefficient behaviour. As a consequence, small fitting imperfections can cause shifts in the Den Hartog indicator and the predicted screening boundaries.

Den Hartog criteria: These differences can be seen in the agreement between Den Hartog screening and the simulated response. For Model 18A, the response-active windows from the simulations align well with the intervals from the Den Hartog criteria. Outside these zones the amplitudes decays to zero, while within the zones significant oscillations occur. This indicates that the Den Hartog criteria is a reliable first-order localisation tool for vulnerable inflow directions for Model 18A. For Model 32A, the agreement is clearly weaker. The onset and decay angles show significant offsets relative to the Den Hartog angles. The mismatch can best be seen in Zone 1, where the simulated response extends beyond the predicted unstable interval and the location of the response window differs noticeably from the quasi-steady prediction.

Influence of added mass and inertia modelling: For both cross-sections, the simulations confirm that the added-mass treatment strongly affects the response magnitude. The angular localisation of response the windows is approximately the same for each of the models. Therefore, it can be concluded that this is primarily governed by the coefficients. In Model 18A, the amplitude ordering is consistent in the dominant zones. The constant added-mass model produces the largest amplitudes, the frequency-dependent model yields intermediate values, and the no-added-mass case gives the smallest response. This can be explained by the fact that the increase in effective translational inertia, reduces the natural frequencies. This leads to faster motions with higher amplitudes. For Model 32A, the inertia sensitivity remains, but the order changes between the different zones. The frequency-dependent added mass yields the largest amplitudes, except in Zone 4. The constant-added-mass case is in most cases conservative. This indicates a stronger sensitivity to coupled phase relations and effective frequency content for Model 32A with the current model set-up and assumptions.

Overall assessment and implications. In general, Model 18A provides a clear and stable indication of the response. The Den Hartog screening predicts well the inflow angles at which galloping occurs, and changing the added-mass model mainly changes the amplitude once the motion is unstable. For Model 32A this is less clear. The simulated angles do not match the angles of the Den Hartog criteria and the results are more sensitive due to the higher-order coefficient fit. Therefore, the results of the Model 32A should be treated more carefully, and the coefficient fitting should be improved and checked before using the model for this cross-section.

5

Conclusions, limitations and recommendations

This chapter summarises the outcomes of the thesis and reflects on the results. First, the limitations of the modelling approach are outlined to support correct interpretation of the predicted onset conditions and response amplitudes. Next, the main research question and subquestions are answered based on the findings of the thesis. The chapter then presents the overall conclusions. Subsequently, the original research questions proposed in the literature review are revisited to clarify how the present work contributes to that initial ambition and to identify the remaining gaps toward a complete system-level predictive capability for the VTS. Finally, recommendations for future work are provided to improve the validity and applicability of the modelling framework.

5.1. Limitations

The modelling choices in this thesis were made to obtain a tractable, transparent, and verifiable cross-sectional galloping framework. As a result, the following limitations should be taken into account when interpreting the predicted onset conditions and response amplitudes. The points are structured from most important to least important in terms of their expected influence on the conclusions.

Quasi-steady forcing: The hydrodynamic loading is modelled using a quasi-steady approach in which forces and moment are obtained from static MARIN simulations. The coefficient curves are generated by placing the cross-section in a steady inflow while keeping it fixed, meaning that the cross-section cannot translate or rotate during the simulations. The coefficients therefore represent time-averaged values at an instantaneous effective angle of attack. This implies that unsteady flow physics are not explicitly resolved. This limitation is particularly relevant near the galloping onset boundary, where the system is marginally stable and small differences in the predicted forces can determine whether the amplitude of the movement decays or grows. As a result, the use of time-averaged quasi-steady coefficients may shift the predicted onset condition, leading to a slightly changed estimate of the critical boundaries and its response.

Velocity dependence in coefficient applicability: The main inflow-direction sweep is reported at a fixed reference velocity of $U_\infty = 0.45\,\mathrm{m/s}$ and subsequently explored through targeted variations. This was done because the available $C_D(\alpha)$ and $C_L(\alpha)$ data were obtained for this specific velocity. The paper of Chabart and Lilien [7] reports a limited sensitivity of the coefficients to velocity for an isolated body. However, the used configuration in water exhibits a stronger and more complex velocity dependence due to wake interaction, which increases the uncertainty when applying the coefficients outside $U_\infty = 0.45\,\mathrm{m/s}$. As a result, the identified critical angles and response amplitudes can shift with velocity and parameter combinations, and the transferability of results beyond the tested operating point is limited.

Limited validation for the case-study geometry: The numerical implementation is verified by reproducing a published benchmark case. However, the project-specific cross-section results are not directly validated against dedicated experimental measurements or high-fidelity CFD for that geometry. Therefore, the outcomes of the case-study should be interpreted primarily as model-based predictions and trends within the chosen framework. They should not be considered fully validated absolute values for onset conditions and response amplitudes.

Idealized flow conditions: The inflow is treated as steady and uniform during the simulations. This excludes variations that may occur in operational conditions. In addition, during the thesis waves have been neglected. Therefore, any modulation of the local flow velocity and direction by waves are not represented. Such inflow variability can modify effective angles of attack or forces on cylinders. Therefore, it can influence both onset and response behaviour. The predicted stability and amplitude levels correspond to idealized conditions and may differ under realistic environmental loading.

Added-mass ellipse approximation: The added-mass properties of the project-specific cross-section are approximated using an equivalent ellipse. This provides a practical way to estimate the hydrodynamic inertia within the cross-sectional modelling framework, but it remains a geometric simplification. As a result, local shape features, like the gaps between the cylinders, are not explicitly represented in the added-mass estimate. This can lead to differences in the effective inertia and wet natural frequencies between the equivalent ellipse and the true cross-section geometry. This can result in a change in the predicted onset conditions and response amplitudes. At the same time, the ellipse approximation allows for direction-dependent added-mass (different values in the x and y directions), which is expected to be more realistic for a non-circular cross-section than assuming identical added-mass values in both directions.

Frequency dependence implemented using data for a single cylinder: The frequency-dependent added-mass behaviour is introduced using a formulation derived for a single cylinder. Applying this behaviour to an interfering multi-cylinder configuration is an approximation, because interference effects can alter the effective inertia response. As a result, the frequency-dependent added-mass implementation in this thesis should be regarded as a practical approximation to explore the potential impact of frequency dependence, rather than as a fully representative model of the added-mass dynamics for interfering cylinders.

Diagonal added-mass assumption: The added-mass matrix is assumed to be diagonal, meaning that all coupling terms are neglected. The added mass in the x-direction is assumed not to depend on motion in the y-direction, and coupling between translation and rotation is ignored. For a single, symmetric body this can be a reasonable approximation. However, for the present multi-cylinder configuration this is mainly a simplification, because the flow around one cylinder can influence the effective inertia of the other. If these coupling effects are relevant in reality, they can change the coupled motion and may shift the predicted onset conditions and response levels.

5.2. Answers to the research questions

Sub-question 1: *To what extent can a published galloping model be reproduced and used as a verified benchmark for this thesis?*

The benchmark study shows that the numerical implementation reproduces the key features of the published reference case. The coefficient fitting reproduces the Den Hartog instability intervals reported in the original study, and the time-domain simulations for representative operating conditions match the reference response characteristics [7]. This supports that the coupled equations of motion, damping and stiffness implementation, and coefficient handling are correctly implemented. The framework is therefore sufficiently verified for application to the project-specific cross-sections.

Sub-question 2: *What are the predicted critical flow angles for galloping of the project-specific cross-sections?*

For Model 18A, Den Hartog screening evaluated from the fitted MARIN coefficients yields four zero-crossings at $\alpha = 13.58°$, $105.40°$, $117.79°$, and $168.59°$, defining three potentially unstable angular zones. These are referred to as Zone 1 ($0° \leq \alpha \leq 13.58°$), Zone 2 ($105.40° \leq \alpha \leq 117.79°$), and Zone 3 ($168.59° \leq \alpha \leq 180°$). The time-domain simulations show sustained responses predominantly within these same bands, with small deviations near the boundaries.

For Model 32A, the Den Hartog function exhibits multiple zero-crossings, resulting in several narrow potentially unstable intervals. For interpretation and simulation, these intervals are grouped into four broader response-active zones. The time-domain simulations confirm a direction-dependent response with four distinct response-active zones. The zones have slight offsets between the Den Hartog boundaries compared to Model 18A, especially in the first zone.

Sub-question 3: *How does the added-mass formulation affect the onset of galloping and the response amplitude?*

For both cross-sections, changing the added-mass treatment has a limited effect on where the response occurs in terms of inflow direction. However, it has a clear influence on the response amplitude once galloping is triggered. For Model 18A, the dominant zones show a clear ranking. The constant added-mass case produces the largest amplitudes, the frequency-dependent model yields intermediate values, and neglecting added mass gives the smallest response. This follows from the effective translational inertia. Including added mass promotes larger post-onset oscillations. In Case 3, the realised response frequencies activate effective values below the constant $C_a = 1$ assumption (and above zero), which explains the intermediate amplitudes.

For Model 32A, inertia sensitivity remains strong but the amplitude ranking varies between zones. In several zones the frequency-dependent formulation yields the largest amplitudes, while in the most dominant zone the constant added-mass case remains highest. This indicates that the response is more sensitive to the realised frequency content and phase relations in the coupled 3DOF dynamics. As a result, a constant $C_a = 1$ is not uniformly conservative for Model 32A within the present modelling set-up.

Main research question: *To what extent can a cross-sectional galloping modelling framework be used to predict the onset and response of galloping for the project-specific cross-sections, as a basis for galloping prediction of the full VTS?*

The developed framework can provide consistent model-based predictions of which inflow directions are most susceptible to galloping. The framework also shows how the response amplitude changes once instability is triggered. For Model 18A, Den Hartog screening provides a reliable first localisation of critical inflow-angle windows, and time-domain simulations con-

firm significant amplitude responses within these intervals. For Model 32A, the framework still predicts direction-dependent response windows, but the agreement with Den Hartog screening is weaker and the predicted boundaries are more sensitive to the higher-order coefficient representation. Overall, the framework is useful for screening and comparative sensitivity studies, but its predictive robustness depends strongly on the quality and smoothness of the underlying coefficient data, particularly for Model 32A.

5.3. Conclusion

In this thesis, a cross-sectional, 3DOF time-domain framework has been developed and applied to assess galloping of two project-specific cross-sections (Models 18A and 32A). The numerical implementation was verified by reproducing a published benchmark case, demonstrating that the coefficient-processing workflow and the coupled equations of motion are implemented correctly.

For Model 18A, the results show a clear and physically consistent direction-dependent galloping behaviour. Den Hartog screening identifies the main susceptible inflow-angle intervals, and time-domain simulations confirm sustained oscillations within these windows. The added-mass formulation mainly affects the response magnitude after onset, while the inflow-direction localisation remains largely governed by the hydrodynamic coefficients. In the frequency-dependent formulation, the effective added mass coefficient can become negative over parts of the reduced-frequency range, which reduces the effective inertia and can therefore change the response level and, in some cases, the amplitude ordering between inertia models.

For Model 32A, the simulations also show strongly direction-dependent response with multiple response-active zones. However, compared to Model 18A, the predicted onset and decay angles show larger offsets relative to Den Hartog screening. This reduced agreement is consistent with the higher sensitivity introduced by the higher-order coefficient fit needed for Model 32A. As a result, the Model 32A predictions should be interpreted more cautiously, and improving the robustness of the coefficient representation is essential before drawing design-level conclusions for this geometry.

Overall, the cross-sectional 3DOF framework provides a verified and internally consistent basis for identifying critical inflow-angle windows where galloping-type instability can occur. Also the implementation of different inertia models are verified across both cross-sections. In that sense, the model is well-suited as an early-stage screening tool. It efficiently localises susceptible angular zones and helps prioritise orientations for further investigation.

At the same time, the present framework should not be interpreted as a fully reliable predictor of exact onset boundaries or absolute response amplitudes. Its predictive accuracy remains limited by the quasi-steady cross-sectional assumptions and by the quality and representation of the hydrodynamic coefficient data. This is reflected most clearly in the reduced agreement observed for Model 32A, where small changes in the fitted coefficient curves can shift predicted critical angles and alter stability classification. As a result, the numerical outcomes should be regarded as indicative rather than definitive, particularly for the implementation in complex geometries like the VTS cross-sections. Recommendations for improving the framework and increasing its predictive robustness are presented in Chapter 5.5.

5.4. Reflection on proposed research questions

This section revisits the original research questions proposed in the literature review and positions the outcomes of this thesis within that initial research ambition. While the thesis began with the broader objective of predicting the vibration response of the VTS under varying flow conditions, the work was scoped toward developing and validating a sectional prediction framework and applying it to representative VTS cross-sections. The section will restate the proposed main question and sub-questions, summarise the contributions achieved in this research, and identify the remaining gaps to fully address the original questions at system level.

5.4.1. Proposed research questions

At the start of this research project, the following main research question and sub-questions were proposed to guide the overall scope of the work. These questions define the broader objective of developing a predictive capability for FIV response of the VTS under varying flow conditions. The questions were as follows:

'What are the key components required to develop a predictive model for estimating the vibration response caused by flow-induced vibrations of the vertical transport system under varying flow conditions?'

- How do geometric characteristics of the vertical transport system influence its susceptibility to flow-induced vibrations?
- Which flow-induced vibration mechanisms are relevant to the vertical transport system, and how do they contribute to the vibration response?
- How do varying flow conditions affect the onset and amplitude of flow-induced vibrations in the system?

5.4.2. Contribution of this thesis to the proposed research questions

The proposed research questions were initially broad and aimed at developing a predictive capability for the full VTS under varying flow conditions. The work in this thesis contributes to that ambition by establishing and verifying a cross-sectional modelling framework. This framework screened the VTS cross-sections for galloping susceptibility across inflow orientations, and by identifying which modelling choices most strongly influence predicted onset and response levels. In this sense, the thesis provides a modelling framework that can be expanded toward a system-level predictive model.

Main question: Key components for a predictive model. This thesis contributes several components required for the full-scale prediction model. First, a verified time-domain simulation framework is established. Second, hydrodynamic coefficients are processed into continuous functions of inflow angle, enabling both Den Hartog screening and nonlinear time-domain simulations to identify susceptible orientations and quantify response amplitudes. Finally, different added-mass formulations are implemented and compared, showing which choices mainly shift onset localisation and which primarily change response magnitude.

Sub-question 1: Influence of geometric characteristics. The influence of geometry is addressed by applying the same framework to two project-specific cross-sections (Models 18A and 32A). For both cross-sections the direction-dependent instability windows and response characteristics have been investigated. The results show that geometry can lead to markedly different susceptibility patterns. Model 18A exhibits stable and physically consistent response-active windows that align well with Den Hartog screening. Model 32A shows narrower windows and stronger sensitivity to coefficient representation. This comparison shows that the predicted galloping susceptibility is strongly governed by geometry-driven differences in the lift, drag, and moment coefficients.

Sub-question 2: Relevant FIV mechanisms and their contribution. The thesis primarily contributes to this question by developing predictive capability for one specific FIV mechanism: galloping. The sectional model includes coupled translation–rotation effects. Other mechanisms that may contribute to the overall VTS response, such as VIV and wake-induced vibration, are not modelled explicitly in the present framework. The thesis therefore clarifies what can be predicted within the current scope and identifies which additional physics and modelling modules would be required to quantify the relative contribution of other mechanisms to the total response.

Sub-question 3: Effect of varying flow conditions on onset and amplitude. Within the modelling assumptions, the thesis directly addresses variation in inflow direction through the orientation sweep of the inflow. The results further show how key modelling choices influence both the predicted onset and the post-onset response amplitudes. The results indicate that inflow direction strongly governs where galloping occurs, while hydrodynamic inertia modelling primarily controls amplitude levels once instability is triggered. However, the available coefficient data set limits the assessment of broader flow variability. The dataset is tied to a reference velocity (0.45 m/s) and the inflow is treated as steady and uniform. As a result, the thesis provides a controlled baseline assessment and identifies the steps needed to extend the predictive capability to more realistic, time-varying flow conditions relevant to operation.

Overall, this thesis advances the proposed research questions by delivering a verified sectional screening tool and by demonstrating its application and sensitivity for representative VTS cross-sections. The framework provides a consistent basis for identifying direction-dependent galloping susceptibility and for assessing how modelling choices influence predicted response trends. The remaining gaps and a recommended path toward a complete system-level predictive capability are discussed in the next subsection.

5.4.3. Remaining gaps

Although this thesis establishes a verified sectional screening capability, the proposed research questions target prediction of the full VTS response under realistic operating conditions. Closing this gap requires progress in three areas.

Hydrodynamic inputs and validation. A system-level predictive model requires hydrodynamic input data that is robust across the full range of operating conditions. This includes coefficient information over all inflow angles and for multiple velocities and validation of the project-specific cross-sections using higher-fidelity simulations or dedicated experiments.

Operating conditions and mechanism coverage. The present framework assumes steady, uniform inflow and focuses on galloping. For realistic VTS operation, time-varying flow conditions should be represented, and the role of additional FIV mechanisms, such as VIV and wake-induced effects, should be assessed to determine which mechanisms govern the response in different regimes.

Upscaling to full-length VTS response. To answer the proposed questions at system level, the verified sectional loading approach needs to be coupled to a structural model of the full VTS. This step is essential to translate local susceptibility into global response levels and fatigue-relevant load cycles and operational envelopes.

Concrete actions that address these gaps are provided in Section 5.5.

5.5. Recommendations

Several extensions can be added in future work to improve the applicability and accuracy of the framework. These items were outside the scope of the present thesis, but are expected to strengthen the model and reduce uncertainty.

Obtain motion-relevant hydrodynamics with a velocity sweep: High-fidelity CFD or dedicated experiments are recommended to build a motion-relevant hydrodynamic database for the interfering cylinder configuration at multiple inflow velocities and inflow angles, instead of relying on a single operating point at $U_\infty = 0.45\,\mathrm{m/s}$. The primary objective is to obtain reliable force and moment coefficient data, $C_D(\alpha)$, $C_L(\alpha)$ and $C_M(\alpha)$, under conditions representative of the dynamic response. This would enable a better assessment of the velocity dependence and improve the transferability of the predicted critical angles and response amplitudes. If possible, this can additionally provide guidance on unsteady effects that are not captured by the present quasi-steady approach. Overall, this step would strengthen the credibility of the coefficient input to Den Hartog screening and time-domain integration, and would provide an additional validation.

Improve coefficient robustness for Model 32A: For Model 32A in particular, it is recommended to improve and verify the coefficient representation used for Den Hartog screening and time-domain integration. The original MARIN report provides force and moment coefficients at 15° angular increments, which is relatively coarse given the sensitivity of the Den Hartog criterion to changes in the slope of the lift curve. To improve this, a refined dataset with angular steps of approximately 5° or smaller should be generated. Additionally, fitting methods with controlled smoothness should be applied, and the sensitivity of $\mathrm{d}C_L/\mathrm{d}\alpha$ and Den Hartog zero-crossings to the chosen fit should be evaluated. These steps are essential to increase the reliability and reproducibility of predicted instability windows.

Extend mechanism coverage beyond galloping: The present framework focuses on quasi-steady galloping and therefore does not account for other FIV mechanisms that may be relevant under realistic operating conditions, such as VIV and WIV. Future work should extend the modelling scope by incorporating additional instability mechanisms. This can be done by dedicated reduced-order modules or through a combined screening approach. This would enable more comprehensive risk assessment for fatigue-relevant loading, and would clarify whether predicted galloping windows remain governing when vortex shedding or wake interference effects become significant.

Improve added-mass modelling: In the present thesis, hydrodynamic inertia is represented using an equivalent-ellipse approximation. This provides a transparent baseline but may not capture inertia contributions associated with local geometry or multi-body effects in the VTS cross-sections. Future work should therefore improve the added-mass representation as an explicit modelling component. This can be done by computing geometry-specific added-mass terms and assessing whether an effective added mass varies with oscillation frequency. A refined inertia model would reduce uncertainty in predicted natural frequencies and stability boundaries.

Model extensions: Further improvements can be obtained by introducing more realistic environmental conditions and, if required for system-level assessment, by coupling the cross-sectional model to a structural model that represents the full VTS dynamics along the span. These additions were not implemented in this thesis but can be incorporated in future work to increase realism and design applicability.

References

[1] V. Balaram. “Rare earth elements: A review of applications, occurrence, exploration, analysis, recycling, and environmental impact”. In: *Geoscience Frontiers* 10.4 (2019), pp. 1285–1303. DOI: 10.1016/j.gsf.2018.12.005. URL: https://doi.org/10.1016/j.gsf.2018.12.005.

[2] International Energy Agency. *The Role of Critical Minerals in Clean Energy Transitions: Executive Summary*. Accessed: 2025-04-30. 2021. URL: https://www.iea.org/reports/the-role-of-critical-minerals-in-clean-energy-transitions/executive-summary.

[3] C. Hurst. *China’s Rare Earth Elements Industry: What Can the West Learn?* Tech. rep. Institute for the Analysis of Global Security (IAGS), 2010. URL: https://www.researchgate.net/publication/235080237.

[4] Y. Lee and T. Dacass. “Reducing the United States’ risks of dependency on China in the rare earth market”. In: *Resources Policy* 77 (2022), p. 102702. DOI: 10.1016/j.resourpol.2022.102702.

[5] X. Wang et al. “Geochemical behaviour of rare earth elements in miningbala-affected waters, southwest China”. In: *Science of the Total Environment* 957 (2024), p. 177747. DOI: 10.1016/j.scitotenv.2024.177747.

[6] K. Miller et al. “Challenging the need for deep seabed mining from the perspective of metal demand, biodiversity, ecosystems services, and benefit sharing”. In: *Frontiers in Marine Science* 8 (2021), p. 706161. DOI: 10.3389/fmars.2021.706161. URL: https://www.frontiersin.org/articles/10.3389/fmars.2021.706161/full.

[7] O. Chabart and J.-L. Lilien. “Galloping of electrical lines in wind tunnel facilities”. In: *Journal of Wind Engineering and Industrial Aerodynamics* 74–76 (1998), pp. 967–976. ISSN: 0167-6105. DOI: 10.1016/S0167-6105(98)00088-9.

[8] R. D. Blevins. *Flow-Induced Vibration*. 2nd ed. Originally published by Van Nostrand Reinhold, 1990. Malabar, Florida: Krieger Publishing Company, 1994. ISBN: 9780894648236.

[9] M. P. Paidoussis, S. J. Price, and E. de Langre. “Prisms in Cross-Flow – Galloping”. In: *Fluid-Structure Interactions: Cross-Flow-Induced Instabilities*. Cambridge University Press, 2010, pp. 15–104. DOI: 10.1017/CBO9780511762758.003. URL: https://www.cambridge.org/core/books/fluidstructure-interactions/prisms-in-crossflow-galloping/E0DB1786C6EBB9E82478AF82D02FE85D.

[10] N. Navrose and S. Mittal. “Lock-in in vortex-induced vibration: effect of mass and damping”. In: *Journal of Fluid Mechanics* 798 (2016), pp. 531–571.

[11] C. Williamson and R. Govardhan. “Vortex-induced vibrations”. In: *Annual Review of Fluid Mechanics* 36 (2004), pp. 413–455.

[12] G. R. S. Assi, P. W. Bearman, and J. R. Meneghini. “On the wake-induced vibration of tandem circular cylinders: the vortex interaction excitation mechanism”. In: *Journal of Fluid Mechanics* 661 (2010), pp. 365–401. DOI: 10.1017/S0022112010003095.

[13] J. K. Vandiver et al. “An Experimental Evaluation of Vortex-Induced Vibration of a Riser Bundle With Gaps”. In: *Proceedings of the ASME 2009 28th International Conference on Ocean, Offshore and Arctic Engineering (OMAE)*. OMAE2009-79757. ASME. Honolulu, Hawaii, USA: ASME, 2009. DOI: 10.1115/OMAE2009-79757.

[14] A. Bokaian and F. Geoola. “Wake-induced galloping of two interfering circular cylinders”. In: *Journal of Fluid Mechanics* 146 (1984), pp. 383–415. DOI: 10.1017/S0022112084001920.

[15] T. Li and T. Ishihara. “Numerical study on wake galloping of tandem circular cylinders considering the effects of mass and spacing ratios”. In: *Journal of Wind Engineering and Industrial Aerodynamics* 210 (2021), p. 104536. DOI: 10.1016/j.jweia.2021.104536.

[16] A. Names et al. “The Interaction Between Flow-Induced Vibration Mechanisms of a Square Cylinder with Varying Angles of Attack”. In: *Journal of Fluid Mechanics* 710 (2012), pp. 102–130. DOI: 10.1017/jfm.2012.307.

[17] X. Xia et al. “Galloping of two-dimensional section of a marine riser attached with fairing under different inflow angles”. In: *Ocean Engineering* 260 (2022), p. 112055. DOI: 10.1016/j.oceaneng.2022.112055.

[18] T. Kristiansen and O. M. Faltinsen. “Higher harmonic wave loads on a vertical cylinder in finite water depth”. In: *Journal of Fluid Mechanics* 833 (2017), pp. 773–805. DOI: 10.1017/jfm.2017.702.

[19] M. He and J. H. G. Macdonald. “Aeroelastic stability of a 3DOF system based on quasi-steady theory with reference to inertial coupling”. In: *Journal of Wind Engineering and Industrial Aerodynamics* 171 (2017), pp. 319–329. DOI: 10.1016/j.jweia.2017.10.013.

[20] M. He and J. H. G. Macdonald. “An analytical solution for the galloping stability of a 3 degree-of-freedom system based on quasi-steady theory”. In: *Journal of Fluids and Structures* 60 (2016). Early online date: 2015-11-13, pp. 23–36. DOI: 10.1016/j.jfluidstructs.2015.10.004.

[21] N. Nikitas and J. H. G. Macdonald. “Misconceptions and generalizations of the Den Hartog galloping criterion”. In: *Journal of Engineering Mechanics* 140.4 (2014), p. 04013005. DOI: 10.1061/(ASCE)EM.1943-7889.0000697.

[22] Z. Wen et al. “Galloping Mechanism of a Closely Tuned 3-DOF System Considering Aerodynamic Stiffness”. In: *Journal of Structural Engineering* 149.4 (2023), p. 04023014. DOI: 10.1061/JSENDH.STENG-11829.

[23] Eric J. Limacher. “Added-mass force on elliptic airfoils”. In: *Journal of Fluid Mechanics* 926 (2021), R2. DOI: 10.1017/jfm.2021.741.

[24] K. Vikestad, C. M. Larsen, and J. K. Vandiver. “Experimental study of excited circular cylinder in current”. In: *Proceedings of the 16th International Conference on Offshore Mechanics and Arctic Engineering (OMAE)*. ASME. Yokohama, Japan, 1997, pp. 231–240.

[25] K. Vikestad, J. K. Vandiver, and C. M. Larsen. “Added mass and oscillation frequency for a circular cylinder subjected to vortex-induced vibrations and external disturbance”. In: *Journal of Fluids and Structures* 14 (2000), pp. 1071–1088. DOI: 10.1006/jfls.2000.0308.

[26] F. Cui et al. “Spatial Galloping Behavior of Iced Conductors under Multimodal Coupling”. In: *Sensors* 24.3 (2024), p. 784. DOI: 10.3390/s24030784.

[27] X. Liu et al. “Galloping Stability and Aerodynamic Characteristic of Iced Transmission Line Based on 3-DOF”. In: *Shock and Vibration* 2020 (Sept. 2020). Article ID: 8828319, pp. 1–15. DOI: 10.1155/2020/8828319.

[28] L. Deng et al. “Vortex-Induced Vibration of Deep-Sea Mining Riser Under Different Currents and Tension Conditions Using Wake Oscillator Model”. In: *Journal of Marine Science and Engineering* 13.8 (2025), p. 1565. DOI: 10.3390/jmse13081565.

[29] S. W. Kim et al. “Prediction of deepwater riser VIV with an improved time domain model including non-linear structural behavior”. In: *Ocean Engineering* 236 (2021), p. 109508. DOI: 10.1016/j.oceaneng.2021.109508.

[30] J. K. Vandiver, L. Ma, and Z. Rao. “Revealing the effects of damping on the flow-induced vibration of flexible cylinders”. In: *Journal of Sound and Vibration* 433 (2018), pp. 29–54. DOI: 10.1016/j.jsv.2018.07.009.

A

Appendix A: results Model 32A

A schematic lay-out of the 32A model is shown in Figure A.1.

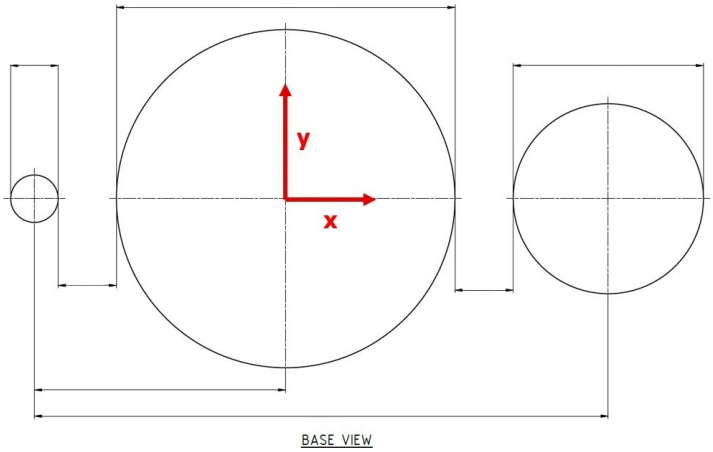

Figure A.1: Layout of the 32A model geometry

Hydrodynamic loads are again evaluated using a quasi-steady representation with a Fourier-fit. A visual can be found in Figure A.2. In contrast to the previous model, the present fit requires a higher order to reproduce the measured variation in $C_l(\alpha)$. While this improves the point-wise agreement with the available data, it also increases the risk of overfitting and introduces more oscillatory behaviour in the coefficient functions. As a consequence, small imperfections in the fitted curves can lead to noticeable changes in the Den Hartog function and the predicted screening boundaries. The resulting stability intervals and response levels should therefore be interpreted with additional caution, as the higher-order fit may be less robust and could reduce the overall accuracy of the predicted time-domain response.

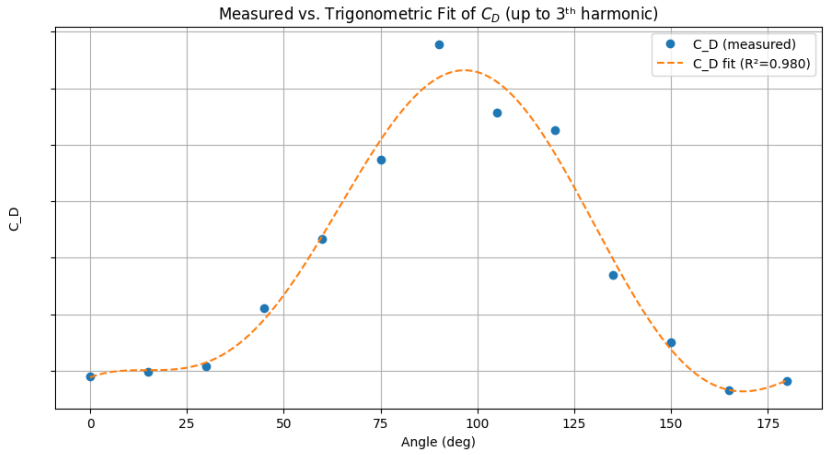

(a) $C_d(\alpha)$ curve fit

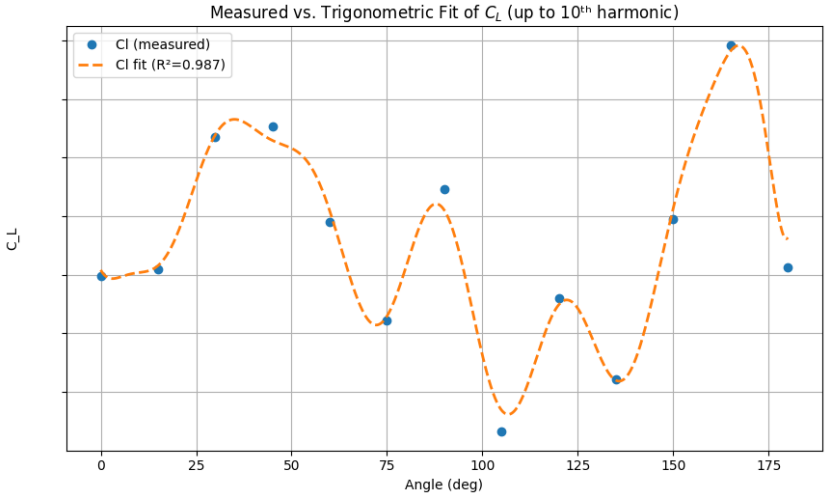

(b) $C_l(\alpha)$ curve fit

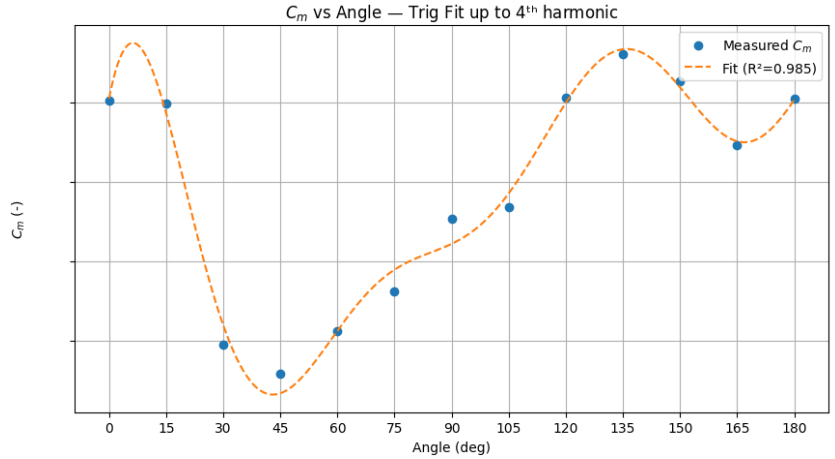

(c) $C_m(\alpha)$ curve fit

Figure A.2: Results for Fourier curve-fitting - Model 32A

Galloping results

Figure A.3 the Den Hartog criteria for the Model 32A. The zero-crossings of $H(\alpha)$ are:

$$\alpha = 1.80°, 39.12°, 41.15°, 52.78°, 69.64°, 90.55°, 104.09°, 124.84°, 133.86°, 167.67°, 179.45°. \tag{A.1}$$

Based on these crossings and Figure 4.3, angular zones with $H(\alpha) \leq 0$ are defined as:

$$\begin{aligned}
&\text{Zone 1A: } 0° \leq \alpha \leq 1.80°,\\
&\text{Zone 2A: } 39.12° \leq \alpha \leq 41.15°,\\
&\text{Zone 3A: } 52.78° \leq \alpha \leq 69.64°,\\
&\text{Zone 4A: } 90.55° \leq \alpha \leq 104.09°,\\
&\text{Zone 5A: } 124.84° \leq \alpha \leq 133.86°,\\
&\text{Zone 6A: } 167.67° \leq \alpha \leq 179.45°.
\end{aligned} \tag{A.2}$$

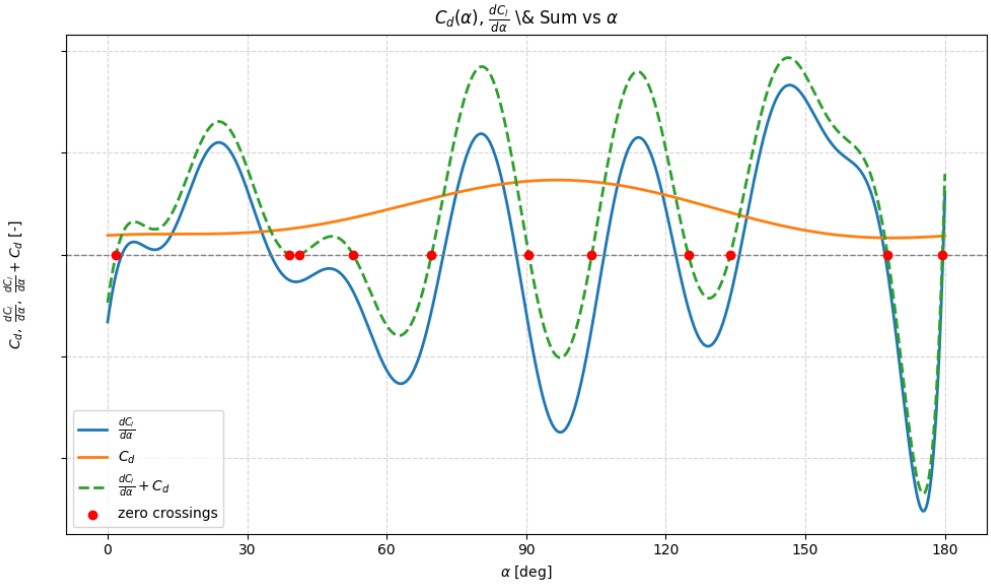

Figure A.3: Den Hartog Criteria Model 32A

Since Zone 1 spans only a very small range of inflow angles, it is not investigated further. In addition, Zones 2A and 3A are located very close to each other and are therefore combined into a single zone. Preliminary calculations also indicate that the results for these two zones show significant overlap, which further supports treating them as one. These zones which will be examined in more detail in Chapter A will there for be:

$$\begin{aligned}
&\text{Zone 1: } 39.12° \leq \alpha \leq 69.64°,\\
&\text{Zone 2: } 90.55° \leq \alpha \leq 104.09°,\\
&\text{Zone 3: } 124.84° \leq \alpha \leq 133.86°,\\
&\text{Zone 4: } 167.67° \leq \alpha \leq 179.45°.
\end{aligned} \tag{A.3}$$

Results Model 32A

This section summarises the time-domain simulations for Model 32A for the three added-mass scenarios introduced in Section 4.4. The responses have been reported using the resultant amplitude of the end-window (Eq. 4.17), evaluated over the final 40 s of each run. All results are performed with the input data from Chapter 4.4, to allow a direct comparison between the inertia treatments.

Figure A.4 shows the full sweep in inflow-directions of A_{end} over $\psi \in [0°, 180°]$ for the three inertia models. For most angles, the oscillations decay and the response approaches zero, indicating a stable coupled 3DOF system for the adopted stiffness and damping. Non-zero amplitudes occur only in four separated zones, introduced in Chapter A, labelled Zones 1–4 in the remainder of this section.

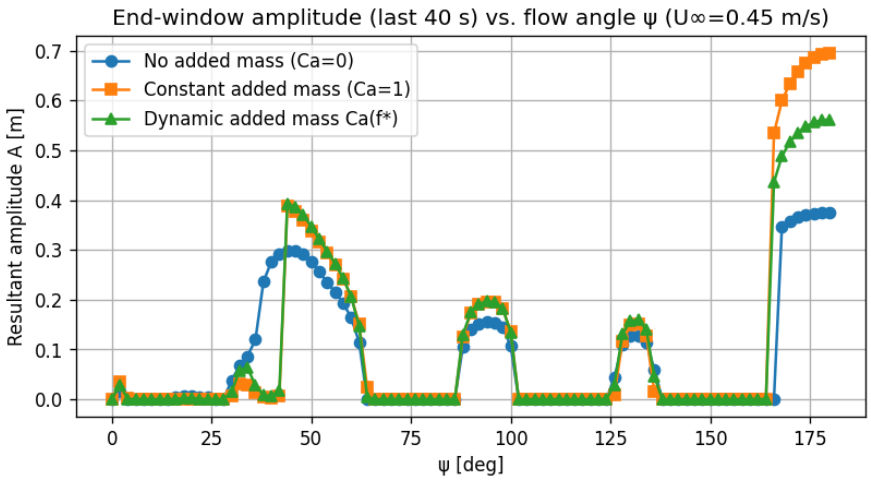

Figure A.4: Full inflow-direction sweep of A_{end} at $U_\infty = 0.45$ m/s for the three added-mass scenarios.

Two trends stand out from Fig. A.4. First, the onset and decay angles of the response windows are broadly consistent across the inertia models, which suggests that the angular localisation is primarily governed by the quasi-steady hydrodynamic coefficient behaviour. Secondly, the amplitude level becomes very sensitive to the added-mass treatment. The constant added-mass model produces the largest response amplitudes, particularly in Zone 4, the frequency-dependent model yields intermediate values, and neglecting added mass results in the smallest response, which is the same as for the Model 18A.

A.0.1. Case 1: No added mass

Figures A.5–A.8 summarise the end-window amplitude A_{end} for Model 32A when the added mass is neglected. Similarly to Model 18A, the response is mostly direction-dependent. Outside the screened angular zones, the amplitude decays to zero, while within the windows the coupled 3DOF system exhibits significant amplitudes. The vertical dotted lines indicate the Den Hartog screening boundaries and are used as a reference to compare the quasi-steady stability prediction with the nonlinear time-domain response.

In Zone 1 (Fig. A.5), the response develops over a wide angular band. A small response is visible at the lower angles, followed by a clear growth into a large response. The response reaches a maximum around $\psi = 46°$ and then decreases as ψ increases. The Den Hartog lines mark the predicted unstable intervals within this range. However, the time-domain response appears broadened, with non-zero amplitudes persisting beyond the quasi-steady boundaries. This behaviour is consistent with a nonlinear, coupled system.

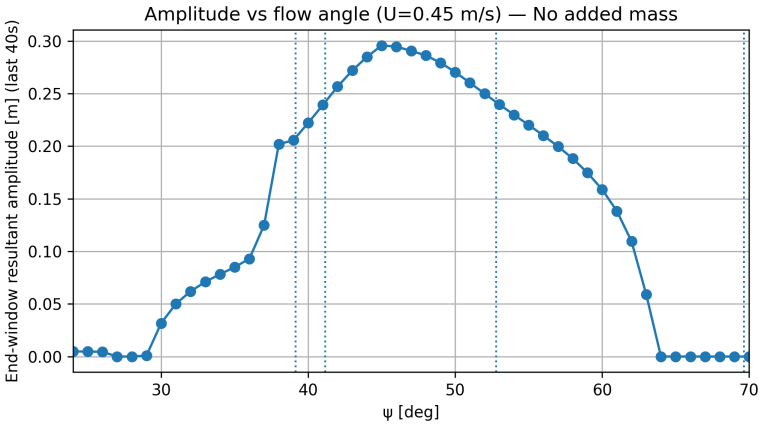

Figure A.5: End-window resultant amplitude A_{end} for Case 1 in Zone 1

Zone 2 (Fig. A.6) forms a relatively smooth and broad plateau. After onset, the amplitude increases rapidly and then remains close to a nearly constant peak level over several degrees, before dropping sharply back to zero. Compared to Zones 1 and 4, the absolute response level is lower, but it remains clearly non-zero across the core of the screened interval. The zero-response towards the upper end occurs slightly offset from the Den Hartog boundary, again indicating that the coupled time-domain dynamics do not collapse exactly at the quasi-steady neutral point.

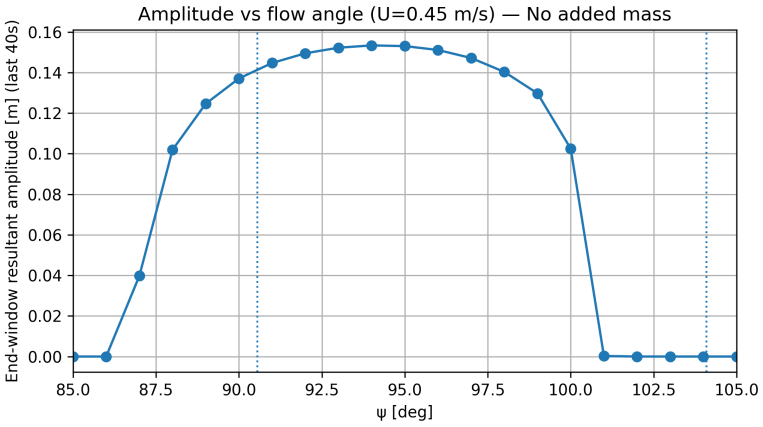

Figure A.6: End-window resultant amplitude A_{end} for Case 1 in Zone 2

In Zone 3 (Fig. A.7), the response appears occurs only over a relatively small range. A_{end} rises from zero, reaches a maximum close to the middle of the interval, around $131°$, and decays again towards both boundaries. The amplitude of the response is very mediate, being smaller than the amplitudes ins Zone 1 and 4. The interval for the Den Hartog criteria matches at the lower boundary but has a slight off-set for the higher boundary.

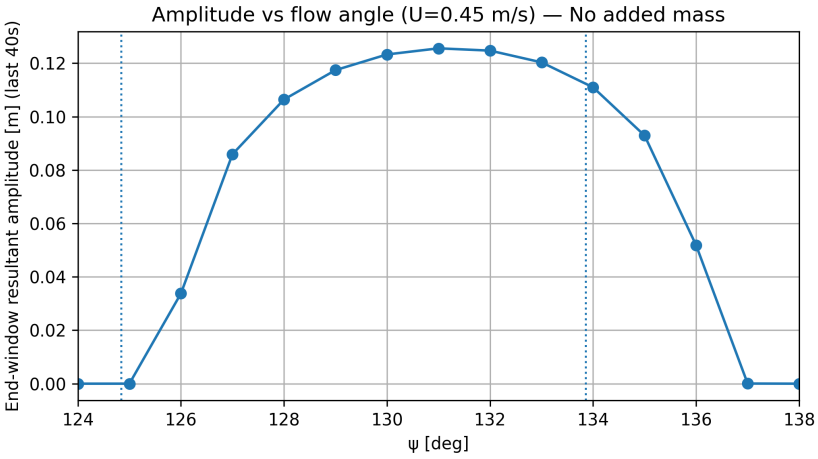

Figure A.7: End-window resultant amplitude A_{end} for Case 1 in Zone 3

Zone 4 (Fig. A.8) exhibits the strongest response for the no-added-mass configuration. The onset is sharp, after which the amplitude reaches a plateau. Near the upper end of the sweep the response remains non-zero, indicating that this region corresponds to the most critical inflow orientations for Case 1. The lower Den Hartog boundary aligns closely with the triggering angle, while the persistence of the limit cycle slightly beyond the predicted upper boundary again reflects nonlinear and coupled effects in the fully time-domain system.

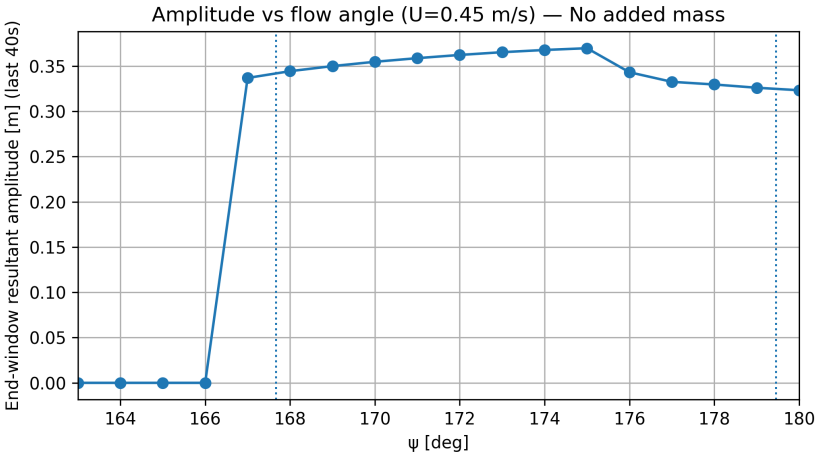

Figure A.8: End-window resultant amplitude A_{end} for Case 1 in Zone 4

A.0.2. Case 2: Constant added mass ($C_{a,x} = C_{a,y} = 1$)

Figures A.9–A.12 show the end-window amplitude for Model 32A using a constant added-mass coefficient; $C_{a,x} = C_{a,y} = 1$. Compared to Case 1, the inclusion of hydrodynamic inertia generally increases the magnitude of the post-onset response and sharpens the onset behaviour in the dominant zones.

In Zone 1 (Fig. A.9), the response stays close to zero over the lower part of the plotted interval. The first Den Hartog interval does not show any response. Once the first Den Hartog boundary is exceeded, and while the inflow direction remains below the lower interval of the second boundary, the oscillations grow rapidly. Beyond onset, the decreases gradually with increasing ψ and ultimately decays back to zero a few degrees before the predicted end of the response window.

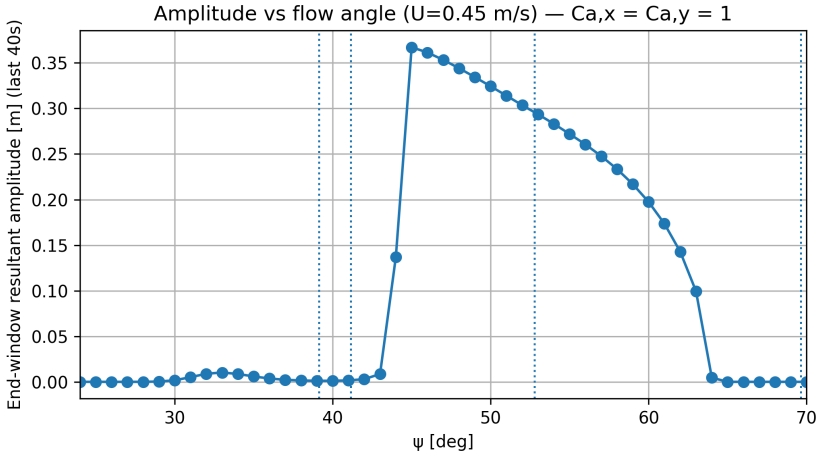

Figure A.9: End-window resultant amplitude A_{end} for Case 2 in Zone 1

Zone 2 (Fig. A.10) again exibits broad plateau. After the onset of the response, A_{end} rises quickly and remains near a nearly constant peak. The response is largely confined within the Den Hartog limits only with again, a slight off-set.

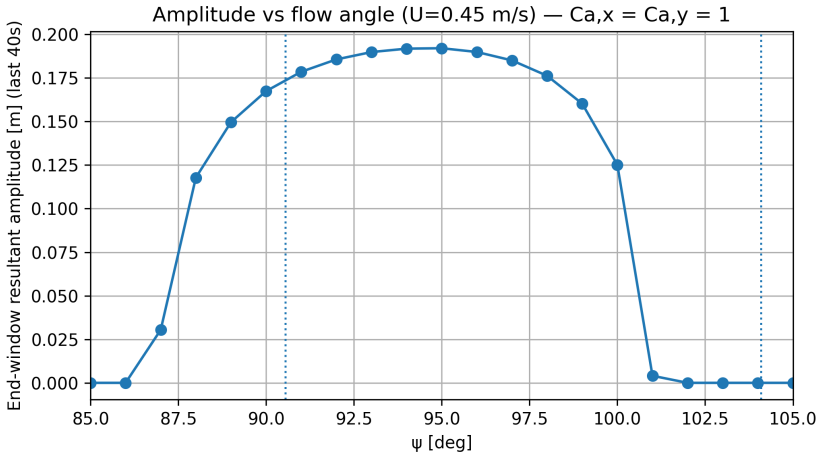

Figure A.10: End-window resultant amplitude A_{end} for Case 2 in Zone 2

In Zone 3 (Fig. A.11), the response rise from near zero to a maximum around the middle of the interval followed by decay towards the edge. The smooth, localised peak and the tight confinement of the response within the Den Hartog bounds suggest that this interval is only weakly unstable.

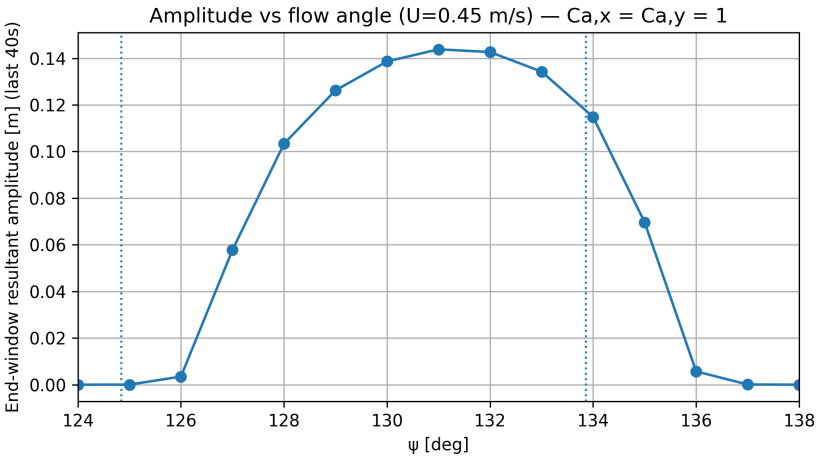

Figure A.11: End-window resultant amplitude A_{end} for Case 2 in Zone 3

Zone 4 (Fig. A.12) remains the most critical region for the constant added-mass implementation. The onset is distinct near the lower Den Hartog boundary, after which the amplitude grows almost linear as ψ increases towards the highest value at $\psi = 180°$. The larger response over the upper part of the interval relative to Case 1 confirms that hydrodynamic inertia is an important contributor to magnitude of the response in this zone.

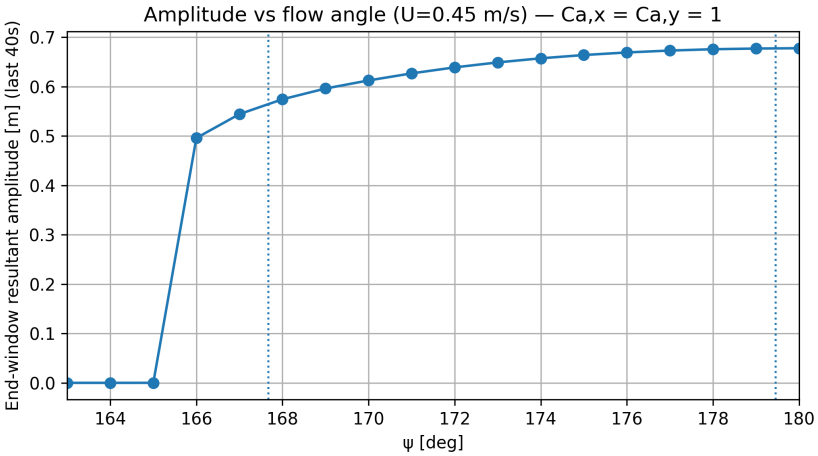

Figure A.12: End-window resultant amplitude A_{end} for Case 2 in Zone 4

A.0.3. Case 3: Frequency-dependent added mass ($C_a(f^*)$)

Figures A.13–A.16 show the end-window amplitude for Model 32A using the frequency-dependent added-mass implementation. The response remains localised in the same Den Hartog screening intervals. Compared to the constant-added-mass model, the frequency-dependent implementation yields very similar response shapes, with modest changes in onset sharpness and plateau level depending on the zone.

In Zone 1 (Fig. A.13), the response stays close to zero throughout the lower part of the interval and then exhibits a sharp onset once the first Den Hartog boundary has been passed. After onset, the oscillation amplitude becomes the largest of the three inertia models. After the maximum, the amplitude gradually decays with increasing ψ until it collapses at the upper a few degrees before the predicted end of the window. As in the previous cases, the non-zero response extends beyond the quasi-steady boundaries, reflecting nonlinear saturation and coupling in the time-domain dynamics.

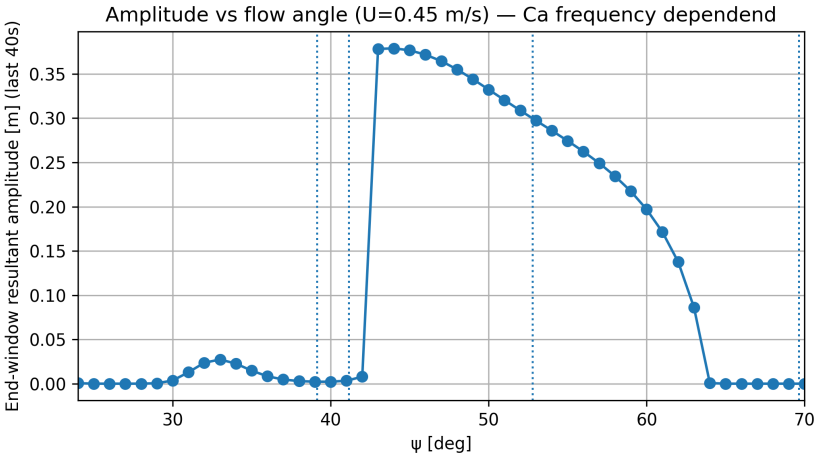

Figure A.13: End-window resultant amplitude A_{end} for Case 3 in Zone 1

Zone 2 (Fig. A.14) again shows a broad plateau-like response. After onset, A_{end} increases rapidly and then remains close to a nearly constant peak value around the middle of the interval. As ψ approaches the upper Den Hartog boundary, the response collapses quickly back to zero. The response is largely confined within the Den Hartog limits, with a small offset near the boundaries, similar to the behaviour observed for Case 2.

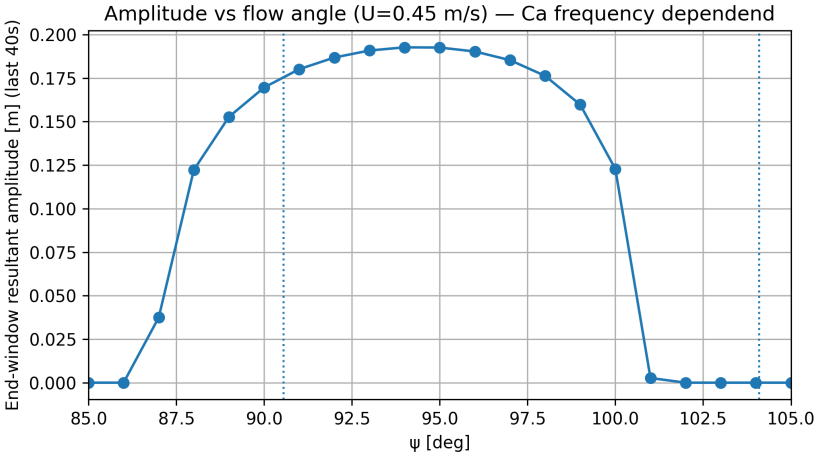

Figure A.14: End-window resultant amplitude A_{end} for Case 3 in Zone 2

In Zone 3 (Fig. A.15), the response again occurs over a relatively narrow angular range. The amplitude rises from zero, reaches a maximum around the middle of the interval, and then decays again towards both edges. Compared to Zones 1 and 4, the response level remains modest. The Den Hartog boundaries provide a good estimate for the onset of the response, while the upper boundary shows a slight offset, with small-amplitude oscillations persisting a few degrees beyond the predicted limit.

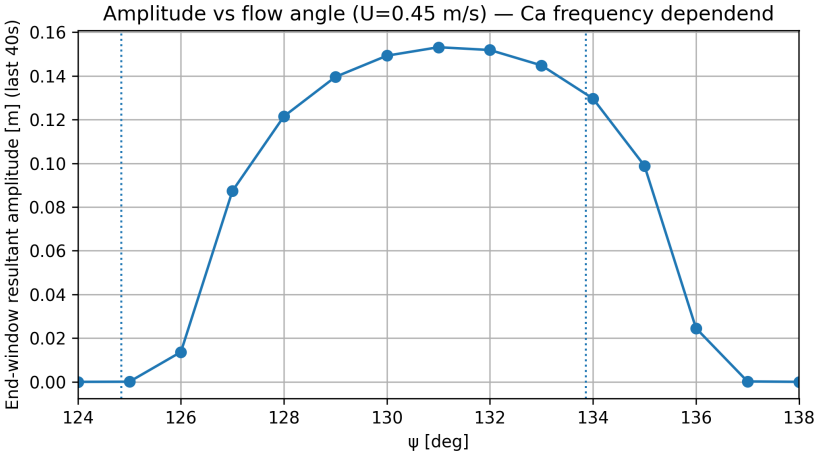

Figure A.15: End-window resultant amplitude A_{end} for Case 3 in Zone 3

Zone 4 (Fig. A.16) again shows the highest response for the frequency-dependent added-mass implementation. Once the lower Den Hartog boundary is exceeded, the oscillations develop rapidly and the amplitude increases monotonically with ψ. Towards $\psi = 180°$, the response approaches a clear plateau.

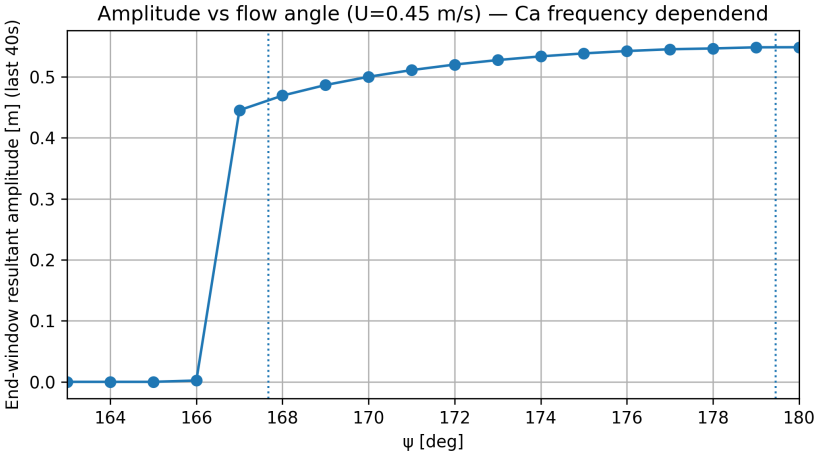

Figure A.16: End-window resultant amplitude A_{end} for Case 3 in Zone 4

A.0.4. Comparison across zones

Figures A.17–A.20 compare the three inertia models directly within each of the four screened zones for Model 32A. In all zones, the Den Hartog boundaries provide a clear first indication of where non-zero responses can occur. The time-domain results show offsets at the boundaries, this behaviour is expected for a nonlinear and coupled 3DOF system.

In Zone 1 (Fig. A.17), the amplitude level dependents strongly on the added-mass treatment once the oscillations are triggered. The case without added mass shows an earlier and more gradual development of the response, while both added-mass models show a sharper onset close to the Den Hartog boundary. After onset of all the cases around $\psi = 45°$, the amplitude ordering is consistent. The frequency-dependent added mass yields the largest response, the constant added mass follows closely, and the no-added-mass case remains the lowest. This confirms that inertia effects mainly govern the post-onset magnitude in this zone. Neglecting inertia effects can also shift the effective response angles relative to the Den Hartog interval.

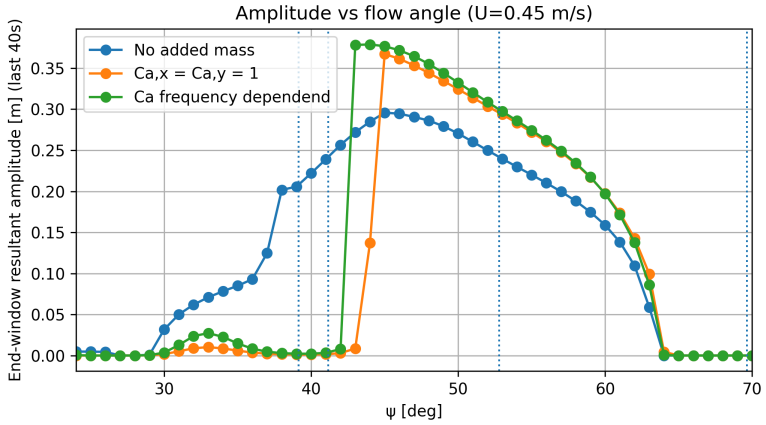

Figure A.17: Direct comparison of end-window resultant amplitude A_{end} across the three added-mass scenarios in Zone 1

Zone 2 (Fig. A.18) shows a broad plateau-like response for all cases. After onset, the amplitude rises rapidly and stays close to a nearly constant peak over the core of the interval, before collapsing towards the upper boundary. The ordering in this zone is similar to the previous zone. Neglecting added mass gives the lowest amplitudes, while both added-mass implementations predict a clearly higher response level. The similarity in shape across the three cases suggests that the added mass does not have a lot of influence in the onset of the response and only has a slight influence on the magnitude of the response.

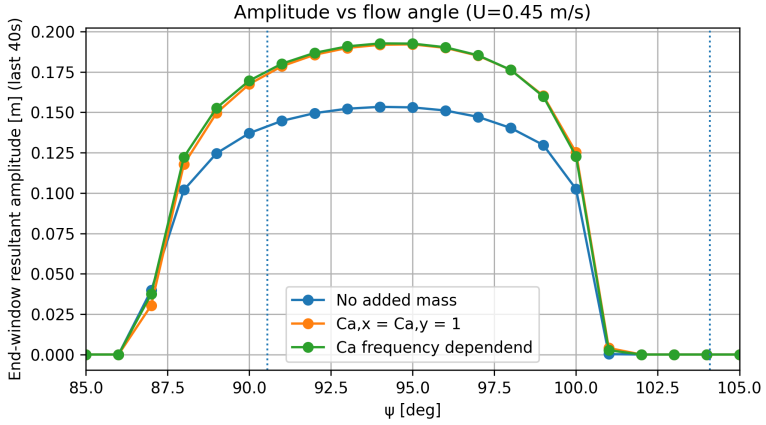

Figure A.18: Direct comparison of end-window resultant amplitude A_{end} across the three added-mass scenarios in Zone 2

In Zone 3 (Fig. A.19), the response is the smallest compared to the other zones. The peak occurs around the middle of the interval and decays towards both edges. Differences between the inertia models are present but limited. The frequency-dependent case gives the largest peak, followed by the constant added-mass model, while the no-added-mass case remains the lowest. The compact shape and low magnitude indicate that this zone corresponds to a weaker instability margin, where inertia effects provide only moderate amplification.

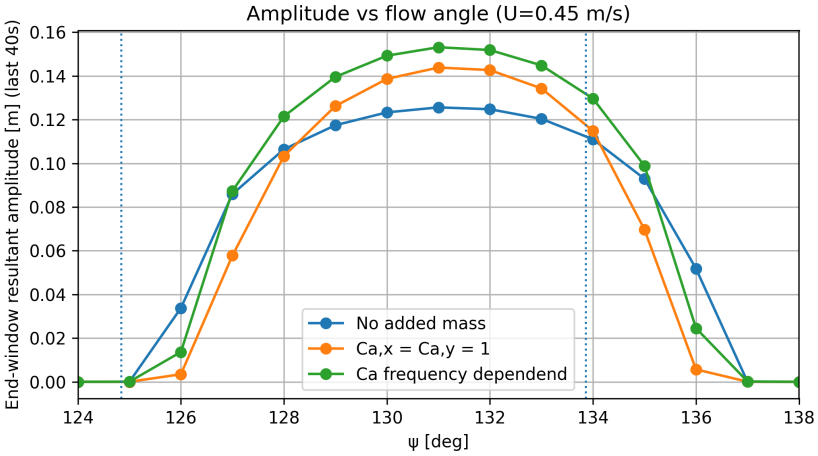

Figure A.19: Direct comparison of end-window resultant amplitude A_{end} across the three added-mass scenarios in Zone 3

Zone 4 (Fig. A.20) is the most dominant response region for Model 32A. All three cases show a distinct onset close to the lower Den Hartog boundary, followed by a monotonic increase towards $\psi = 180°$ and a clear plateau. The amplitude ordering is consistent in this zone and is strongly inertia-dependent. The constant added-mass model predicts the highest amplitudes, followed by the frequency-dependent implementation, and neglecting added mass results in the lowest response. This confirms that hydrodynamic inertia is a primary driver of the response magnitude in this zone.

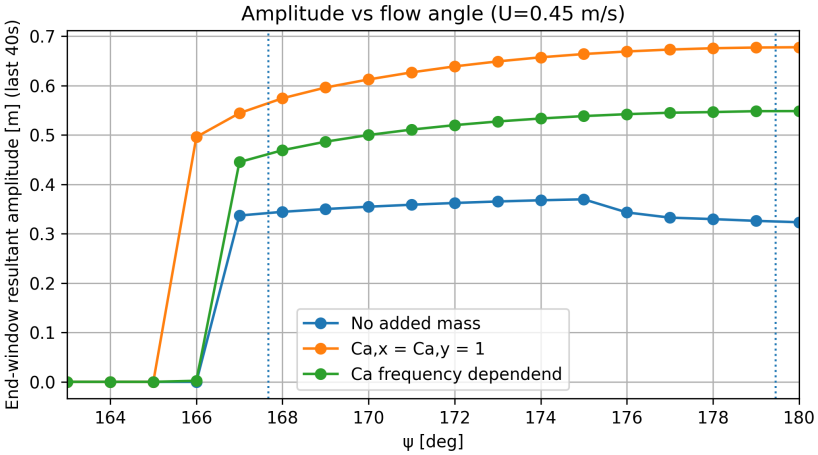

Figure A.20: Direct comparison of end-window resultant amplitude A_{end} across the three added-mass scenarios in Zone 4

A.0.5. Conclusion Model 32A

The time-domain results for Model 32A show a direction-dependent response with four distinct response-active zones. However, compared to Model 18A, the agreement with the Den Hartog screening is clearly weaker. The Den Hartog boundaries often do not coincide well with the onset and decay of the simulated responses, and a significant offset is present in all zones. This mismatch is most noticeable in Zone 1, where the response extends beyond the predicted Den Hartog intervals and the location of the response window differs noticeably from the quasi-steady prediction. As a result, the Den Hartog criterion appears less reliable as a first-order localisation tool for Model 32A than it was for Model 18A.

A key explanation is the uncertainty in the hydrodynamic coefficient representation used for Model 32A. The curve fittings are less certain and require a higher-order representation, which increases the sensitivity of the Den Hartog function and the resulting screening boundaries. Consequently, small fitting errors can shift the predicted stability limits substantially. This also implies that the current set of results should be interpreted with caution, since the response levels and boundary locations may not be fully realistic given the uncertainty in the underlying fitted coefficient curves.

In terms of inertia effects, the simulations still show that the added-mass treatment has a strong influence on the post-onset response magnitude. For Model 32A the frequency-dependent added mass often yields the largest response, except for Zone 4, while the constant added-mass case is not consistently conservative. This behaviour suggests that the coupled dynamics for Model 32A are more sensitive to phase relations and effective frequency content than in Model 18A, which again points to limitations in the present modelling assumptions for this geometry and coefficient set.

Overall, the results expose shortcomings in the integrity of the Model 32A implementation. The systematic offsets relative to the Den Hartog boundaries, together with the sensitivity to higher-order and uncertain curve fits, indicate that the current model does not yet provide a fully robust or physically reliable prediction framework. Before using Model 32A for design conclusions, the coefficient fitting procedure should be revisited to reduce uncertainty and to improve consistency between quasi-steady screening and fully coupled time-domain behaviour.